DEVELOPMENT OF A NON-INVASIVE RESPIRATORY ENERGY HARVESTER USING TRIBOELECTRIC EFFECT

by

Paresh M. Vasandani

B.E. in Biomedical Engineering, University of Mumbai, 2007

Master of Product Development (MPD), Carnegie Mellon University, 2010

Submitted to the Graduate Faculty of

the Swanson School of Engineering in partial fulfillment

of the requirements for the degree of

Doctor of Philosophy

University of Pittsburgh

2017

UNIVERSITY OF PITTSBURGH

SWANSON SCHOOL OF ENGINEERING

This dissertation was presented

by

Paresh M. Vasandani

It was defended on

April 10, 2017

and approved by

Alan Hirschman, Ph.D., Professor, Departmental of Bioengineering

George Stetten, M.D., Ph.D., Professor, Departmental of Bioengineering

Nitin Sharma, Ph.D., Assistant Professor, Departmental of Mechanical Engineering & Materials Science

Wenyan Jia, Ph.D., Research Assistant Professor, Department of Neurological Surgery

Zhi-Hong Mao, Ph.D., Associate Professor, Departments of Electrical and Computer Engineering, and Bioengineering

Dissertation Director: Mingui Sun, Ph.D., Professor, Departments of Neurological Surgery, Bioengineering, and Electrical and Computer Engineering

DEVELOPMENT OF A NON-INVASIVE RESPIRATORY ENERGY HARVESTER USING TRIBOELECTRIC EFFECT

Paresh M. Vasandani, Ph.D.

University of Pittsburgh, 2017

The need to recharge and eventually replace batteries is increasingly significant for operating a variety of wearable electronic devices. Rapid advances in the functions of electronic devices have stimulated the requirements for portable and sustainable power sources, thus opening the possibility of using human biomechanical energy as a promising alternative power source. Respiration is a unique form of spontaneous and stable source of human biomechanical energy that is currently untapped, and has the potential to be converted to a sustainable power source for low power wearable electronic devices and integrated body sensor networks. However, effectively harvesting respiration energy characterized by low frequency and low force, is currently a technological challenge, and cannot be well-achieved by classical energy harvesting methods. In this work, a triboelectric nanogenerator (TENG) is demonstrated as a small and light-weight wearable respiratory energy harvester (wREH), capable of tracking rate and depth of respiration, and can be utilized as a self-powered respiratory motion sensor.

Although TENGs have been demonstrated as a promising technology for mechanical energy harvesting, they have a high inherent impedance which poses a major challenge to their effective integration with electronic systems for practical applications. The high inherent impedance creates a huge mismatch when TENGs are directly integrated with energy storage devices that usually have low impedance, resulting in low energy conversion efficiency. This problem is generally treated by power management circuits which have a limited effect. In this

work, a synchronous switching approach is developed, which has been shown to enhance the TENG output energy by over a factor of two and lower the optimum load resistance, from megaohms to ohms.

Contact electrification in a TENG occurs only when two dissimilar triboelectric surfaces are contacted. However, there exists no theoretical relationship between contact force and triboelectric charge transfer in TENGs. Accordingly, a charge-force relationship is presented by combining the theories of contact electrification and contact mechanics, which successfully explains the tendency of charge transfer. Furthermore, a method to design simulation experiments to predict the TENG output within an order of magnitude using its structural parameters, is presented as an effective design tool.

TABLE OF CONTENTS

LIST OF TABLES

LIST OF FIGURES

PREFACE

Acknowledgements

First and foremost, I would like to express my sincere gratitude to my advisor, Dr. Mingui Sun, for giving me an opportunity to work on this fascinating project, and for his valuable guidance and encouragement along the way. Dr. Sun is a great mentor and a wonderful human being. I have learnt a lot from him about research - and beyond that. If I can be half as active as he is, when I am his age, I would consider myself very lucky. Inspired by a short bike ride with him, I plan to do a 100mile bike ride in the near future, and hopefully many more after that, just like him.

I would like to thank Dr. Wenyan Jia and Dr. Zhi-Hong Mao for their guidance and warm support, and for serving on my committee. I would also like to thank other committee members – Dr. Alan Hirschman, Dr. George Stetten, and Dr. Nitin Sharma.

I thank Dr. Di Gao for letting me work in his lab, and Dr. Jiamin Wu for his helpful insights on PDMS processing. A special thank you to my friend, Bharat Gattu, for his insights and help with PDMS material fabrication. I also thank all my lab colleagues, particularly Bo Luan, Chengliu Li, Shitong Mao, and Yuecheng Li, for making my time in the lab a pleasant one.

Finally, I would like to thank my parents for their unconditional love and unwavering support, and my friends back home for always making me feel included even though we are thousands of miles apart. Without my family and friends, none of this would be possible.

1.0 INTRODUCTION

1.1 HUMAN BIOMECHANICAL ENERGY HARVESTING – THE NEED/OPPORTUNITY AND CHALLENGES

Miniaturization and increase in functionality are the most important trends in electronic technology, making wearable devices one of the most rapidly growing technologies in computing and healthcare. Personal body area network (BAN) provides medical, lifestyle, assisted living, sports, and entertainment functions for the user [1, 2]. Currently, batteries are necessary to power such systems, and are a significant source of size, weight, and inconvenience. Furthermore, the need to recharge batteries or eventually replace them constitutes a significant limitation on operating time of portable and wearable electronics [3, 4]. The limited lifetime and energy storage have made rechargeable batteries the bottleneck of wearable technology, as they limit their sustainable operation [5, 6]. With the anticipated increase in use of wearable technology, there are concerns about potential environmental and human health impacts of rechargeable lithium batteries in electronic waste. This is due to the presence of potentially toxic materials including metals, such as copper, nickel, and lead, and organic chemicals, such as toxic and flammable electrolytes [7]. Recovery, recycling, and reuse of lithium battery materials will be complex and challenging, and therefore there is a need to develop sustainable energy alternatives [8]. Fortunately, advances in low power design has brought down the energy requirements of wearable electronic devices and wireless sensor networks to the scale of microwatts and milliwatts, making

human biomechanical energy harvesting a promising clean alternative to electrical power supplied by batteries [9-11]. Human biomechanical energy harvesting has therefore attracted increasing attention in the past decade [12, 13].

Human biomechanical energy harvesting generally refers to converting mechanical energy available from various sources in the human body to electrical energy. There are two sources of human biomechanical energy: momentary and spontaneous. Momentary sources include discontinuous activities such as walking, running, upper limb motions, etc., whereas spontaneous sources include continuous activities such as blood pressure, heartbeat, respiration, etc. The human body is a tremendous source of energy. An average person of 68 kg with 15% body fat stores ~390 MJ of energy. Muscles convert this stored chemical energy into positive mechanical work with an efficiency of about 25% [14]. If only a fraction of this energy can be unobtrusively harvested, batteries could be eliminated. However, the challenge in doing so arises from the acquisition, regulation, and distribution of power to ensure sustainable and maintenance-free operation [15-17].

Human biomechanical energy is characterized by fluctuating amplitudes and variable low frequency. For instance, frequencies of upper and lower limb motions are typically within 10 Hz [18-20], and respiratory motion frequency is only about 0.33 Hz [21]. Harvesting such irregular low frequency energy *via* traditional energy harvesting techniques based on piezoelectric, electromagnetic and electrostatic transduction mechanisms, may be inefficient [22]. This is because the power generated is strongly dependent on the external vibration frequency, dramatically dropping at low frequencies and requiring the harvester to work at or within a narrow window from the resonant frequency [20, 23, 24]. In addition, due to the structural complexity,

particularly of MEMS-based harvesters, it is a great challenge to integrate an increasing compliant spring and bulk movable mass in a small size [25, 26].

Recently, triboelectric nanogenerators (interchangeably referred to as TENGs or TGs throughout this dissertation) that work on a combination of contact electrification (or triboelectric effect) and electrostatic induction, have been demonstrated as a promising technology for human biomechanical energy harvesting (walking/footfalls [27-30], upper limb motions [31-34], textile-based [35-38], etc.). Since its first report in 2012 [39], TENGs have attracted tremendous research interest as they offer numerous advantages over traditional energy harvesting technologies, namely, low cost, light weight, diverse choice of fabrication materials, and high adaptability design, thus making them more suitable for energy harvesting from low frequency human body motion [40-43].

Respiration is a spontaneous source of human biomechanical energy that is currently untapped, and has the potential of being a sustainable power source for low power wearable electronic devices and integrated body sensor networks. However, in addition to being a low frequency motion, the force generated during respiration is also very low. Therefore, effectively harvesting respiration energy is currently a technological challenge, and cannot be well-achieved by classical energy harvesting methods. The TENG technology offers an exciting new approach in this regard. The challenge with using TENGs is that they usually have low currents (in the microamps range) and a high inherent impedance which results in low energy conversion efficiency. So, power management circuits with low leakage energy storage units are required [44, 45].

1.2 SCOPE AND ORGANIZATION

This dissertation is aimed at evaluating the feasibility of using the triboelectric effect based TENG to harvest respiration energy in a non-invasive manner, and thereby developing a wearable respiratory energy harvester, which can also be utilized as a self-powered respiratory motion sensor capable of tracking rate and depth of respiration.

In that regard, Chapter 2.0 discusses different approaches of harvesting respiration energy, followed by preliminary studies conducted to evaluate the feasibility of using triboelectric effect to harvest respiration energy in a non-invasive manner. Chapter 3.0 discusses the importance of contact force in the triboelectrification process and the fundamental theory of a contact-mode TENG, which does not consider the effect of contact force. Subsequently, a theoretical relationship between the transferred triboelectric charge and contact force for a contact-mode TENG is presented, which has been shown to successfully predict the tendency of charge transfer. Although triboelectrification is a ubiquitous phenomenon, and has been studied for over 2500 years, the charge transfer mechanism between two dissimilar surfaces when at least one of them is insulating is still an unresolved problem in physics [46]. Therefore, presented in chapter 4.0 is a method for designing simulation experiments to create metamodels that can predict the TENG output using its structural parameters such as area, gap, and dielectric thickness, within one order of magnitude. Such metamodels can serve as an effective design tool for TENGs. In Ref. [16], the power that can be generated from respiration by fastening a tight belt around the chest has been estimated to be 0.83 W. This estimation assumes a very ambitious force of 100 N being applied over a 5 cm circumferential change when breathing deeply. Accordingly, chapter 5.0 gives an overview of the mechanism of respiratory motion and subsequently presents a method for direct measurement of force and displacement during normal respiration. This provides a better understanding of the

forces involved, and helps to set the parameters of the benchtop test setup used for characterizing the respiratory harvester. Chapter 6.0 presents the design and fabrication of the harvester and its characterization under normal respiratory motion. The wREH is also demonstrated as a self-powered respiration sensor. Further, since the output of a TENG increases with increase in the effective contact area between its triboelectric layers, a simple and cost-effective method to fabricate micropatterned films is presented. In chapter 7.0 , a switch based TENG structure is presented for enhancing the generator output. This approach significantly lowers the matched impedance of the TENG by several orders of magnitude, and can potentially be used in several applications to improve generator performance, including the respiratory energy harvester. Finally, chapter 8.0 discusses future work. Section 1.3 highlights the main contributions of the dissertation.

1.3 MAIN CONTRIBUTIONS

The main contributions of the dissertation are as follows:

- A new theoretical relationship between the transferred triboelectric charge and contact force for a contact-mode TENG is presented.
- A new method to design finite element simulation experiments to predict the output voltage of triboelectric generators using its structural parameters is presented.
- A new contact-mode based TENG design is demonstrated as a wearable respiratory energy harvester.
- A new method employing synchronous switching to enhance the output energy of TENGs by over a factor of two is presented.

2.0 APPROACHES TO HARVEST RESPIRATORY ENERGY

Respiratory energy can be harvested and converted to electricity from: (a) flow of air, and (b) abdomen/chest motion. A brief overview of different approaches to harvest respiration energy is presented here, followed by preliminary studies conducted to evaluate the feasibility of using triboelectric effect to harvest respiration energy in a non-invasive manner. Potential challenges to implementation are also discussed, and benefits of using a TG over traditional energy harvesting technologies are highlighted.

Starting with the piezoelectric energy harvesting transduction mechanism, Sun, C., et al. (2011) reported a technique that uses piezoelectric polyvinylidene fluoride (PVDF) microbelts to convert the energy from low-speed air flow to electricity via their resonant oscillation [47]. The micrometer thick PVDF thin films fabricated by a top-down reactive ion etching process generated output power in the range of nW–μW at an air flow speed of about 1 ms^{-1}, which represents air flow rate of normal adult human respiration. This approach is potentially in-vivo as the authors discuss biocompatibility and powering implantable biomedical devices as its potential application. However, if wearable electronics were to be powered using this approach, a face mask would be required which would limit real-life applications. In another approach, Wang, J.-J., et al. (2014) demonstrated the design and microfabrication of piezoelectric rubber bands and their application in energy harvesting from human motions [48]. The bands are fabricated as multilayer PDMS cellular structures coated with PTFE films and stretchable gold electrodes and implanted with

bipolar charges. As a potential application, the authors propose that these bands can be mounted on elastic waistbands to harvest the circumferential stretch during breathing. It is claimed that with a 0.63 N force and a 2.5cm deformation, an electric charge of more than 20μC can be collected and stored per breath. Although these piezoelectric approaches are interesting, the fundamental issue is that the potential output power is inversely proportional to the frequency of the fundamental vibration mode, and the design and fabrication complexity (and cost) increases as the triggering frequency reduces [18, 49]. Further, durability of such complexly fabricated microstructures in the application environment is a potential concern.

Next, the electromagnetic energy harvesting transduction mechanism is considered. Electromagnetic generators generally have a higher power output compared to the piezoelectric and electret based approaches [22, 50, 51]. Delnavaz, A. and J. Voix (2012) presents an air-flow respiration energy harvesting device based on electromagnetic induction due to the relative movement of a coil and a suspended magnet [52]. The device is composed of a face mask, connecting tubes and an energy harvesting module, which generates a maximum induced voltage of 25 mV, equivalent to 3.1 μW of power. In another approach, Shahhaidar, E., et al. (2013) demonstrates an off the shelf gearmotor used as a harvester for converting the movements of the torso due to normal respiration into electricity, and compares its performance to two different types of piezoelectric beam benders [53]. To increase the output while minimizing the respiratory effort required to turn the armature, a 50:1 gear ratio was used and an optimal load resistance of 160 Ω was selected. The maximum peak voltage of about 0.5 V was obtained in this study. Although these approaches are relatively less complex, the restricted working mechanism of an electromagnetic generator stemming from the fact that its optimized output power is proportional to square of the triggering frequency generally produces very low voltages (< 1V), as is seen in

the two approaches discussed here. This makes it inefficient to utilize the output power because of the threshold voltage drop of rectifying diodes [44, 54]. In addition, to increase the output any further, the form factor of the device would have to be increased, which is not desirable.

In contrast, TENGs based on the combination of triboelectric effect and electrostatic induction, generally have output voltage that is independent of the triggering frequency, enabling effective utilization of the output power after rectification [42]. Zheng, Q., et al. (2014) demonstrated that a TENG implanted within a rat can convert the mechanical energy from periodic expansion and contraction of the thorax during breathing to power a simulated pacemaker. This presents a significant step forward for lifetime-implantable self-powered medical devices [55]. However, to utilize triboelectric effect to harvest energy from respiratory motion to power wearable electronics, a non-invasive and comfortable approach is desirable. To evaluate this, preliminary studies using two basic modes of contact-separation [39, 56-59] and sliding [60-63] were conducted. These are discussed in section 2.1.2. Table 2.1 gives a summary of different approaches to harvest respiratory energy discussed herein.

Table 2.1. Approaches to harvest respiratory energy along with their potential applications and challenges to implementation.

Energy Harvesting Mechanism	**Respiration Energy Source** (**A**: flow of air; **B**: abdomen/chest motion)	**Potential applications** (**I**: powering implantable medical devices; **W**: powering wearable electronic devices)	**Potential challenges to implementation**
Piezoelectric	**A** (in-vivo as claimed by authors [47])	**I** (as claimed by authors); **W** may also be possible	i. Complex/costly fabrication process ii. Microbelt durability may be a concern iii. To power wearables, a face mask would be required that would limit real-life applications

Table 2.1 (continued)

	B [48]	**W**	i. Complex/costly fabrication process ii. Durability of stretchable electrodes may be a concern
Electromagnetic	**A** [52]	**W**	i. Face mask limits real-life applications ii. Output voltage in the mV range is not efficient for rectification
	B [53]	**W**	i. Output voltage in the mV range is not efficient for rectification ii. Challenge to enhance output while keeping a small form factor
Triboelectric effect + Electrostatic induction	**B** (in-vivo) [55]	**I**	i. Huge impedance mismatch with energy storage units.

2.1 PRELIMINARY STUDIES: EVALUATING FEASIBILITY OF USING TRIBOELECTRIC EFFECT TO HARVEST FROM A LOW FREQUENCY MOTION

Initial sliding experiments were conducted using the prototype shown in Figure 2.1. The Prototype parameters are given in Table 2.1. Per the sliding mode structure shown in Figure 2.1(a), the top layer (dielectric 1 with metal 1 attached) can slide longitudinally on the bottom layer (dielectric 2 with metal 2 attached), which is fixed. When the layers fully overlap, equal and opposite tribo-charge density (σ) is developed at the contacting surfaces of the dielectrics due to the triboelectric effect. The tribo-charges on insulators only distribute in the surface layer and their decay with time is negligible [64]. As the lateral separation distance (x) increases as the top layer slides outwards, the in-plane charge separation induces a potential difference between the electrodes. Subsequently,

as the top layer slides back to the full overlap position, the potential difference drops. Electrical connections to the metal electrodes are made so the voltage signal can be measured. The peak-to-peak output voltage with manual rubbing was about 60 V. Although this initial sliding test showed promise, it was necessary to further evaluate the possibility of using a TG in sliding-mode under a low-force and low-frequency motion. To do so, a bench-top setup shown in Figure 2.2 was constructed.

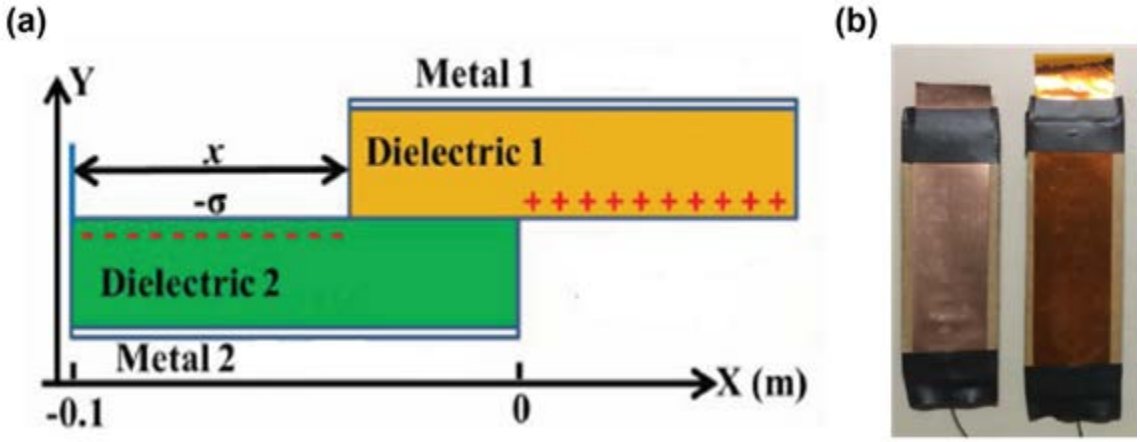

Figure 2.1. Structure of sliding-mode TG (Figure from Ref. [63]). (b) Fabricated prototype.

Table 2.2. Prototype parameters for sliding-mode test.

Parameters	Selected Values
Dielectric 1	Polyimide film
	(relative dielectric constant, ε_{r1} = 3.4, 50μm thick)
Dielectric 2	PET film
	(relative dielectric constant, ε_{r2} = 3.4, 50μm thick)
Electrodes (Metal 1 &2)	Gold
Width	~ 0.025m
Length of dielectrics	~ 0.05m
Maximum separation distance (x)	~ 0.05m
Sliding Velocity (v)	Manual rubbing

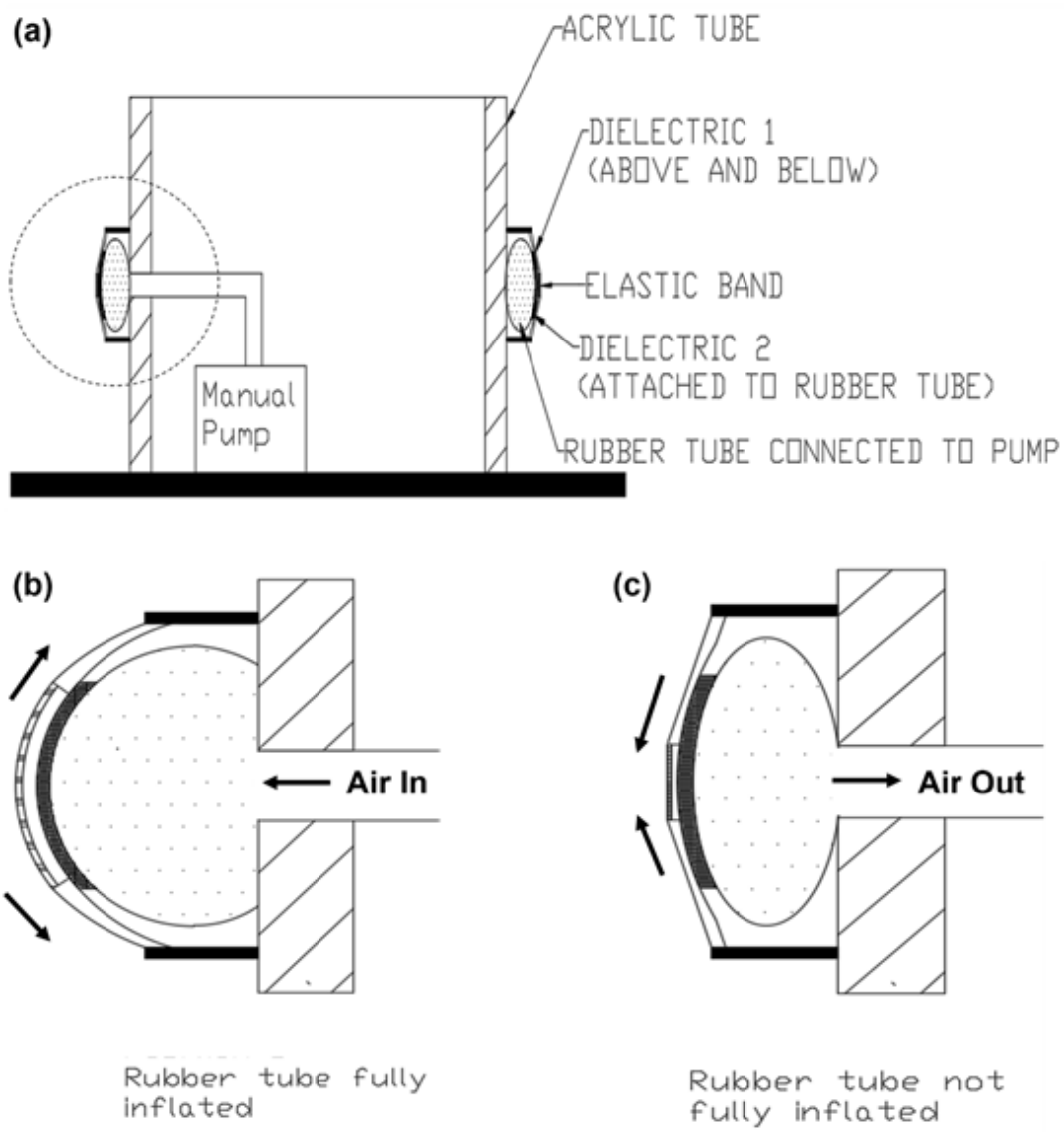

Figure 2.2. (a) Bench-top setup schematic for sliding-mode test. (b) Scaled-up portion of the region marked with a dashed circle in (a) when the tube is inflated. (c) Scaled-up portion of the region marked with a dashed circle in (a) when the tube is deflated.

The set-up consists of a rubber tube connected to a manual pump, so it can be inflated and deflated. Dielectric 2 film (with deposited Au electrode) was attached to the rubber tube, and two Dielectric 1 films (with deposited Au electrodes) connected by an elastic band, were positioned over dielectric 2, such that during the inflation and deflation of the rubber tube, the dielectric layers

will slide back and forth against each other to generate electricity. The two sliding mechanisms were connected in parallel for measurement. However, no appreciable output voltage was generated (a few hundred millivolts peak-to-peak). The dielectric materials used were the same as those listed in Table 2.2. It was therefore concluded that although it may be possible to utilize a sliding mechanism to harvest energy from respiratory motion, the design of such a mechanism would be complex to obtain a meaningful output for powering an electronic device. Next, the contact-mode was evaluated.

The feasibility of using contact-mode was evaluated by modifying the bench-top setup shown in Figure 2.2 for a TG fabricated with a concave substrate. The contact-mode TG structure schematic, fabricated prototype, and the modified bench-top setup are shown in Figure 2.3(a-c) respectively. The contact-mode works similar to the sliding-mode, except that the motion is vertical contact-separation instead of lateral sliding, and is discussed in more detail in chapter 3.0 The substrate structure maintains a space between the two polymer films, except when a force is applied. The TG was sandwiched between the tube and a Polyvinyl chloride (PVC) sleeve at the front most part of the tube as shown, based on the assumption that this part (crudely representing the front of the abdomen) is where the device would be positioned. The TG used in conjunction with the pumping system which serves as the source of a low frequency cyclic compressive force, gives an average peak-to-peak output voltage of about 2.17 V (Figure 2.2(d)). This is in the range of the output voltage generated from rat's breathing by the implanted triboelectric nanogenerator discussed earlier in this chapter.

This preliminary study confirmed the potential of using a contact-mode TG to non-invasively harvest energy from respiration motion. Hence this mode is selected for further development.

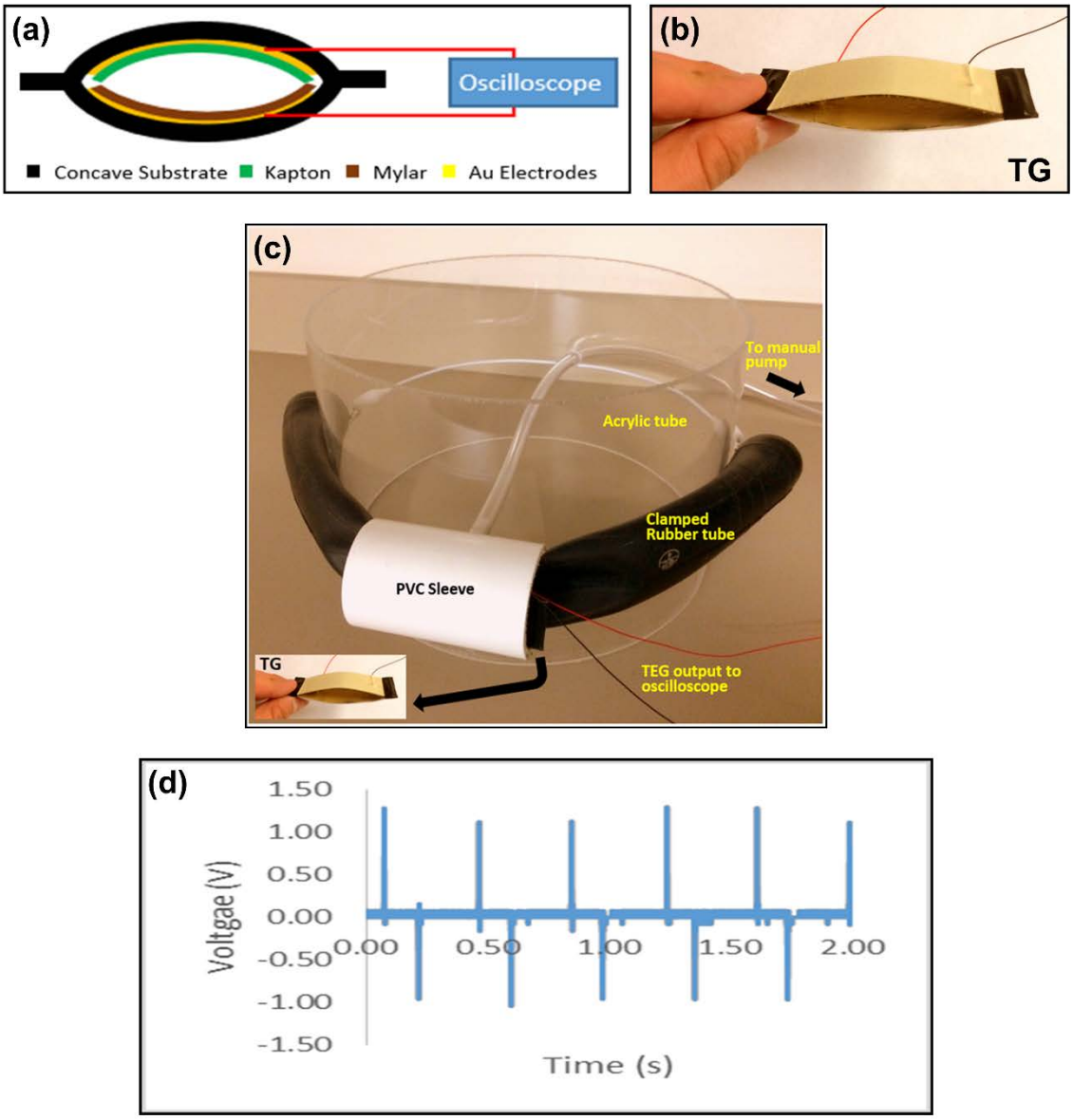

Figure 2.3. (a) Contact-mode TG structure schematic. (b) Fabricated prototype. (c) Bench-top test setup for contact-mode test. (d) Measured output voltage of the TG.

3.0 TRIBOELECTRIC CHARGE - CONTACT FORCE RELATIONSHIP FOR TWO TRIBOELECTRIC LAYERS

3.1 INTRODUCTION

Contact force plays an important role in the triboelectric charge generation process in a TENG. A larger contact force increases the triboelectric charge density and thereby results in a higher current and voltage. An instance of this can be seen in the experiments conducted on a flexible zig-zag shaped multilayered TENG, with Kapton and Polytetrafluoroethylene (PTFE) as its dielectric/triboelectric materials, and Aluminum as the electrode material [28]. Another instance is seen in the experiments on a human skin based TENG that is based on periodic contact-separation between human skin and a micropyramid patterned polydimethylsiloxane (PDMS) film deposited with Indium tin oxide (ITO) electrode, wherein, the magnitude of the output voltage is proportional to the applied pressure [31]. Although contact force is a critical factor that affects the output of a contact-mode triboelectric generator, a theoretical relationship between transferred charge and contact force is not reported in literature. Consider the well-accepted theoretical *V-Q-x* relationship given in equation (3-1) developed to provide guidance for rational design of contact-mode TENGs [56], which does not explicitly consider the impact on contact force.

$$V = -\frac{Q}{A\varepsilon_0}\left(\frac{d_1}{\varepsilon_{r1}} + \frac{d_2}{\varepsilon_{r2}} + x(t)\right) + \frac{\sigma\, x(t)}{\varepsilon_0} \tag{3-1}$$

where V is voltage between the electrodes, Q is the amount of transferred charge between the electrodes, A is the apparent area of contact, x is the separation distance between the dielectric or triboelectric layers, σ is the triboelectric charge density, d_1 and d_2 represent the thickness, while ε_{r1} and ε_{r2} are the relative dielectric constants of the two layers, and ε_0 is permittivity of free space.

The TENG structures that the above *V*-*Q*-*x* relationship is derived for are shown in Figure 3.1(a). Briefly, the contact side of the triboelectric layers are stacked facing each other, with the non-contact side deposited with a metal electrode. Once an external mechanical force is applied to the structure, the two dielectric layers make contact. Owing to surface charge transfer due to contact electrification, the contacting surfaces will have equal and opposite triboelectric charge density σ. When the force is removed, the separation between the triboelectric layers increases, and a potential difference V is induced between the electrodes. This potential is responsible for driving charges Q between the two electrodes via an external load, when connected. In Figure 3.1(b), contact occurs between a metal and a dielectric layer, i.e., the metal acts as the triboelectric layer of the TENG. The *V*-*Q*-*x* relationship for the conductor-to-dielectric contact-mode can thus be obtained by simply substituting $d_1 = 0$ in equation (3-1).

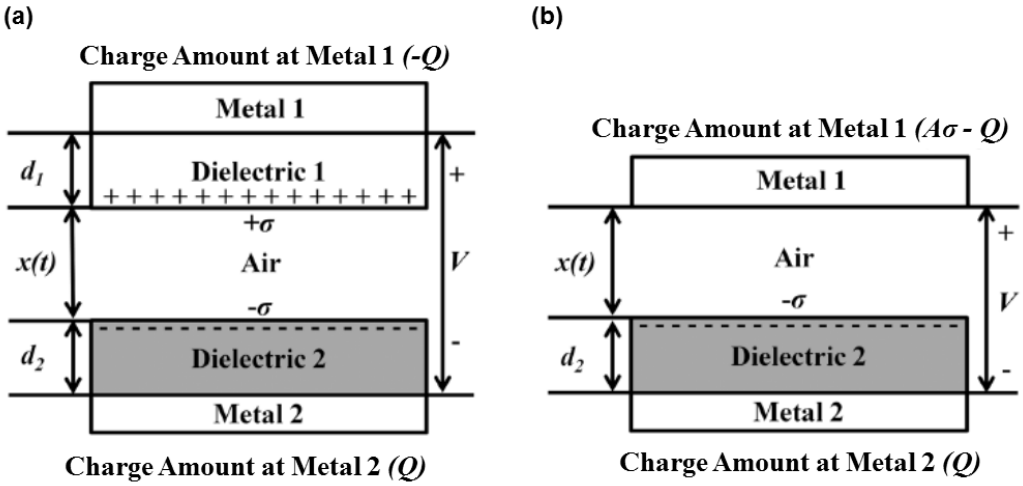

Figure 3.1. Contact-mode TENG structures for (a) dielectric-to-dielectric contact, and (b) conductor-to-dielectric contact. Image from Ref. [56].

From the discussion above, the TENG output is dependent on the development of surface triboelectric charge density (σ) and is directly proportional to it. This charge is only developed when the two triboelectric layers are brought into contact by an external force, as mentioned above. Therefore, understanding the relationship between triboelectric charge and contact force is important, as it can serve as an important guide in the design of contact-mode TENGs. Accordingly, a theoretical relationship between the transferred triboelectric charge (q) and contact force (F) is presented for a contact-mode TENG, by combining the theories of contact electrification and contact mechanics (briefly described below). Subsequently, using the calculated triboelectric charge, open circuit voltage (V_{oc}) of a TENG is predicted for varying contact forces. Furthermore, to show that the effect of different surface morphologies is captured by the *q-F* relationship, V_{oc} of TENGs made with triboelectric layers having different surface roughness characteristics is assessed.

3.1.1 Contact charging involving insulators

Triboelectric effect or contact electrification is universal and has attracted many investigations, but due to the variations in the structure and morphology of insulator materials, there has been no conclusive mechanism for all triboelectric phenomena. The mechanism of charge exchange between two contacting surfaces when at least one of them is insulating, is one of the oldest unresolved problems in physics [65-67]. Reports proposing mechanisms involving electron transfer, ion transfer, and material transfer exist in literature [68, 69]. On the other hand, metal-to-metal contact charging is well understood. Charge transfer in this case is explained using the mechanism of electron transfer that results from the difference in work function (ϕ) between the contacting metal surfaces to equalize their energy levels. This is used to explain metal-to-insulator contact charging, by assigning an effective work function to the insulator. Electron transfer is proposed to occur between the metals' fermi level and localized energy levels in the band gap of the insulator [70]. Several charge transfer models for insulator-to-insulator contacts are presented which are similar to those for metal-insulator contact, except that the available energy levels are at the surface instead of the bulk, and these levels are called "surface states". The surface state theory is used to explain the charge transfer between the surface states of the two contacting materials, driven by the "surface work function" difference between the materials, and conceptually applies equally to [71-73]. This theory has two limits. In the low-density limit, a finite number of states on the dielectric surface are filled or emptied. In the high-density limit, an electric field is created between the dielectric surfaces by charge exchange to equalize the fermi levels of the contacting materials. Although the high-density limit of this theory has been shown to predict the charging of toner particles in electrophotography (within a factor of 2), it does not

explain all experimental observations [74-76]. However, it does explain the sensitivity of contact charging, and is used here for deriving a relationship between charge transferred and contact force.

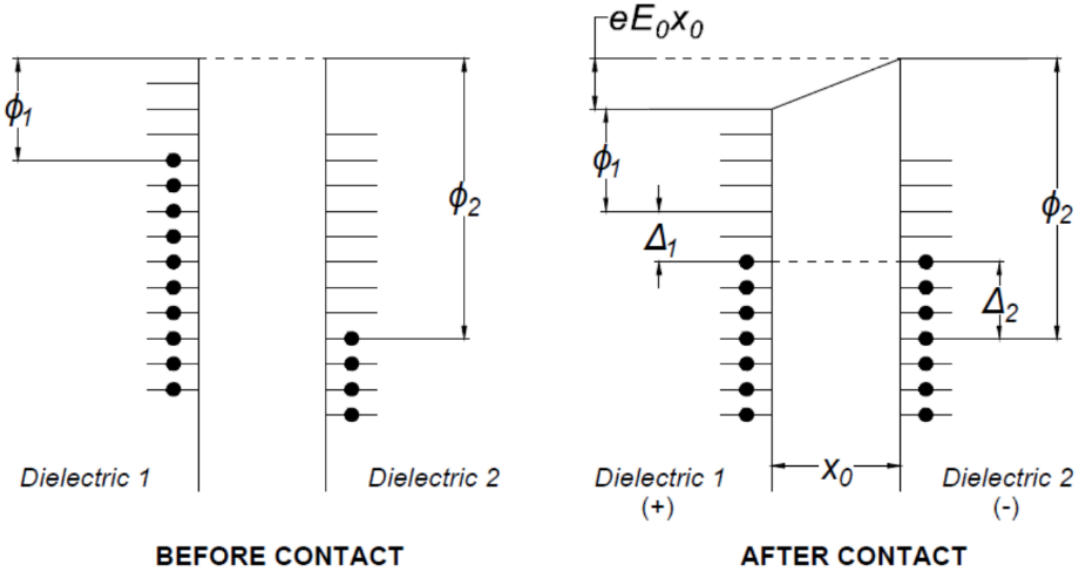

Figure 3.2. Energy level diagram for insulator-insulator contact. Figure modified from Ref. [76].

Figure 3.2 shows the energy level diagram for insulator-insulator contact (low-density state is the "before contact" state, while the high-density" state is the "after contact" state). Filled surface states are represented by a dash with a black dot, whereas dashes without a dot represent empty surface states. On contact, electrons move form filled states of dielectric 1 to empty states of dielectric 2, to equalize the fermi levels of the two materials, and the expression for the energy level is given by [76]:

$$\phi_1 + \Delta_1 + eE_0x_0 = \phi_2 - \Delta_2 \tag{3-2}$$

where ϕ_1 and ϕ_2 are the effective or surface work functions of dielectric 1 and dielectric 2, respectively; Δ_1 and Δ_2 are changes in the fermi energy of dielectric 1 and dielectric 2,

respectively, due to the charge transfer; E_0 is the electric field at the contact point between the dielectrics; x_0 is the critical separation distance between the two dielectrics when charge transfer ceases; e is the elementary charge.

3.1.2 Contact mechanics

Virtually all engineering surfaces are rough to some degree. When two surfaces are pressed together, the asperities on the surface make contact [77]. Therefore, the real area of contact (A_r) is different from the nominal or apparent area of contact (A), and only A_r is available to support the load. For many rough surfaces of engineering importance, surface height and gradients are random and can be modeled by a Gaussian probability distribution. This is the reason why such surfaces can be analyzed statistically by consideration of random functions in several variables. Measured profiles of several real surfaces having vastly different roughness characteristic were used to predict A_r and F from various statistical elastic contact models and contrasted to the deterministic fast Fourier transform (FFT)-based contact model, wherein the surfaces are being analyzed as they are measured, accounting for all peaks and valleys without compromise [78]. All these mathematical models which represent a complex surface profile using just a few key statistical parameters showed good quantitative and qualitative agreement (within an order of magnitude or closer) among themselves, producing nearly linear predictions of A_r as a function of F and in some cases. Here, the Bush, et al.'s statistical contact model is used [79], wherein elastic contact of an isotopically rough surface with a plane is approximated by the summits of a random process model by paraboloids with the same principal curvatures and then applying the classical Hertzian solution for their deformation. The asymptotic solution to this contact model is given by:

$$A_r = \frac{F}{E'}\sqrt{\frac{\pi}{m_2}} \tag{3-3}$$

where E' is the equivalent elastic modulus, and m_2 is a statistical surface parameter called RMS (root mean square) slope, and is given by:

$$m_2 = \frac{1}{N}\sum_{n=1}^{N}\left(\frac{dz}{dx}\right)_n^2 \tag{3-4}$$

where *N* is the total number of data points on the surface profile scan and *z* is the surface height relative to its mean.

3.2 DERIVATION

In equation (3-2), the changes in fermi energies due to charge exchange, Δ_1 and Δ_2, can be expressed as follows:

$$\begin{aligned}\sigma_1 &= e\Delta_1 N_1 \\ \sigma_2 &= e\Delta_2 N_2\end{aligned} \tag{3-5}$$

where σ_1 and σ_2 are the triboelectric charge densities for dielectric 1 and dielectric 2, respectively; N_1 and N_2 are the number of surface states per unit area per unit energy (assumed constant in energy) on dielectric 1 and dielectric 2, respectively.

Using the principle of superposition, the electric field E_0 can be approximated by:

$$E_0 \approx \frac{\sigma_1 + \sigma_2}{\varepsilon_0} \tag{3-6}$$

where ε_0 is the permittivity of free space.

Combining equations (3-2), (**3-5**), and (3-6), gives:

$$\frac{\sigma_1}{eN_1} + \frac{\sigma_2}{eN_2} = \phi_2 - \phi_1 - \frac{ex_0}{\varepsilon_0}(\sigma_1 + \sigma_2) \tag{3-7}$$

Since charges are exchanged to neutralize the electric field created due to the difference in the effective work functions of the materials and the critical separation distance, the net charge on the dielectric surfaces would be equal (and opposite), i.e., $|\sigma_1| = |\sigma_2| = |\sigma|$. Applying this condition of charge neutrality, equation (3-7) becomes,

$$\sigma = e\left(\frac{N_1 N_2}{N_1 + N_2}\right)(\phi_2 - \phi_1) - \left(\frac{2\sigma e^2 x_0}{\varepsilon_0}\right)\left(\frac{N_1 N_2}{N_1 + N_2}\right) \tag{3-8}$$

According to Schein, L. B., et al. (1992), the high-density limit should occur when $e^2 x_0 N_1 N_2 / \varepsilon_0 (N_1 + N_2) = 1$, requiring the charge transferred per unit area to be ~ 6 x 10^{16} m^{-2}, which is orders of magnitude higher than is experimentally observed (10^{14} m^{-2}). This is estimated by assuming $N_1 = N_2 = N_e$, with a reasonable difference in solid state work functions, $\phi_2 - \phi_1$ = 1 eV, and x_0 = 10 Å [71]. However, x_0 values calculated from experimental values of the transferred charge per unit area, are orders of magnitude larger than expected. Using this assumption for the high-density limit, equation (3-8) can be simplified as follows:

$$\sigma = \frac{(\phi_2 - \phi_1)\varepsilon_0}{3ex_0} \tag{3-9}$$

Since the transferred triboelectric charge is a product of the triboelectric charge density and the apparent contact ($q = \sigma A$), we get,

$$q = \frac{(\phi_2 - \phi_1)A\varepsilon_0}{3ex_0} \tag{3-10}$$

Now, from the theory of contact mechanics discussed above, A can be replaced by A_r in equation (3-10), as the charge transfer will occur in the real area of contact. Combining equations (3-10) and (3-3), we get the following relationship between triboelectric charge and contact force:

$$q = \frac{\left(\frac{F}{E'}\sqrt{\frac{\pi}{m_2}}\right)(\phi_2 - \phi_1)\varepsilon_0}{3ex_0} \tag{3-11}$$

From equation (3-11), it can be said that for a given set of triboelectric materials (m_2 = constant), the triboelectric charge is directly proportional to the contact force (F) and inversely proportional to the critical separation distance (x_0) between the two materials. This can be clearly visualized in the contour plot shown in Figure 3.3, simulated for a TENG made using a PET film and a PDMS microdome patterned film as its triboelectric materials. The charge transferred is the highest (up to 35 pC) when F is at its maximum (10 N) and x_0 is at its simulated minimum (100 nm). The selected range of x_0 for simulation is based on observed values [71, 80], and the range

of *F* is selected to ensure that it covers the experimental conditions herein. All the parameters used for theoretical calculations and experiments are presented in Table 3.1.

Table 3.1. Theoretical and experimental parameters

Parameters	**Parameter Value**	
Dielectric 1	Mylar® PET film (d_1 = 0.05 mm; ε_1 = 3.1)	
Dielectric 2	#1. PDMS (Sylgard® 184) film with microdome patterns (d_2 = 0.5 mm; ε_1 = 2.72; dome size about 5µm; m_2 = 25.014) *	#2. PDMS (Sylgard® 184) film with nanoprojections surrounded by nanocracks (d_2 = 0.5 mm; ε_1 = 2.72; nanoprojection size about 200 nm; m_2 = 921.9) *
ϕ_1	4.25 eV [39, 81]	
ϕ_2	4.85 eV [39, 81]*	
x	10 mm (experimental setting)	
ε_0	8.854e-12 F/m	
e	1.6e-19 C	
υ_1 *(Poisson's ratio for dielectric 1)*	0.38	
υ_2 *(Poisson's ratio for dielectric 2)*	0.5 [82]	
E_1	3.378 GPa	
E_2	1.32 MPa [82]	
$E^{'}$	1.759 MPa*	
A	15mm x 25mm (TENG prototype area size)	

*Note:

i. *Effective work function of PDMS is assumed to be equal to that of polyvinyl chloride (PVC) due to proximity in the triboelectric series*
ii. *RMS slope (m_2) is only evaluated for PDMS films (discussed more in section 3.3.1). The PET film is considered to be an ideal flat surface.*
iii. *Effective elastic modulus is calculated using the following formula:*

$$\frac{1}{E^{'}} = \frac{(1-\nu_1^2)}{E_1} + \frac{(1-\nu_2^2)}{E_2}$$

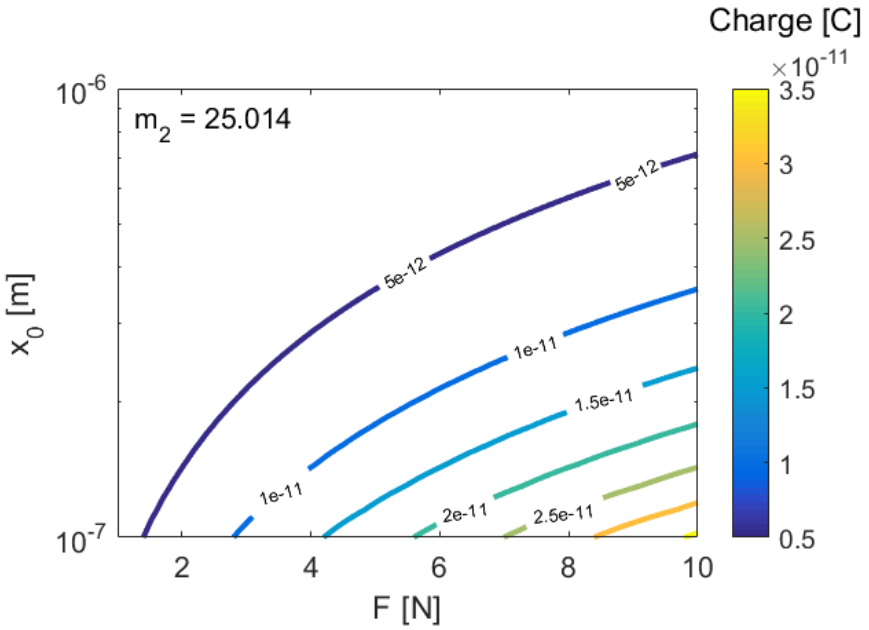

Figure 3.3. Contour plot of triboelectric charge with respect to critical separation distance and contact force.

3.3 EXPERIMENTAL VERIFICATION

To further validate the theoretical equation (3-11) presented in the previous section, a set of experiments were conducted. First, V_{oc} of the TENG made using the microdome patterned film is recorded under contact forces ranging from ~0.45 kgf (4.4 N) to ~0.51 kgf (5 N). The peak values of the experimental open-circuit voltage were compared to the peak V_{oc} values predicted using equation (3-12), obtained by substituting $Q = 0$ in equation (3-1) for open-circuit condition and combining it with equation (3-11). Second, to evaluate the effect of different surface morphologies, V_{oc} of a TENG made with a PDMS film with microdome patterns (PDMS film #1) is compared to that made with a PDMS film with nanoprojections surrounded by nanocracks (PDMS film #2). A PET film is used as the other dielectric for both TENGs. The two PDMS films have very different surface roughness characteristics (discussed more in section 3.3.1).

$$V_{oc} = \frac{\left(\frac{F}{E'}\sqrt{\frac{\pi}{m_2}}\right)(\phi_2 - \phi_1)x}{3ex_0 A} \tag{3-12}$$

Equation (3-12) gives the relationship between the open-circuit voltage of a contact-mode TENG and contact force. For carrying out the calculations here, x_0 is taken to be 100 nm. All other parameters are given in Table 3.1.

3.3.1 Evaluating root mean square (RMS) slope of a surface profile

The RMS slope of a surface profile is evaluated using Gwyddion 2.47 [83]. A scanning electron microscopy (SEM) image of the PDMS film surface to be evaluated is used for this purpose. Figure 3.4 shows the SEM images and the 3D representations of the PDMS films #1 and #2, used for the calculation of RMS slope (m_2). The difference between the surface morphologies is clearly seen – PDMS film #1 has well-ordered microdome structures and a more consistent height profile as compared to the pattern and height profile of the nanostructures in PDMS film #2. The m_2 surface roughness parameter is one way of quantifying the difference in the observed roughness profiles of these surfaces. Five surface profile scans are performed for each PDMS film, and m_2 is recorded from each scan. The mean value of m_2 is used for calculation of V_{oc} from equation (3-12). An example surface profile scan for each film is shown in Figure 3.5 along with its value of m_2. The overall mean and standard deviation (SD) of m_2 for PDMS film #1 is 25.014 (n = 5, SD = 2.197) and for PDMS film #2 is 921.9 (n = 5, SD = 49.245).

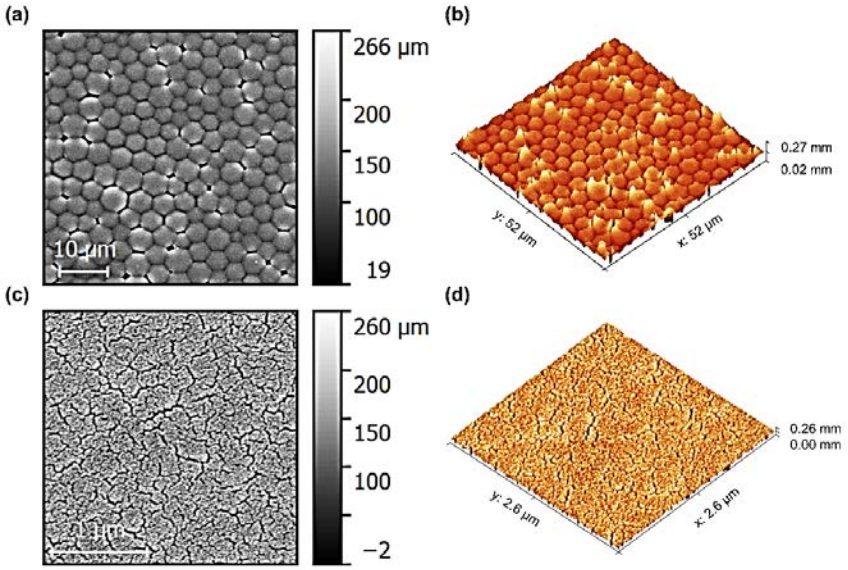

Figure 3.4. (a) SEM image of PDMS film #1 that is used for evaluation of RMS slope. (b) 3D representation of (a). (c) SEM image of a PDMS film #2 that is used for evaluation of RMS slope. (d) 3D representation of (c). Note: Scale represents the surface height relative to its mean.

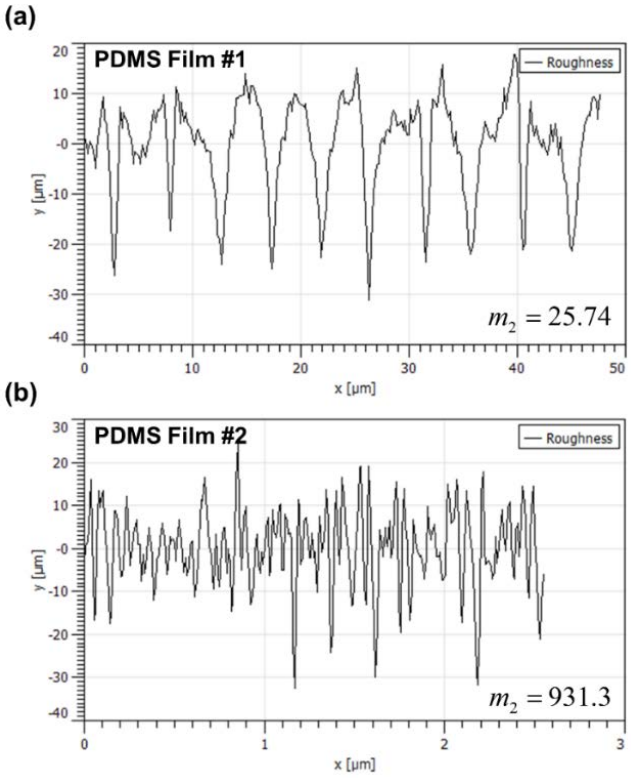

Figure 3.5. Surface profile scans showing the roughness profile of (a) PDMS film #1 and (b) PDMS film #2.

3.3.2 Results

Figure 3.6 shows the theoretical and experimental comparison of dependence of V_{oc} of a TENG made with PDMS film #1 on contact force. As expected, a linear trend is observed in both cases, and the theoretical model can predict the peak values within an order of magnitude. Experimentally, as the force increases from 4.4 N to 5 N, the mean peak values of the V_{oc} increase from 10.73 V (n = 7, SD = 0.79) to 22.53 V (n = 7, SD = 0.21). Theoretically, as the force increases from 4.4 N to 5 N, the peak values of the V_{oc} increase from 47.50 V to 53.82 V.

Figure 3.7 shows the theoretical and experimental comparison of V_{oc} of TENGs made from PDMS film #1 and #2, while the force is kept constant. As expected, the surface with a higher value of m_2, i.e., film #2, has a lower voltage output, while the surface with a lower value of m_2, i.e., film #1, has a higher voltage output. This is because the real contact area (A_r) decreases with increase in m_2, per equation (3-3), resulting in lower triboelectric charge transfer on contact. The theory successfully estimates this trend and the TENG output is within an order of magnitude for the two different surface morphologies. The experimental mean peak V_{oc} for film #1 and #2 is 16.35 V (n = 8, SD = 0.21) and 3.94 V (n = 10, SD = 0.33), respectively. The theoretical mean peak V_{oc} for film #1 and #2 is 50.57 V and 8.33 V, respectively.

A point worth noting is that the difference in magnitude is potentially due to uncertain factors such as impurities, oxidized layer, separation speed, etc. [76, 84, 85], and assuming values of certain unknown parameters such as effective work function of PDMS and critical separation distance.

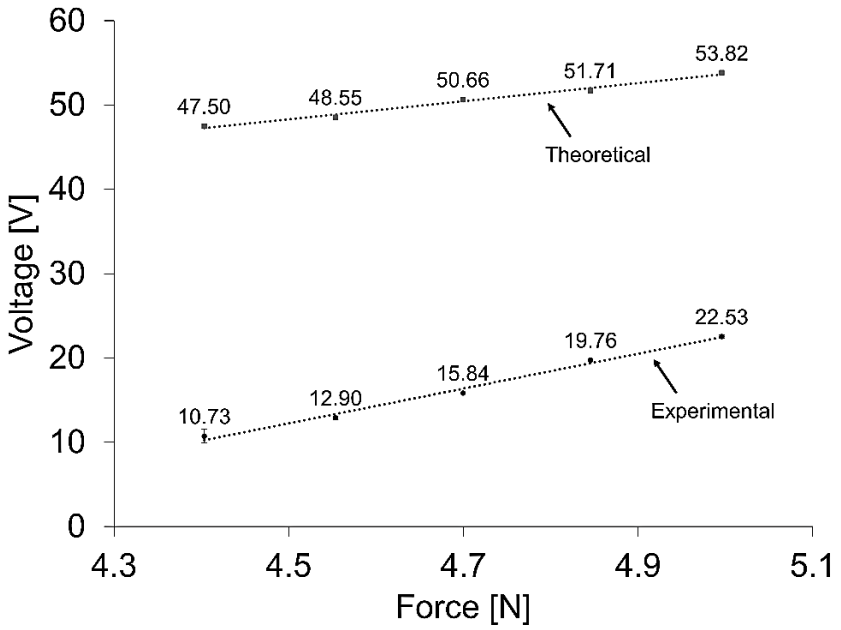

Figure 3.6. Theoretical and experimental comparison of dependence of open-circuit voltages of a TENG on contact force.

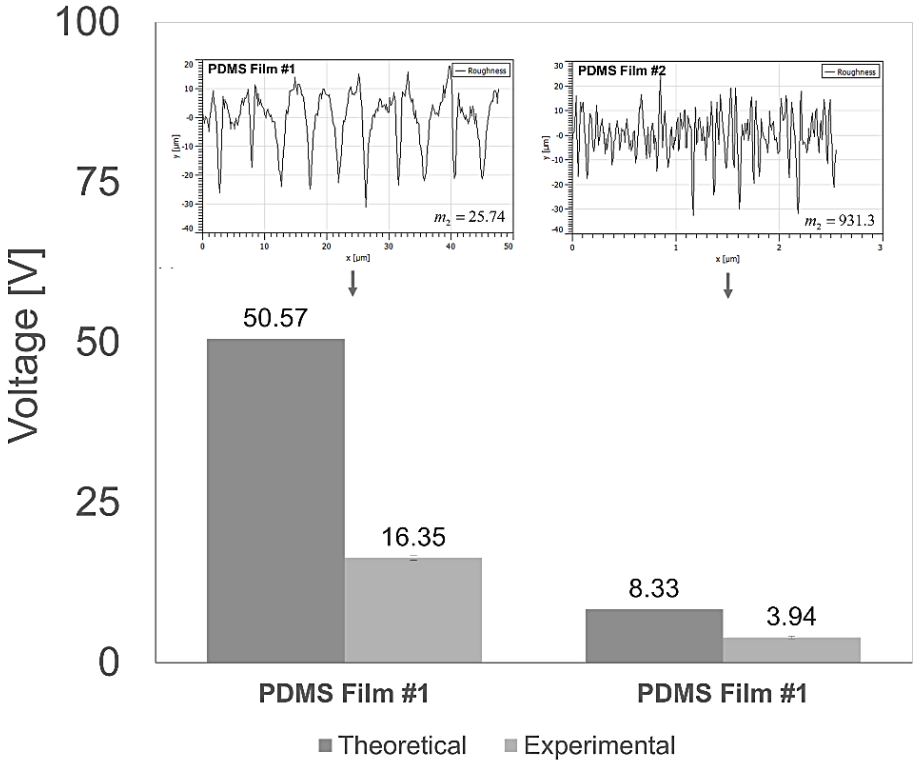

Figure 3.7. Theoretical and experimental comparison of open-circuit voltage of TENGs made from two different PDMS films. Inset: Roughness profiles of the two PDMS films.

3.4 SUMMARY

A triboelectric charge – contact force relationship for a contact-mode TENG is presented by combining the theories of insulator contact charging and contact mechanics. Experiments have been successfully performed to verify the theoretically expected results in two cases: (a) varying contact force, while keeping the surface profile constant, and (b) varying the surface profile, while keeping the contact force constant. The theory presented here can serve as an important guide in the design of the TENG structure for specific applications and self-powered systems.

4.0 DESIGN OF SIMULATION EXPERIMENTS TO PREDICT TRIBOELECTRIC GENERATOR OUTPUT USING STRUCTURAL PARAMETERS

4.1 INTRODUCTION

Contact electrification or triboelectric effect is one of the oldest and most universally existing phenomena, and has attracted many investigations. However, the underlying mechanism of charge transfer between two contacting surfaces when at least one of them is insulating, remains an unresolved problem in physics (as discussed in chapter 3.0) The governing phenomena spans different scales of material behavior, and several competing possible mechanisms such as electron transfer, ion transfer, bond dissociation, chemical changes to surface, and material transfer, have been proposed. Depending on structure and morphology of insulating materials, and environmental conditions, different mechanisms may be involved [46, 66, 86, 87]. Characterizing the charged surfaces and studying the charge transfer mechanisms often requires specialized equipment [88]. Owing to these uncertainties, determining and controlling surface charge density is a significant problem, making prediction of the output voltage of a triboelectric generator a challenge. Therefore, the electrodynamics based *V-Q-x* theoretical model described by equation (3-1), although helpful as a guide in rational design of the triboelectric generator (TG) structure, is not sufficient to appropriately predict the output voltage of a contact-mode TG. This problem also extends to finite element simulations, wherein triboelectric charge density (σ) is a boundary condition. Finite element simulations of the electric potential distribution in triboelectric

nanogenerators performed by assuming triboelectric surface charge densities serve the purpose of validating the working principle, but do not produce realistic predictions [31, 89, 90]. It should also be noted that contact force plays an important role in charge generation. The output voltage increases with increase in contact force, as the effective contact area between the dielectric layers increases due to distortion of one or both surfaces on a microscopic scale, resulting in an increase in the charges transferred [28, 31]. In addition, structural parameters such as area, gap, and dielectric thickness, which affect the output voltage of the generator, have previously been investigated individually but their interaction effects have not been considered.

During recent years, efforts have been made in the direction of finding optimum load capacitance and resistance and their dependence on TG's structural parameters and operating conditions [56, 91]. Finding optimum load capacitance is important because storage elements such as capacitors or batteries are necessary to stabilize and regulate output to power electronic devices because of the intrinsic unstable characteristics of various mechanical energy sources. Finding optimum load resistance is required to achieve maximum instantaneous power. The influence of the gap and dielectric thickness on optimum load resistance for maximum instantaneous power has been investigated by varying both parameters simultaneously, thus making it difficult to determine how each parameter contributes to the change in the output power. In another study, the impact of gap and area on performance of single electrode triboelectric nanogenerators has been investigated by varying one parameter at a time [92]. This approach does not take parameter interactions into account. To effectively design a contact-mode TG for an application, it is necessary to have a better understanding of how the output response of the TG is affected by variations in different structural design parameters. One effective way of accomplishing this is to use design of experiments (DOE) methodology to run finite element simulations, wherein

experimentally derived σ is used as a boundary condition. A well-designed simulation study can provide a great deal of information about input factors on responses than would otherwise be possible, while providing insights that cannot be gathered from trial-and-error approaches and by sampling one factor at a time. DOE methods are selected to conduct a set of simulation runs to generate a response, i.e., output voltage. Then, the simulation results are analyzed to derive a metamodel that approximates the relationship between the input parameters and the responses with statistical models (typically regression models) [93]. Such a metamodel can help reduce computational and experimental efforts in the process of designing a contact-mode TG.

Accordingly, presented here is a method to design finite element simulations of triboelectric generators, wherein experimentally derived surface charge density is used as a boundary condition. Two metamodels have been established because of a 2^3 full factorial design and a central composite design. The models have been experimentally verified, and have shown to predict the output voltage within one order of magnitude. In essence, structural design parameters of a contact-mode TG with a selected set of materials are investigated by designing finite element simulation runs, to arrive at metamodels. These metamodels, once verified experimentally, can be used as an effective design tool to not only predict the response of a contact-mode TG, but also to select optimum values of the structural parameters within the simulated design space. In this regard, the next section of this chapter is devoted to outlining the method, wherein selection of structural design parameters and response, finite element simulation model set-up, design methods used, and prototype fabrication and experimental procedure, are discussed. Thereafter, data analysis and experimental verification of the metamodels derived from it are presented, followed by the summary section.

4.2 METHODS

The flowchart of the systematic approach for creating the aforementioned design tool for a contact-mode TG system is shown in Figure 4.1. Briefly, the complete process requires the following steps, with further details presented in the succeeding sections.

i. Define the materials and operating conditions of the contact-mode TG system that needs to be studied. These are generally dictated by the application. For this study, polyethylene terephthalate (PET) and polyimide films are selected based on their position in the triboelectric series [65, 94] and ease of handling during fabrication. Gold (Au) is selected as the material for metal electrode, which can be easily deposited on the selected dielectric film. The contact-mode TG is operated in ambient conditions under a contact-separation frequency of 0.33Hz. As the frequency of contact-separation increases, the output voltage of the TG increases. A low operating frequency is therefore selected to ensure that the method described here is applicable for most practical applications. Most machinery equipment has a frequency of 100 Hz or higher, whereas human motion exhibits a much lower frequency (<10Hz) [50].

ii. Clarify the selection of input parameters or factors, their range of variability, i.e., design space, and the system response to be studied.

iii. Select a design method based on which the simulation runs should be executed.

iv. Set-up and run the finite element simulation model

v. Analyze the simulation data to generate metamodels.

vi. Conduct experiments using the TG system defined in step (i), while changing structural parameters as appropriate and feasible, in order to verify the metamodels generated in step (v), which can then be used as a design tool within the simulated design space.

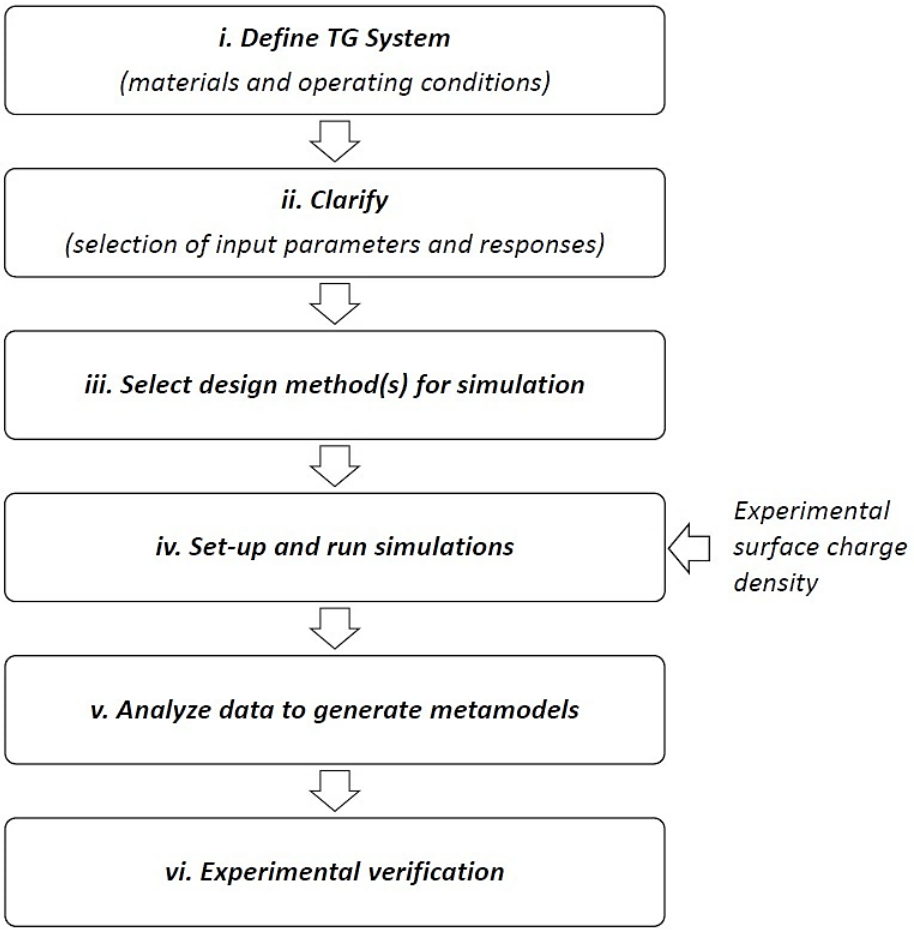

Figure 4.1. Method flowchart

4.2.1 Selection of factors and response

Considering the theoretical model discussed above, area, gap, and dielectric thickness, are selected as the structural design factors. Electric potential or voltage between the electrodes is selected as the response for this study. The next step is to define the design space or region of interest for each input factor. This decision is guided by the main effect of a single factor, which is the effect of that factor considered independently on the response. This is done by performing finite element simulations on the model described in section 2.2. Other considerations involved are related to

geometrical restrictions depending on application. Table 4.1 shows the minimum (low setting) and maximum (high setting) values selected for each factor, and Figure 4.2 shows the simulation results for main effects of each factor. For this study, the geometrical restrictions of the test set-up and material availability were also considered before finalizing the factor ranges for further simulation runs. For example, although a thicker film would enhance the output voltage of the TG, as seen from (3-1) and Figure 4.2 (c), it would require a large separation distance between the two electrodes, which would increase the size and weight of the device. This is a potential deterrent for many portable applications, and in general can be considered as a drawback for vertical contact-separation mode TG. It is known that charge increases as the thickness of the film decreases, and does not reach saturation for the thinnest films [67]. Therefore, 50.8 μm to 508 μm dielectric thickness range is selected. Although this range does not affect the output voltage as seen from Figure 4.2(c), it is necessary to investigate any significant interaction effects in this range.

Table 4.1. Input factors with minimum (low) and maximum (high) settings.

Input Factors	**Minimum Value (Low setting)**	**Maximum Value (High setting)**
Area (A)	6.45 cm^2	58.06 cm^2
Gap (x)	2.54 mm	25.4 mm
Dielectric Thickness (d)	50.8 μm	508 μm

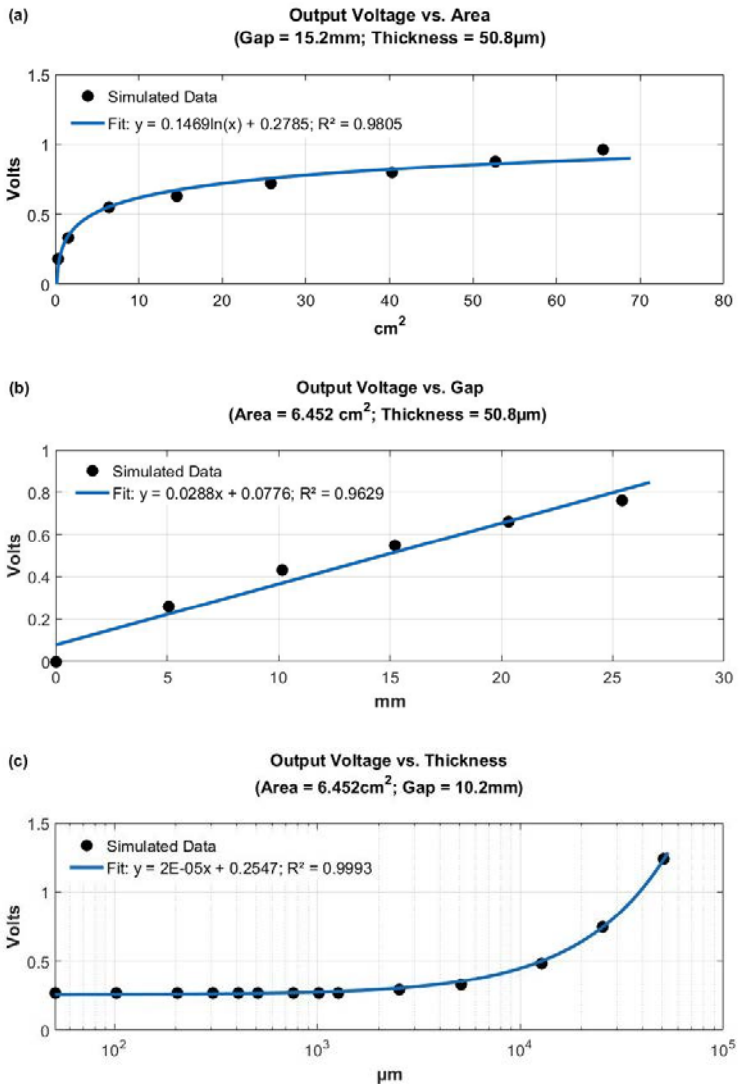

Figure 4.2. Main effects of (a) area (b) gap, and (c) dielectric thickness on output voltage of triboelectric generator.

4.2.2 Finite element simulation model

A generic three-dimensional (3D) finite element model (FEM) for a dielectric-to-dielectric contact-mode TG with PET and polyimide films, and two Au electrodes were constructed as shown in Figure 4.3, and appropriately meshed. One of the electrodes is connected to ground, and the PET and polyimide films are given experimentally obtained value of triboelectric surface charge

density. A contact-mode TG with approximate area of 4cm x 6.5cm and thickness of 50µm for the aforementioned dielectric films which are deposited with Au electrodes was fabricated and tested under a 0.33 Hz frequency of contact-separation (refer section 2.4. for details). The measured open circuit peak voltage was 0.372 V. This output voltage of the TG is proportional to the surface charge density. The magnitude of surface charge density (328.5 pCm^{-2}) is thus calculated by substituting this voltage value in equation, $V_{OC} = \sigma x / \varepsilon_0$ ($Q = 0$ at open circuit condition), where variables have been defined in equation (3-1), and x is equal to 10mm, which is the maximum separation between the two dielectric films dictated by the test set-up.

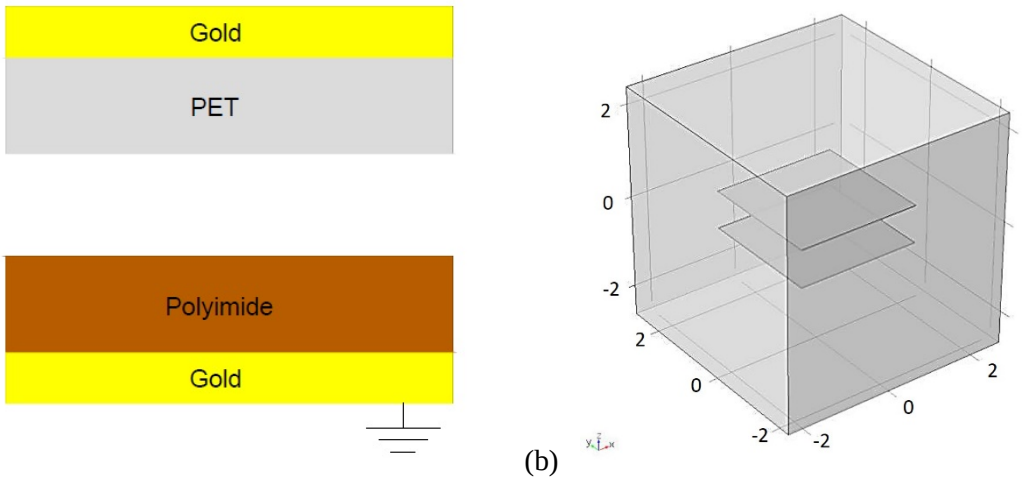

Figure 4.3. (a) Schematic diagram of the finite element model. (b) A 3D FEM constructed with an air box surrounding it.

4.2.3 Design of simulation experiments

DOE is an effective tool for maximizing the amount of information gained from a study while minimizing the amount of data to be collected [95]. DOE proposes fractional experimental designs which help investigate the effects of many different factors by varying them simultaneously instead

of changing only one factor at a time. Factorial designs allow estimation of the sensitivity to each factor and to the combined effect of two or more factors. The input variables on the experiment are called factors, and the performance measures resulting from the experiment are called responses. Polynomial equations, which are Taylor series approximations of the unknown true functional form of the response variable, are used to model the response [96]. The response variable Y as a function of the input factors $X's$ (shown to the third order here), is given by:

$$Y = \beta_0 + \sum_{i=1}^{p} \beta_i X_i + \sum_{i=1}^{p}\sum_{j=1}^{p} \beta_{ij} X_i X_j + \sum_{i=1}^{p}\sum_{j=1}^{p}\sum_{k=1}^{p} \beta_{ijk} X_i X_j X_k + \cdots \quad (4\text{-}1)$$

where $i \neq j \neq k$, p = number of factors to be studied, β_0 = the overall mean response, β_i = the main effect for factor (i = 1, 2, …, p), β_{ii} = the two-way interaction effects between the i^{th} and j^{th} factors, and β_{ijk} = the three-way interaction effects between the i^{th}, j^{th}, and k^{th}, factors. Analysis of Variance (ANOVA) and t-test are the methods used to test whether an effect is significant.

Two experimental design techniques are used in this study, wherein "experiment" is execution of a computer simulation model. Each experimental condition with a unique combination of factor levels is called a "run" and the entire set of runs is the "design". A design is a matrix where every column corresponds to a factor, and the entries within the column correspond to settings or levels for that factor. Each row then represents a specific combination of factor levels, and is called a "design point". Replication allows us to check the homogeneity of variance assumption and is used to increase the precision of the experiment by giving more accurate effect estimates by reducing the underlying standard errors associated with the $\beta's$. Replication is incorporated into the experimental design in this study by performing 3D evaluation of simulation

results to obtain additional response values for a single design point at different coordinates, within the central region of the upper dielectric-electrode structure, as shown in Figure 4.4.

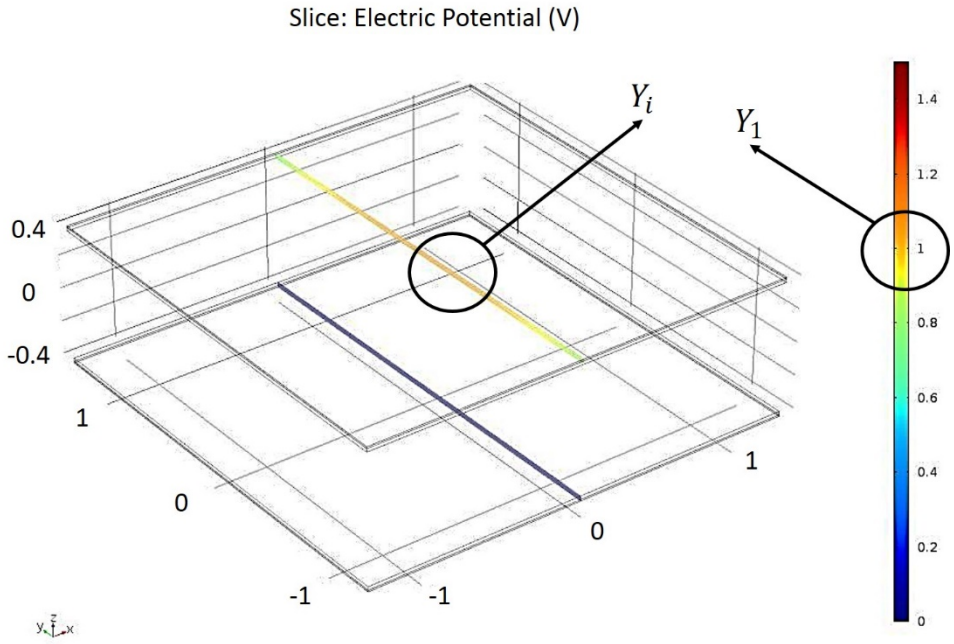

Figure 4.4. Example of a simulation result for a unique combination of factor levels. $\boldsymbol{Y_1}$ is taken as one response, and $\boldsymbol{Y_i}$ are taken as replicates ($\boldsymbol{i = 2, 3, 4}$ ...), obtained by 3D evaluation of the center region of the upper dielectric-electrode structure.

A 2^3 full factorial design, implying three factors with two levels for each factor is implemented with 5 replicates. The levels are low and high values of the selected input factors often coded as -1 and +1, respectively. Refer table 1 for these values. There are eight different ways of combining high and low settings of Area (A), Gap (x), and Dielectric Thickness (d), to arrive at a response, i.e., output voltage (V). Conceptually, these high and low settings of the factors can be shown at the corners of a cube. A 2^3 design therefore implies eight runs. 5 replicates make the total number of runs equal to 48. The orthogonality property of this design makes the analysis

of the simulation response straightforward because each main effect and interaction can be estimated independently, as pairwise correlation between any two columns (factors) is equal to zero. For this design, there are three main effects, three two-factor interactions, and a three-factor interaction.

A central composite design (CCD) is implemented to estimate any quadratic effects, in addition to main effects and interaction effects. CCD design in this case, is the 2^3 design augmented with six center points and six axial points to allow estimation of curvature, making the total number of runs for this design equal to 20. The axial points represent the new settings for each factor in the design. The low and high factor settings given in table 1 are considered to be the limits, and taken as the axial points for this design. If the distance between the central point of the design space, i.e., (0, 0, 0), and each full factorial sample is normalized to 1, then the six axial points are (±1, 0, 0), (0, ±1, 0), and (0, 0, ±1). The eight corner points of the cube are obtained by assigning each of the three factors a level setting of $+c$ and $-c$ ($|c| < 1$), and combining these settings in eight different ways, essentially creating a 2^3 design cube within the design space. The value of c is taken to be 0.5946. A quadratic model is frequently used to estimate the response surface, and is given by:

$$Y = \beta_0 + \sum_{i=1}^{p} \beta_{\mathrm{i}} X_{\mathrm{i}} + \sum_{i=1}^{p} \sum_{j=1}^{p} \beta_{ij} X_{\mathrm{i}} X_j + \sum_{i=1}^{p} \beta_{ii} X_{ii}^2 \qquad (4\text{-}2)$$

where $i \neq j$, p = number of factors to be studies, β_0 =the overall mean response, β_{i} = the main effect for factor (i = 1, 2, …,p), β_{ij} = the two-way interaction effects between the i^{th} and j^{th} factors, and β_{ii} = the quadratic effect for the i^{th} factor.

The simulation responses collected for all the aforementioned designs are analyzed to create metamodels. To remove non-significant terms from the 2^3 model, backward stepwise elimination is performed with 'alpha-to-remove' equal to 0.1, which means that any term with a p-value greater than 0.1 will be removed from the model. Main effects and interaction plots are generated, and the model accuracy is tested using residual plots, used to validate assumptions of normal distribution, constant variance, and independence for ANOVA analysis. The residual in regression analysis is the difference between the observation value and the fitted value. Box-Cox transformation on the response data is performed if the model assumptions are not met [97].

4.2.4 Prototype fabrication and experimental procedure

In order to perform experimental verification of the metamodels, two different TG configurations are implemented and tested. The parameters for the two prototypes are given in table 2. PET and Polyimide dielectric films are cut in rectangles of desired sizes, and deposited with a thin gold (Au) film on one side by sputter coating. The Au film serves as a metal electrode. The non-coated side of the dielectric film serves as the contact side. Wires are connected to the electrode side to connect the output of the TG device to an oscilloscope. The electrode side of both dielectric films are attached onto a suitable rigid substrate such as acrylic. Once the two halves of the TG are fabricated, they are assembled on the experimental set-up with the desired maximum separation distance between them.

The schematic of the experimental set-up used to measure the output voltage of the two fabricated TG prototypes is shown in Figure 4.5. The two samples are brought into contact, such that the dielectric surfaces are parallel and their centers coincide. The lower sample is stationary,

while the upper sample is moved up and down via a variable speed platform, thus creating repetitive contact-separation cycles, forming a TG. The frequency of the variable speed platform is set at 0.33 Hz for all experiments, as this is the setting that was used to calculate the surface charge density (discussed in section 4.2.1.), ensuring that the contact force is consistent for all experiments. The output of the TG is connected to an oscilloscope which measures the voltage pulses generated. At least 40 observations of output voltage peaks are collected and analyzed to calculate means and standard deviations.

Table 4.2. Prototype parameters for experimental verification testing.

Prototype parameters	**TG Prototype 1**	**TG Prototype 2**
Dielectric 1	PET (ε_{r1} = 3.1)	PET (ε_{r1} = 3.1)
Dielectric 2	Polyimide (ε_{r2} = 3.4)	Polyimide (ε_{r2} = 3.4)
Area	~ 25 cm^2	~ 6.45 cm^2
Maximum separation distance	~ 4 mm	~ 12.5 mm
Dielectric thickness	~ 50.8 µm	~ 50.8 µm
Contact-separation frequency	~ 0.33 Hz	~ 0.33 Hz
Metal electrodes	Au (sputter coated)	Au (sputter coated)

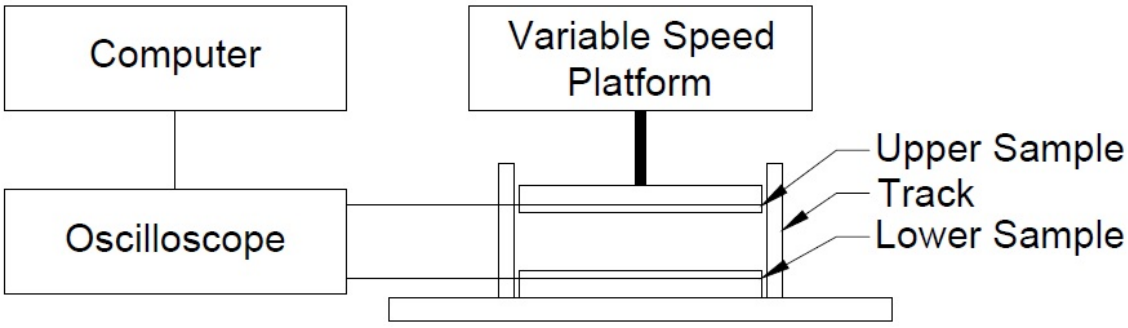

Figure 4.5. Schematic of the experimental set-up.

4.3 RESULTS

4.3.1 2^3 full factorial design model

The design matrix with simulated responses using 2^3 full factorial design with five replicates is shown in Table 4.3. The Box-Cox transformation ($T(V) = (V\hat{}\lambda - 1)/\lambda$) is performed to transform the response data into normality, using a transformation parameter, $\lambda = -0.3$. The corresponding model is given by:

$$-V^{0.3} = -1.35775 + 0.069014\,A + 0.325092\,x + 0.002730 + 0.039174\,Ax + 0.001418\,Ad - 0.003997\,xd \quad (4\text{-}3)$$

The factorial regression analysis removes the three-way interaction term from the model via backward stepwise elimination. All other terms are significant ($p < 0.01$). However, the coefficients of d and its interactions although significant, are orders of magnitude smaller compared to the coefficients of constant, A and x. This is also seen in the main effects and interaction plots in Figure 4.6(a) and (b), respectively, wherein change in V due to change in d is negligible. Factor x has the most influence on response V, followed by factor A. The model $R^2 = 0.999$ and $R^2_{adj} = 0.999$. No difference between R^2 and R^2_{adj} means that there are no non-significant terms in the model. In addition to equation (4-3), the contour plot of V vs. x, A, shown in Figure 4.6(d) can also be used to estimate the output voltage of the TG, within the design space. The contour plot shows that V increases with increase in x and A. For example, when A and x are at high settings, i.e, $A = 58.06\text{cm}^2$ and $x = 25.4$ mm, $V > 1.2$ Volts. Similarly, contour plots of

V vs. x, d and V vs. A, d can be made, as needed. Figure 4.6(c) shows the residual plots for V in the model given by equation (4-3). There does not seem to be any great deviation in the normal probability plot of the residuals. The Standardized Residuals vs. Fits plot and Standardized Residuals vs. Observation Order plot do not show any strong patterns. Thus, the model can be considered valid.

Table 4.3. The design matrix with simulated responses using 2^3 full factorial design with five replicates.

Run no.	A	x	d	V
1	-1	-1	-1	0.160
2	1	-1	-1	0.180
3	-1	1	-1	0.600
4	1	1	-1	1.200
5	-1	-1	1	0.160
6	1	-1	1	0.180
7	-1	1	1	0.600
8	1	1	1	1.200
9	-1	-1	-1	0.166
10	1	-1	-1	0.185
11	-1	1	-1	0.659
12	1	1	-1	1.322
13	-1	-1	1	0.170
14	1	-1	1	0.193
15	-1	1	1	0.649
16	1	1	1	1.319
17	-1	-1	-1	0.166
18	1	-1	-1	0.185
19	-1	1	-1	0.659
20	1	1	-1	1.321
21	-1	-1	1	0.171
22	1	-1	1	0.194
23	-1	1	1	0.648
24	1	1	1	1.320
25	-1	-1	-1	0.166
26	1	-1	-1	0.185
27	-1	1	-1	0.659
28	1	1	-1	1.322
29	-1	-1	1	0.170
30	1	-1	1	0.193
31	-1	1	1	0.649
32	1	1	1	1.319
33	-1	-1	-1	0.166
34	1	-1	-1	0.185
35	-1	1	-1	0.660
36	1	1	-1	1.322
37	-1	-1	1	0.167
38	1	-1	1	0.190
39	-1	1	1	0.649
40	1	1	1	1.318
41	-1	-1	-1	0.166
42	1	-1	-1	0.185
43	-1	1	-1	0.659
44	1	1	-1	1.322
45	-1	-1	1	0.170
46	1	-1	1	0.193
47	-1	1	1	0.649
48	1	1	1	1.320

(a) Main Effects Plot for V

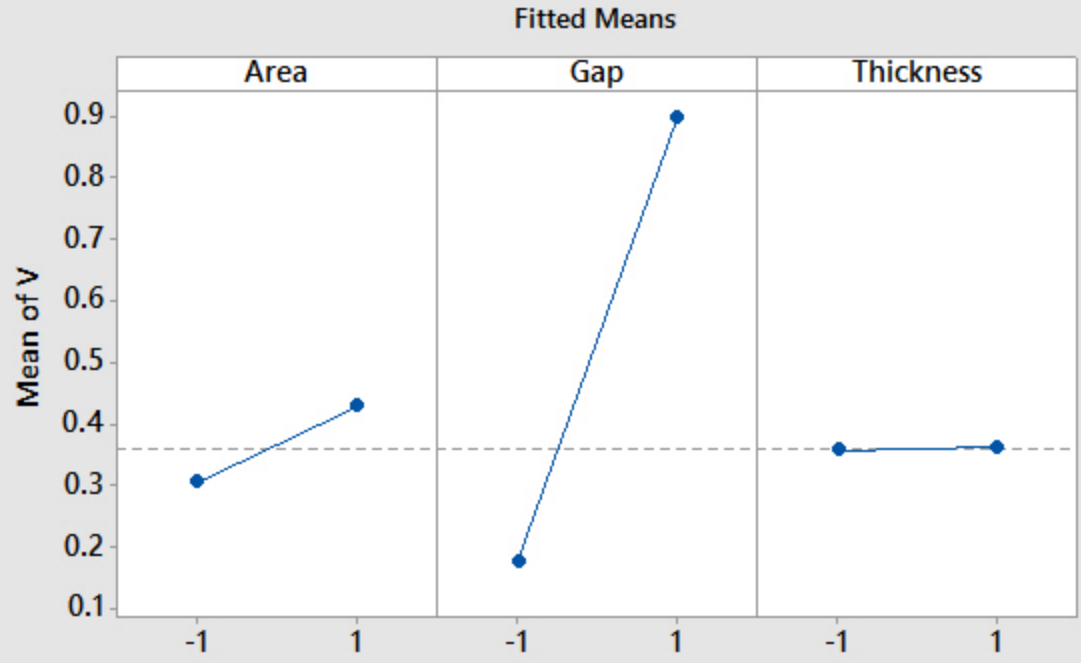

(b) Interaction Plot for V

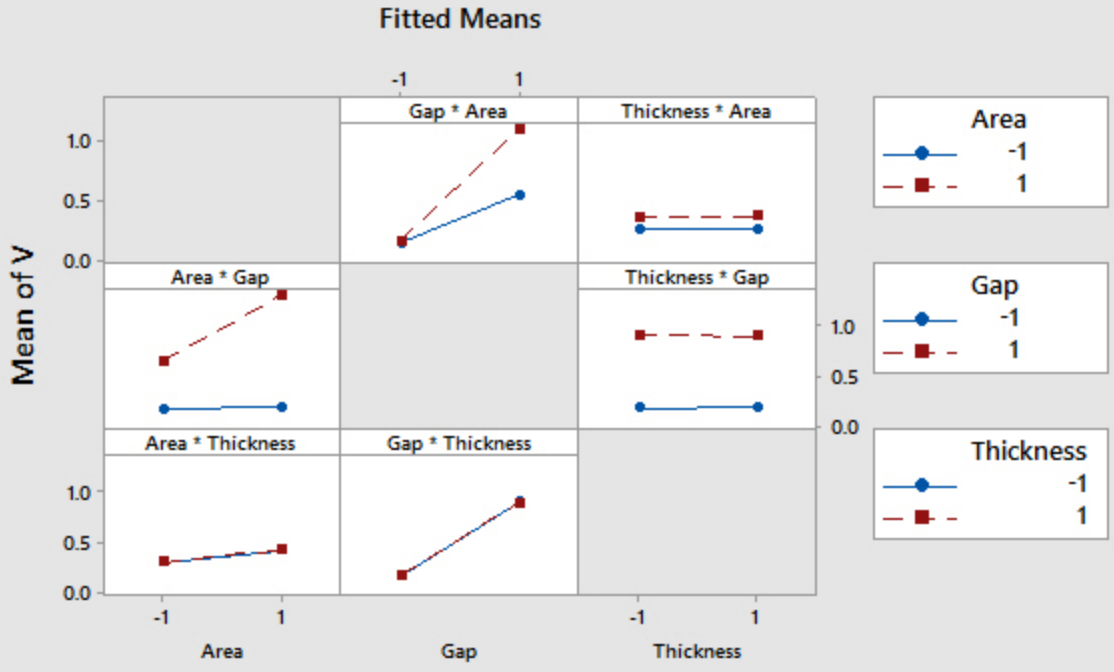

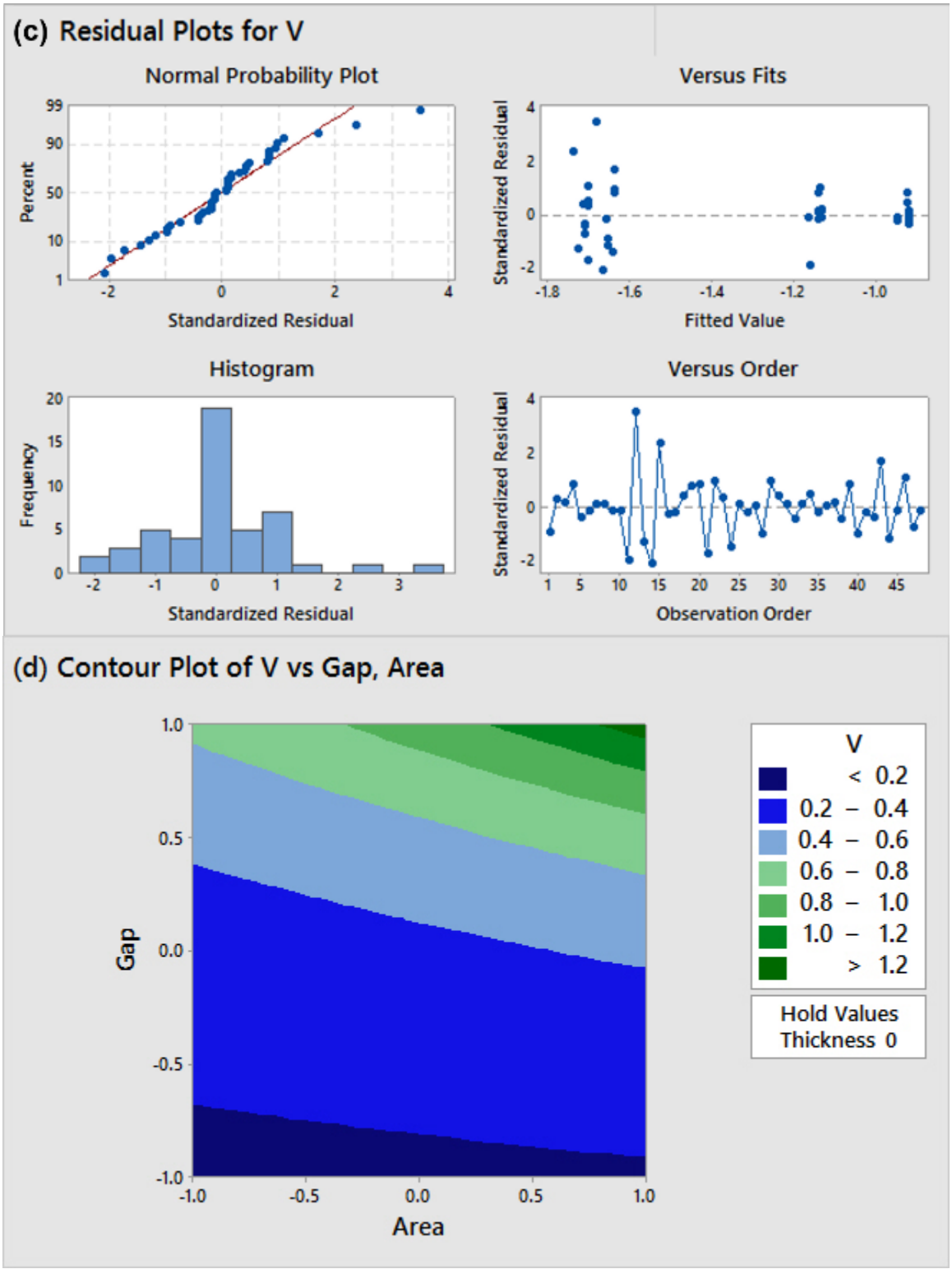

Figure 4.6. (a) Main effects plot, (b) Interaction plot, (c) Residual plots, and (d) Contour plot of Voltage vs. Gap, Area for 2^3 full factorial design.

4.3.2 Central composite design model

The design matrix with simulated responses using CCD design is shown in table 4 in supporting information. The corresponding model is given by:

$$V = 0.70053 + 0.08228\,A + 0.40381x + 0.0403\,A^2 - 0.1197\,x^2 - 0.0097d^2 + 0.1061\,Ax \quad (4\text{-}4)$$

The response surface regression analysis removes terms d, Ad, and xd from the model, as their coefficients are zero. This is also seen in the main effects and interaction plots in Figure 4.7(a) and (b), respectively, wherein change in V due to change in d is negligible. Minor quadratic effects of A, x, and d are detected by this design. Factor x has the most influence on response V, followed by factor A. The model $R^2 = 0.995$ and $R^2_{adj} = 0.990$. The small difference between R^2 and R^2_{adj} means that the probability of having non-significant terms in the model is negligible. In addition to equation (4-4), the contour plot of V vs. x, A shown in Figure 4.7(d) and the surface plots shown in Figure 4.8 can also be used to estimate the output voltage of the TG, within the design space. The contour plot shows that V increases with increase in x and A. For example, when A and x are at high settings, i.e, $A = 58.06\text{cm}^2$ and $x = 25.4$ mm, $V > 1.2$ Volts. Similarly, contour plots of V vs. x, d and V vs. A, d can be made, as needed. Figure 4.7(c) shows the residual plots for V in the model given by equation (4-3). There does not seem to be any great deviation in the normal probability plot of the residuals. The Standardized Residuals vs. Fits plot and Standardized Residuals vs. Observation Order plot do not show random patterns. Thus, the model can be considered valid.

(a) Main Effects Plot for V

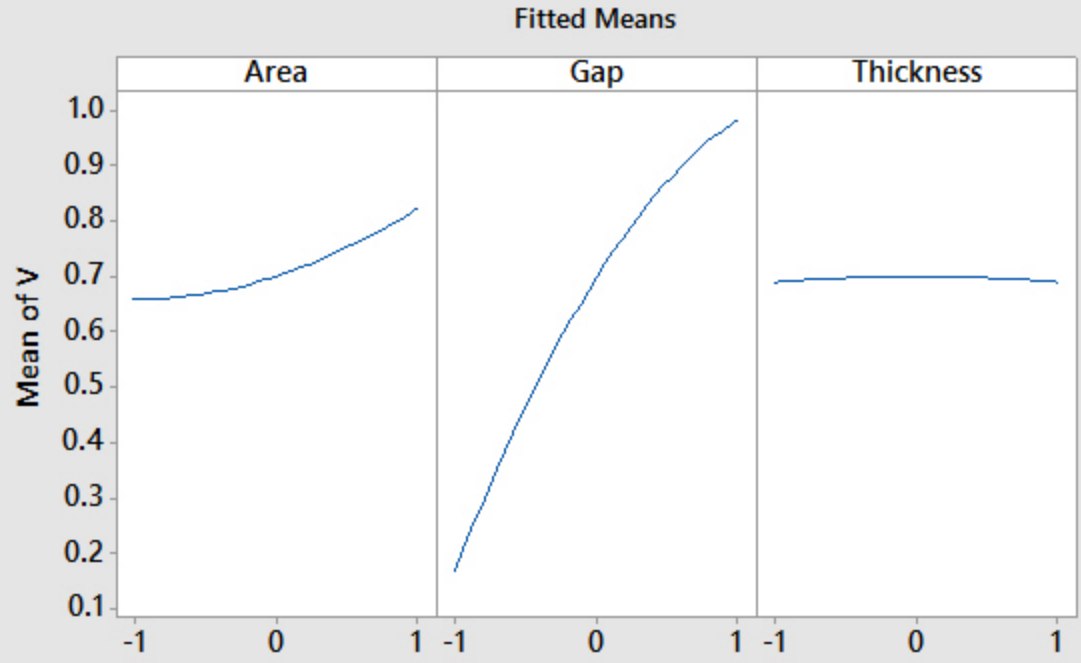

(b) Interaction Plot for V

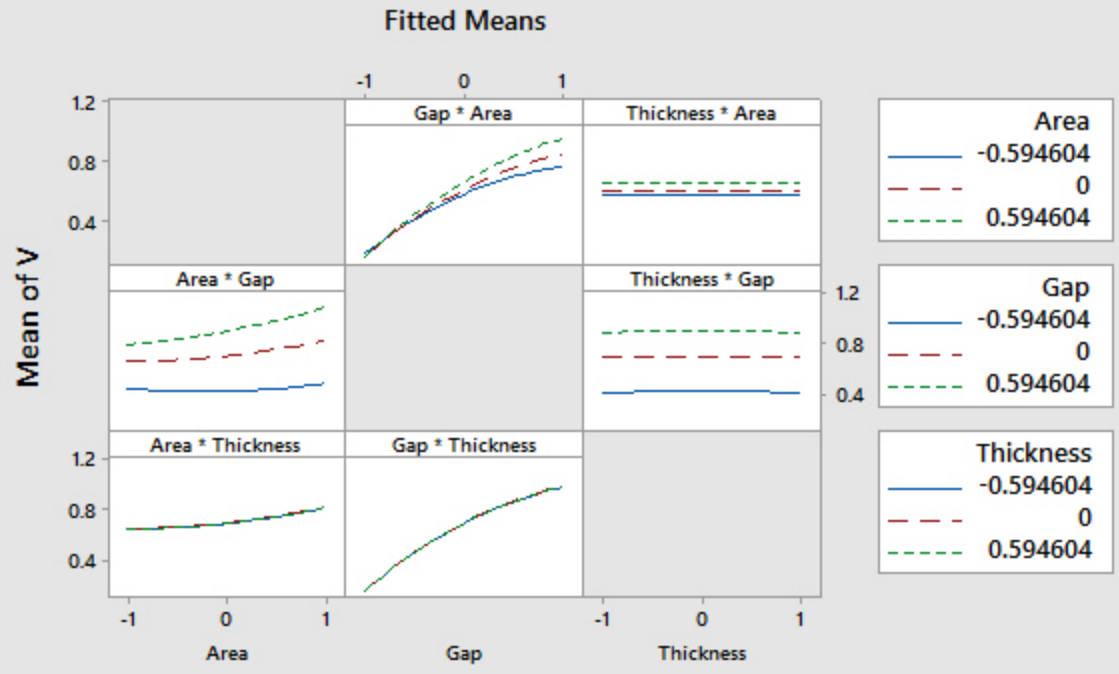

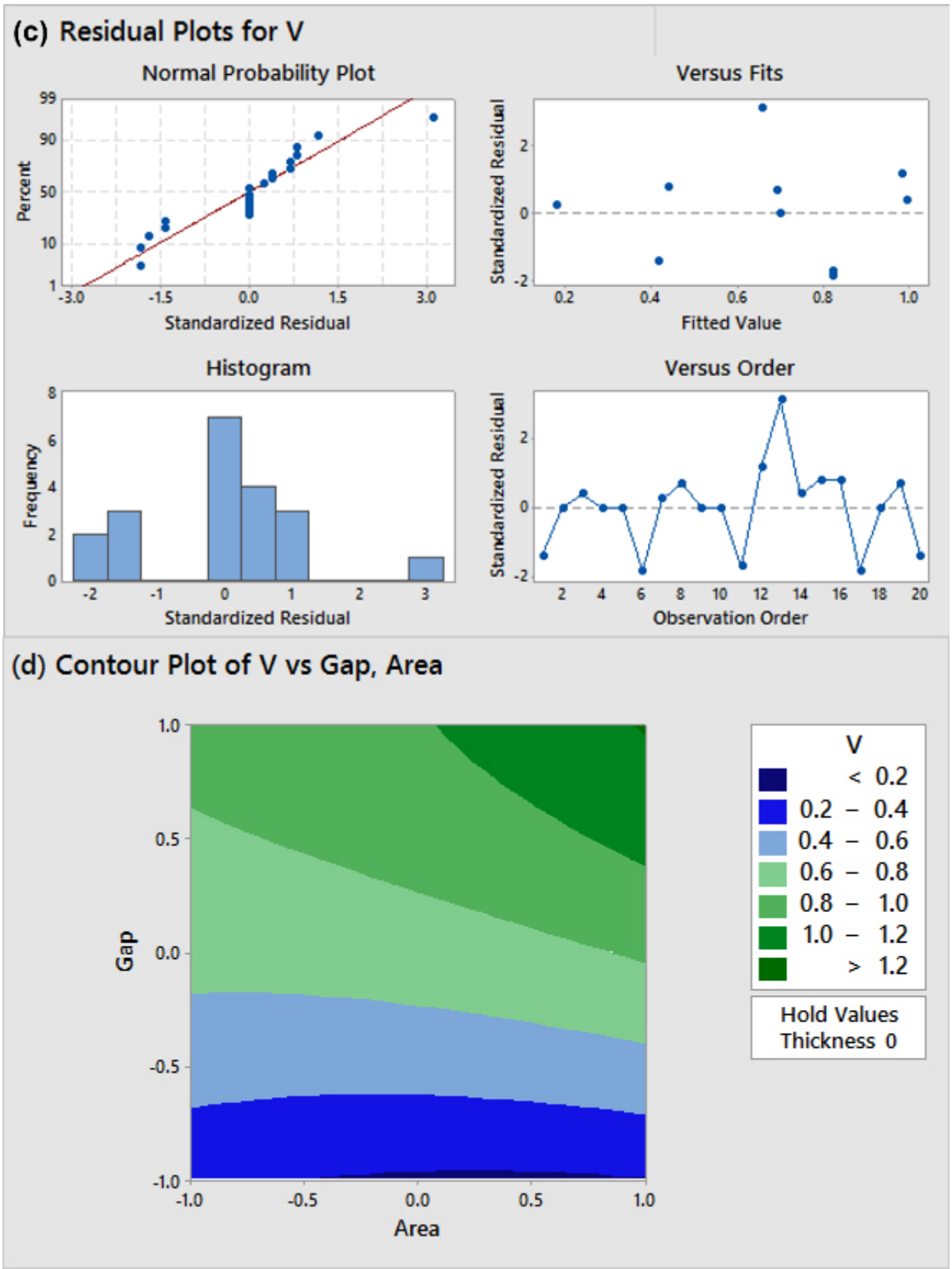

Figure 4.7. (a) Main effects plot, (b) interaction plot, (c) Residual plots, and (d) Contour plot of Voltage vs. Gap, Area for CCD design.

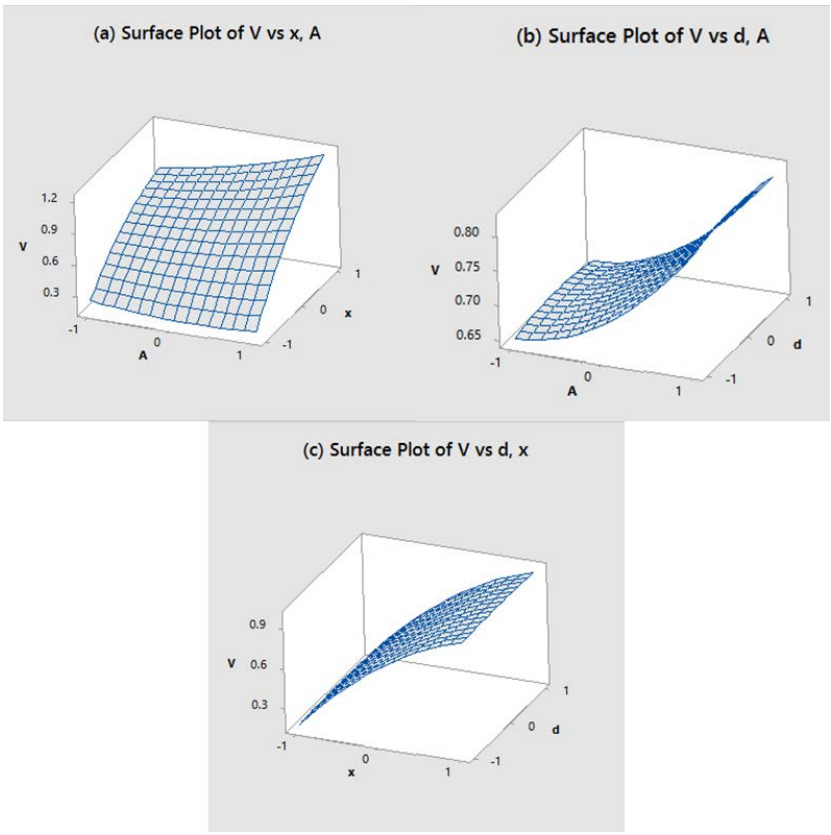

Figure 4.8. Surface plots of V vs. (a) x, A, (b) d, A, and (c) d, x.

Table 4.4. The design matrix with simulated responses using central composite design.

Run no.	A	x	d	V
1	-0.5946	-0.5946	-0.5946	0.4
2	0.5946	-0.5946	-0.5946	0.45
3	-0.5946	0.5946	-0.5946	0.8
4	0.5946	0.5946	-0.5946	1
5	-0.5946	-0.5946	0.5946	0.4
6	0.5946	-0.5946	0.5946	0.45
7	-0.5946	0.5946	0.5946	0.8
8	0.5946	0.5946	0.5946	1
9	-1	0	0	0.7
10	1	0	0	0.8
11	0	-1	0	0.18
12	0	1	0	1
13	0	0	-1	0.7
14	0	0	1	0.7
15	0	0	0	0.7
16	0	0	0	0.7
17	0	0	0	0.7
18	0	0	0	0.7
19	0	0	0	0.7
20	0	0	0	0.7

4.3.3 TG configuration and measurements

Two different configurations of TGs, described in section 4.2.4, were fabricated and tested. For a sample size of 48, the mean peak output voltage for TG prototype 1 is 0.280 volts and the standard deviation (SD) is 0.03 volts. For a sample size of 40, the mean peak output voltage for TG prototype 2 is 0.242 volts and standard deviation is 0.02 volts. Experimental results are compared to model predictions in Table 4.5. Both models predict the output of the TG within one order of magnitude.

Table 4.5. Experimental results vs. Model predictions

TG Prototype Number	**Peak Output Voltage** *(volts)*		
	Experimental	**Metamodel Predictions**	
		2^3	**CCD**
Prototype 1	0.280 (n = 48, SD = 0.03)	0.186	0.258
Prototype 2	0.242 (n = 40, SD = 0.02)	0.283	0.614

4.4 SUMMARY

The results from both designs, 2^3 full factorial and CCD, show similar findings. Both designs show that x is the most influential structural parameter for a contact-mode TG, followed by A, and that d has negligible effect on the output voltage of TG. Contour and surface plots provide a nice way of looking at the response as a function of two factors at a time, and can be used to select possible combinations of the structural parameters that result in the desired output voltage depending on

the application. This can help in optimization and design trade-off decisions, by allowing focus on interesting features of the response surface landscape such as peaks, flats, or threshold regions, without considering the specific form of the regression model.

A noteworthy point is that 2^3 designs are most efficient if we can assume that the simulation response is well-fit by a model with only linear main effects and interactions, i.e., the simulation behavior for factor combinations in the interior of the design space is not known. CCD design does help in estimating any quadratic effects, but for greater detail about the response, finer grids such as m^p factorial designs can be used, where larger the value of m, better the space-filling properties of the design. This however comes with massive data requirements, leading to a higher computational and experimental burden. Sometimes when there are factors that take only a few levels or are not as significant as other factors for a given design space, mixed-level or mixed-gridded factorial design can be used. For example, for the study presented here, x and A can have multiple levels, and d may only have 2 levels, thereby generating a $(m^p)(2^1)$ design, where $p = 2$ and $m > 3$ (replicated as needed to gain enough data to achieve narrow confidence intervals and powerful hypothesis tests). Simple designs are chosen for this study to emphasize the effectiveness of the method presented. For a more extensive list of potential designs and relevant references, see Ref. [93].

In summary, a new method to design finite element simulation experiments to predict the output voltage of triboelectric generators using its structural parameters is presented. Due to the complex nature of the triboelectric phenomena, determining the surface charge density is a significant problem, making prediction of the output voltage a challenge, as previously discussed. Experimentally derived surface charge density is therefore used as a boundary condition in the simulations, resulting in real world output voltage predictions within one order of magnitude. The

metamodels generated using the method presented can be used to investigate virtual prototyping of the generator to understand the linear, quadratic, and interaction effects of the different structural design factors on its response. Computational and experimental efforts can be greatly reduced, as these simple metamodels can serve as an effective design tool in the simulated design space. The overall intention of this study is to show the benefits of (a) designing finite element simulations for a triboelectric generator, and (b) using experimental surface charge density as a boundary condition, thereby convincing you to use the method presented in your next triboelectric generator simulation study.

With respect to designing a wearable respiratory energy harvester (wREH), the simulations and experiments conducted in this chapter indicate that to increase the generator output (while keeping a small form factor), it is necessary to achieve (a) increase in the effective contact area *via* surface modification, and/or (b) increase in the separation distance between the contacting dielectric surfaces.

5.0 MEASUREMENT OF ABDOMINAL FORCE AND DISPLACEMENT DURING NORMAL RESPIRATION

5.1 INTRODUCTION

The preliminary study and the design of experiments discussed in chapters 2.0 and 4.0 respectively, indicate the potential of using a contact-mode triboelectric generator to harvest energy from respiration. To design a wearable respiratory energy harvester (wREH), it is necessary to better understand the abdomen motion during normal respiration in terms of the distance the abdomen moves and the force it generates. After an extensive literature search, no direct measurement of force generated on the anterior abdominal surface during normal breathing was found. Accordingly, after a brief background on respiratory motion, the experimental set-up used to measure the distance and force during respiration is presented along with the results obtained. These measurements are also used to determine the benchtop test setup parameters used for device characterization (discussed more in chapter 6.0).

The equation of motion of the respiration system during quiet breathing is given by a single first order differential equation [98-100]:

$$P_{(t)} = EV_{(t)} + R\dot{V}_{(t)} \tag{5-1}$$

where at any instant *t*, $P_{(t)}$ is the pressure exerted across the system that produces instantaneous air flow $\dot{V}_{(t)}$ and volume displacement $V_{(t)}$, and *E* and *R*, respectively, are the elastance and resistance

of the respiratory system. Any force applied to the respiratory system is either stored as elastic energy or dissipated as resistive energy. The elastic element of the respiratory system consists of the chest wall and the lungs. The resistive element are the conducting airways. The chest wall includes the thoracic cage and the abdominal compartment, which are arranged in parallel, since they undergo almost the same pressure and contribute different volumes. The primary task of the respiratory muscles (Figure 5.1(a)) is to serve the purpose of ventilation, by generating forces necessary to overcome both the elastic and resistive load of the respiratory system. The dome-shaped diaphragm is the most important inspiratory muscle. It is composed of muscle fibers that radiate from the central tendon to attach to the lower rib cage. The zone of apposition is where majority of the muscular portion of the diaphragm lies (Figure 5.1 (b)) [101].

The diaphragm exerts two types of forces upon contraction: (i) the muscle fibers shorten and force the dome to displace caudally, thus increasing the intra-abdominal pressure, which causes ventral displacement of the anterior abdominal wall. The net effect is the lowering of pleural pressure (P_{pl}) to effect lung expansion. Thus, diaphragmatic pressure increases the trans-diaphragmatic pressure (P_{di}), which is partially dependent on abdominal pressure (P_{ab}), as $P_{di} = P_{ab} - P_{pl}$. The schematic of pressures applied to chest wall are shown in Figure 5.1(c) [102].

Second, the contracting diaphragm exerts an appositional force. This is related to the configuration of the muscle fibers in the zone of apposition which, in contrast to fibers in the dome, have a much larger radius of curvature. Less pressure is therefore generated to move the diaphragm. The pleural space in the zone of apposition is exposed to approximate abdominal pressure, thereby acting directly to push the lower rib cage in an outward direction. Consequently, the pressure in pleural recess between the apposed diaphragm and the rib cage increases during inspiration. At the beginning of inspiration, both upper and lower rib cage tend to collapse as P_{pl}

becomes progressively more sub atmospheric. However, this expected tendency of the upper rib cage to collapse during diaphragmatic contractions because of the negative P_{pl} can be partly diminished by the mechanical interdependence with the lower rib cage, and even offset or reversed into outward motion by the compensatory contraction of the intercostal muscles. Thus, although the diaphragm is the primary muscle of respiration, intercostal and scalene muscles are also actively taking part in quiet respiration to aid in the movement of the chest wall.

The parasternal and external intercostals serve as primary inspiratory muscles by raising the ribs during contraction. In contrast, the internal intercostals, which run at right angles to the externals, serve an expiratory function by contracting during expiration to induce caudal motion of the lower ribs. The scalene muscles contraction also aids inspiration by expanding the rib cage. Several muscles serve an accessory role during periods of increased effort (i.e., exercise, fatigue). These muscles include the sternocleidomastoids, pectroralis minor, and erector spinae, all of which elevate the ribs during contraction.

The respiratory muscles of the abdominal wall, including the obliques, rectus abdominis, and transversus abdominis, are primary expiratory in function by the virtue of the increase in abdominal pressure upon contraction. They aid in unloading the inspiratory muscles during times of stress by their effects on lung volume. The abdomen thus plays a major role in respiratory mechanics. The abdomen, except for the diaphragm superiorly and the anterior abdominal wall, is an essentially incompressible compartment with fixed boundaries. Consequently, the movement of the diaphragm and thoracic cage is coupled with movement of anterior abdominal wall [103].

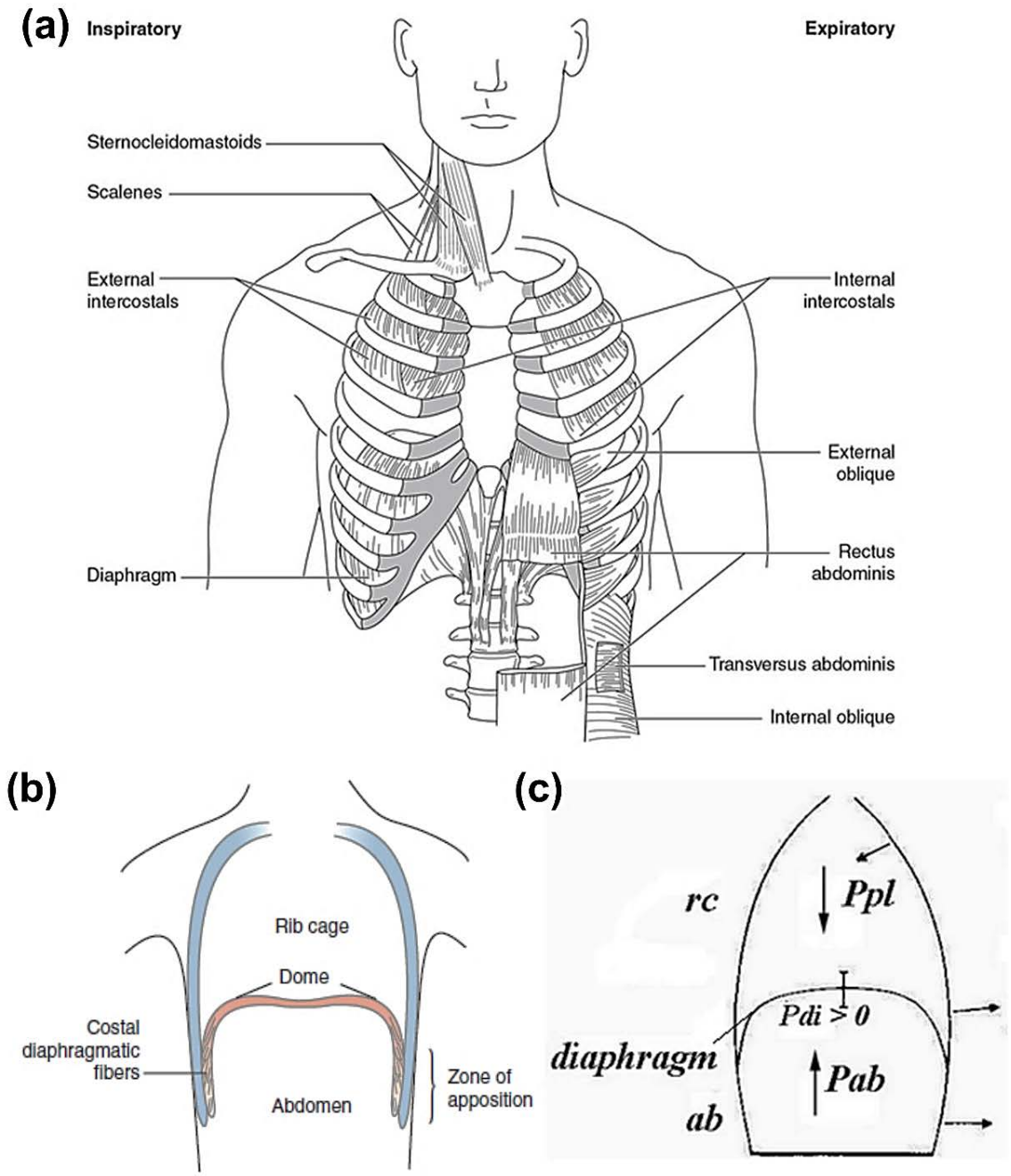

Figure 5.1. (a) Muscles of respiration. Image from Ref. [103]. (b) Chest wall, frontal section, at end-expiration. Costal diaphragmatic fibers are cranially oriented, resulting in apposition to the lower rib cage. Image from Ref. [101]. (c) Schematic of pressures applied to chest wall and its components, rib cage (*rc*) and abdomen (*ab*) during inflation. Image from Ref. [102].

5.2 EXPERIMENTAL SET-UP AND MEASUREMENT RESULTS

As discussed above, the intra-abdominal pressure (IAP) rises and falls throughout inspiration and expiration [104]. This IAP fluctuation during normal breathing is presumed to indicate the pressure moving the abdomen and thoracic wall [105], and the abdominal surface motion measurement is therefore used for continuous monitoring of respiratory function [106]. It has been found that the abdominal wall tension (AWT) reflects Intra-abdominal pressure, and that the epigastric region appears most suitable for AWT measurements [107, 108]. Therefore, the epigastric region is selected for distance and force measurement. The experimental set-up shown in Figure 5.2 consists of a braided elastic band (BEB), photoreflective sensor (PRS), linear actuator, and load cell. The actuator, load cell, and BEB are connected in series (in that order), with the PRS placed under the BEB.

The PRS measures the ratio of expansion and contraction of the BEB using changes in transmissivity of infrared light passing through the BEB when it is pulled and released by the linear actuator [109]. The load cell records the pull force at the same time. Figure 5.3 shows the recorded output signals from the PRS and the load cell. This set-up is used to characterize the BEB by obtaining a relationship between the PRS output voltage and pull force as well as the PRS output voltage and BEB displacement, which is the same as actuator displacement, i.e., ~2.5cm (Figure 5.4). The BEB is then worn around the abdomen with the PRS placed underneath, and the PRS output voltage is recorded during normal respiration (Figure 5.5). The abdomen displacement and pull force generated are then estimated using the relationships obtained from the BEB characterization tests. Figure 5.6 (a) and (b), show the box-plots of the predicted abdomen displacement and force, respectively. The maximum values of predicted displacement and force are 20.22 mm and 1.20 lbf, respectively, and median values are 15.38 mm and 0.97 lbf,

respectively. Figure 5.2(a) shows that the load cell is first connected to an amplifier, which is used to get measurable data from the strain gauge load cell. The output of the amplifier is then sent to the microcontroller. A digital-to-analog converter (DAC) is used to convert the digital signals from the amplifier to analog signals. The motor driver is programmed using a microcontroller to move back-and-forth by ~2.5cm. All analog signals are recorded using a data acquisition system (NI USB 6251).

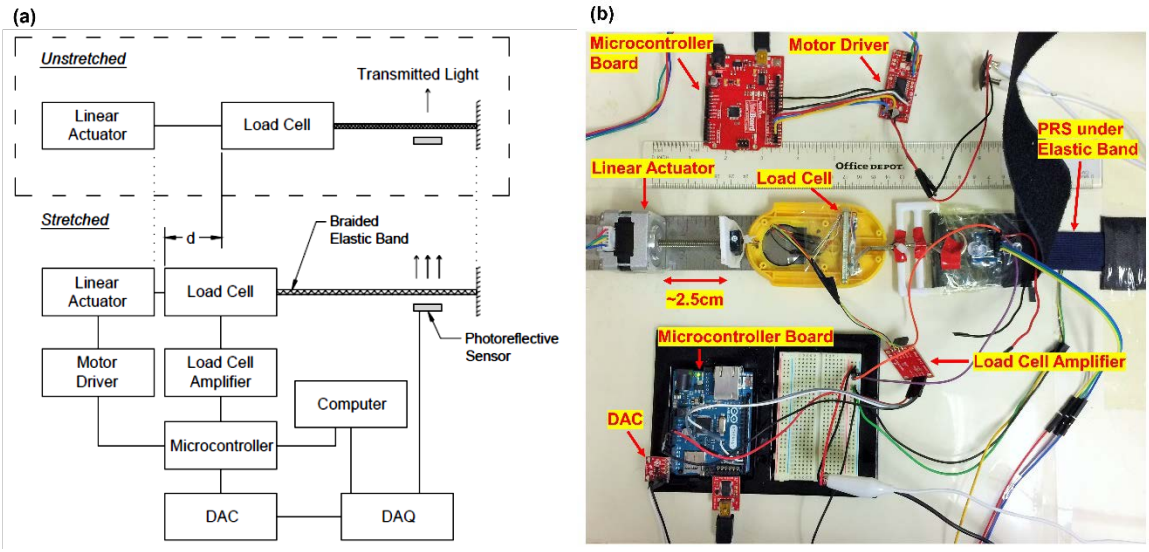

Figure 5.2. (a) Block schematic of the experimental set-up. Dashed box indicates the upstretched state of the braided elastic band, and the upward pointing arrows indicate transmitted light (increases in the stretched state). (b) Constructed experimental set-up. Note: *d* is ~2.5cm.

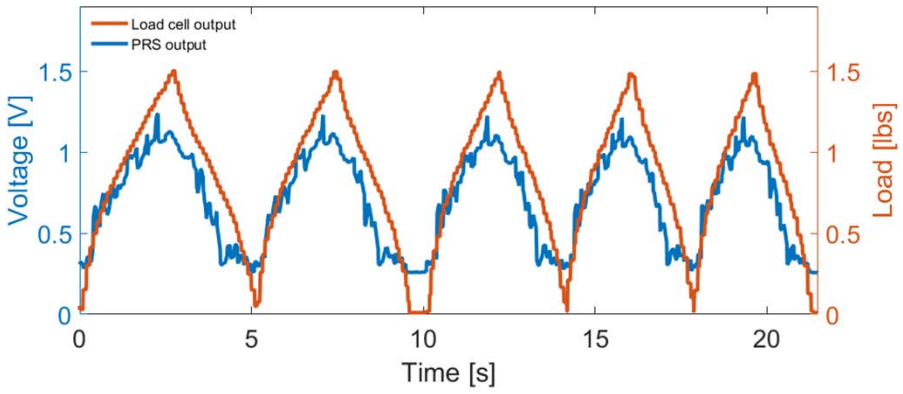

Figure 5.3. Recorded output signals from the photoreflective sensor (PRS) and the load cell.

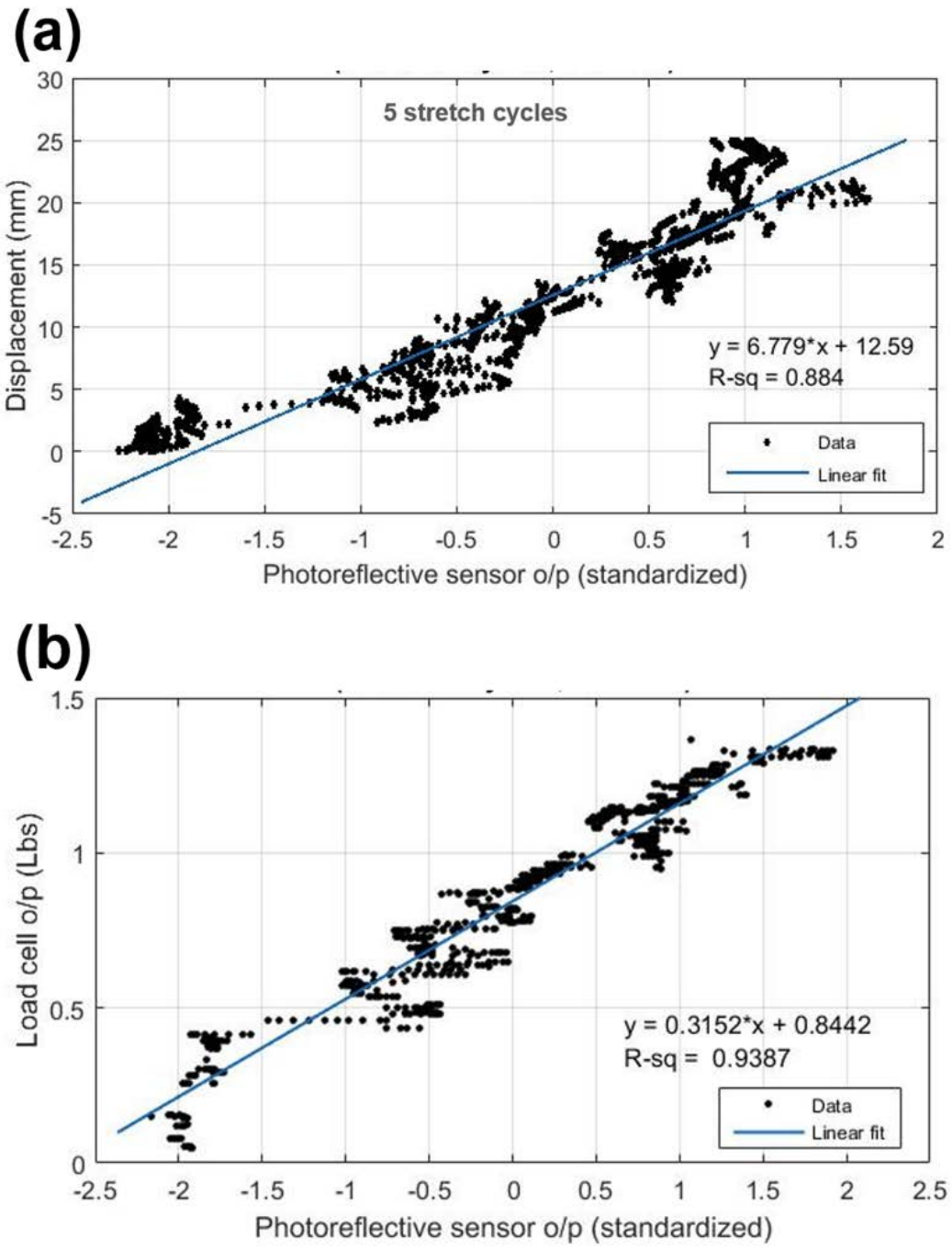

Figure 5.4. (a) Relationship between braided elastic band (BEB) displacement and photoreflective sensor (PRS) output voltage obtained from measurements over 5 stretch cycles [*y = 6.779x + 12.59, R-sq = 0.884*]. (b) Relationship between pull force and PRS output voltage obtained from measurements over 5 stretch cycles [*y = 0.3152x + 0.8442, R-sq = 0.9387*].

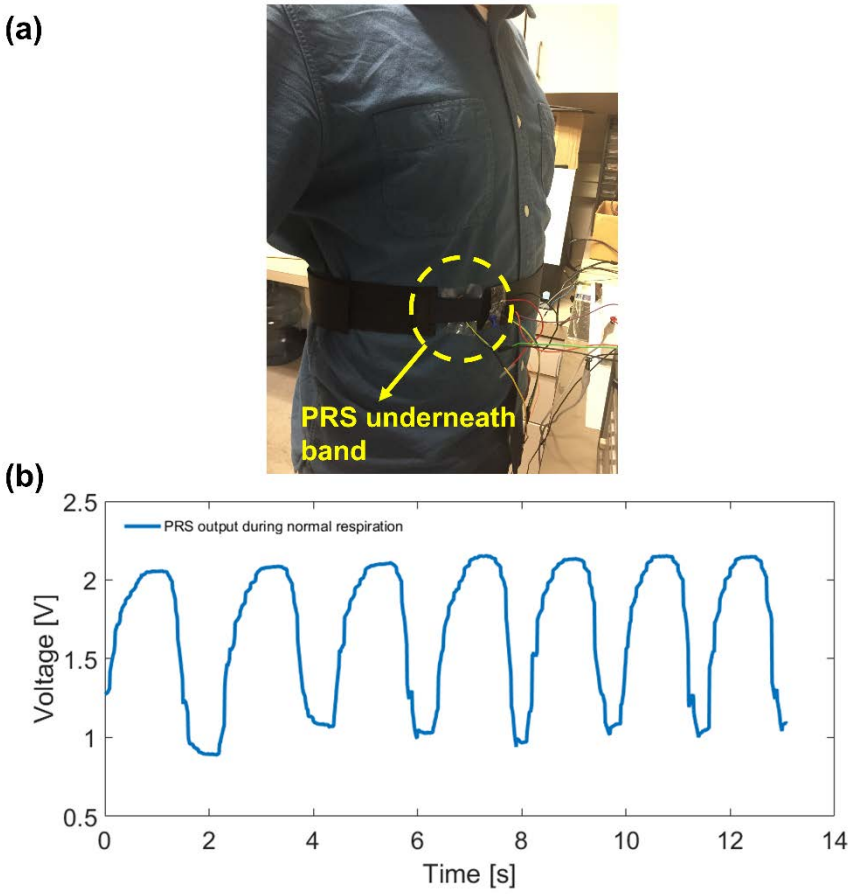

Figure 5.5. (a) The braided elastic band (BEB) worn around the abdomen with the photoreflective sensor (PRS) placed underneath. (b) PRS output signal recorded during normal respiration.

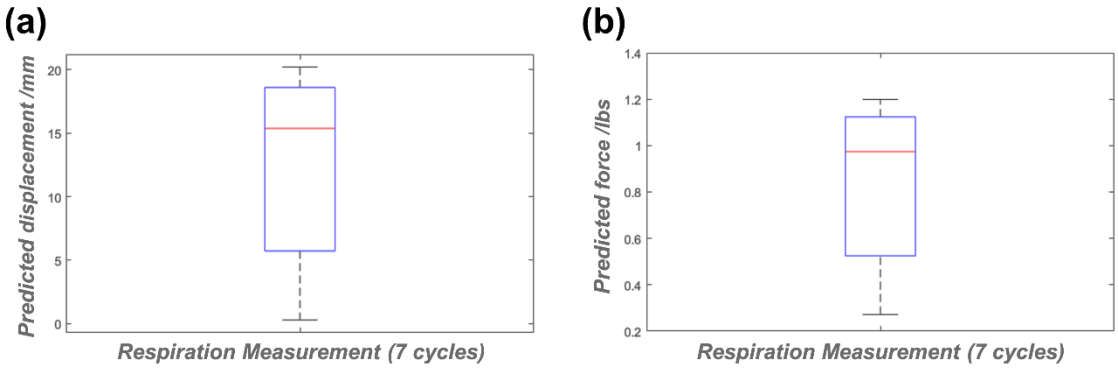

Figure 5.6. (a) Box-plot of predicted abdomen displacement during 7 cycles of normal respiration. (b) Box-plot of predicted abdominal force generated during 7 cycles of normal respiration.

5.3 SUMMARY

Direct measurement of abdominal force and displacement is performed by using a set-up consisting of a braided elastic band (BEB), photoreflective sensor (PRS), linear actuator, and load cell. The BEB is first characterized under stretch-release cycles triggered by a linear actuator by correlating its displacement and the pull force to the PRS output voltage. Post characterization, the BEB is worn around the abdomen along with the PRS underneath to predict its motion during respiration. The separation distance between the dielectric layers and the contact force in the benchtop test setup shown in Figure 4.5 are set to 15mm and 1 lbf (~0.45 kgf), respectively, based on the median abdominal displacement and force of 15.38 mm and 0.97 lbf, respectively, obtained herein. Further, this information also serves as an important design input requirement and is helpful in making design decisions.

6.0 WEARABLE RESPIRATORY ENERGY HARVESTER

6.1 INTRODUCTION

A TENG based on contact-separation mode is demonstrated as a wearable respiratory energy harvester (wREH), with its electric output performance characterized under normal respiratory motion. Figure 6.1 shows a graphic summary. The wREH is small (56mm x 63mm x 17mm), light-weight (20g), and can be comfortably worn around the abdomen just like a belt. A respiratory motion triggered lever mechanism is employed to operate the TENG in contact-separation mode. As the lever mechanism is triggered by abdomen motion during respiration, periodic contact and separation occurs between two different triboelectric material surfaces resulting in alternating flow of inductive electrons between the electrodes deposited on the non-contact side of these surfaces [56, 110]. To enhance the output performance of the wREH by increasing the effective contact area, a microdome-patterned PDMS film is used as one of the triboelectric material surfaces. PDMS has the advantages of flexibility, durability, transparency, non-toxicity, biocompatibility and cost-effectiveness, and has been used to enhance the output power of TENGs through micro/nano patterned surfaces [84, 111]. However, to create such patterned films, a master mold needs to be prepared using photolithography, which is a costly and complex manufacturing process. To overcome this limitation, a simple and cost-effective PLGA

patterning technique is demonstrated here. The fabricated wREH triggered under test conditions representing normal respiratory motion, delivers a peak open-circuit voltage (V_{oc}) of 16.8 V, surface charge density *(σ)* of 33.5 μCm^{-2} per cycle, and maximum area power density of 7.584 mWm^{-2} at an external load resistance of 4.6 MΩ. Rectified output of the wREH is used to charge commercial capacitors and light up a light emitting diode (LED). The wREH has also been shown to be utilized as a self-powered respiratory motion sensor capable of tracking rate and depth of respiration.

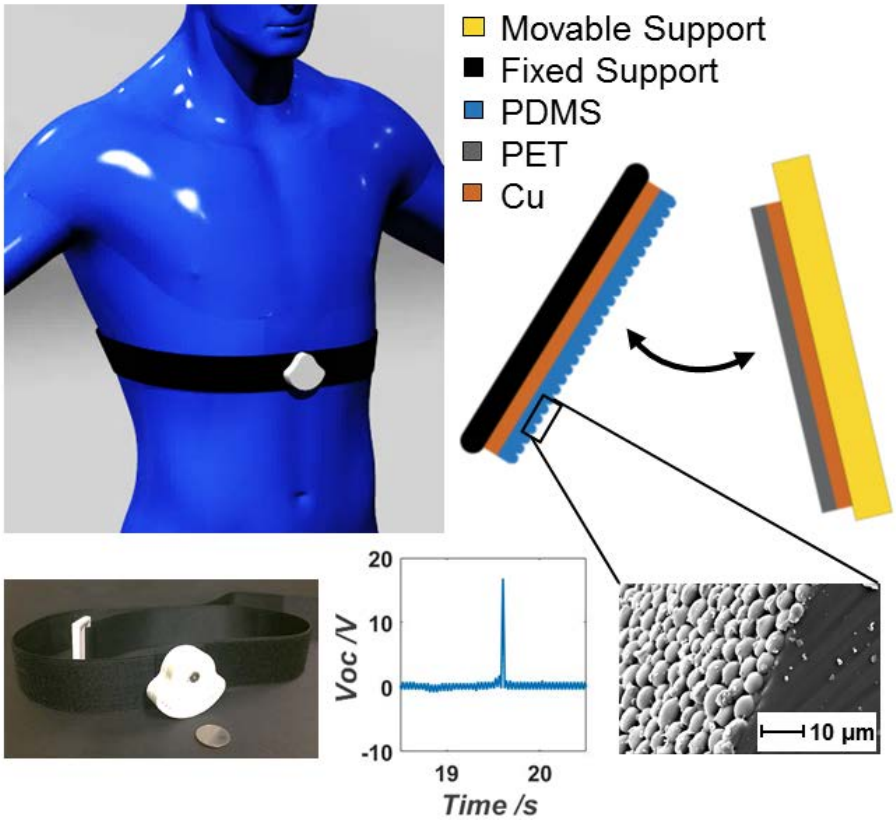

Figure 6.1. Triboelectric nanogenerator using microdome structures is presented as a wearable respiratory energy harvester and self-powered respiration sensor. The harvester is comfortably worn around the abdomen, and operates using a respiratory motion triggered mechanism. The regularly ordered micropatterns engineered using a simple and cost-effective poly lactic-co-glycolic acid patterning technique helps enhance the output performance by enhancing the triboelectric charge density.

6.2 DEVICE DESIGN AND FABRICATION

Several concepts were brainstormed, after which the lever mechanism concept described here was selected (refer Appendix A for details on different concepts generated). The CAD assembly model of wREH housing incorporating the TENG structure and different components of the lever mechanism is shown in Figure 6.2(a). It is well known that the charge generation process of a TENG is significantly affected by humidity and pressure [112, 113]. The housing can not only protect the TENG structure from unwanted mechanical impacts, but can also offer protection from changes in weather conditions. ABS (Acrylonitrile Butadiene Styrene) copolymer is selected to make the housing, lever arm, and fixed support, as it is a frequently used material in rapid prototyping of plastic objects [114]. The TENG structure consists of two dielectric components made up of a PET film (15mm x 25mm; 0.05mm thick) and a PDMS film (15mm x 25mm; 0.5mm thick) with microdome structures. Both films are deposited with a copper (Cu) electrode on their non-contact side. One film is attached to the movable support and the other to the fixed support. The movable support is fixed to one miniature ball bearing at the top and one at the bottom. The bearings in turn are fixed in the slots designed for them in the top and the bottom housing, thus creating a lever mechanism with the movable support as the lever arm. The lever arm is connected to a non-compliant belt such that when the belt is worn around the abdomen, the lever arm motion is synchronized with respiratory motion. This creates periodic contact and separation between the two dielectric films of the TENG which is necessary for generating an alternating signal. Figure 6.2(b) shows the fabricated device with the top housing open for observation. An elastic band (stretched to show the TENG structure in a separated state) is used as a return spring, which keeps the movable support in a compressed state such that the two dielectric films are in contact at the end of each exhalation cycle.

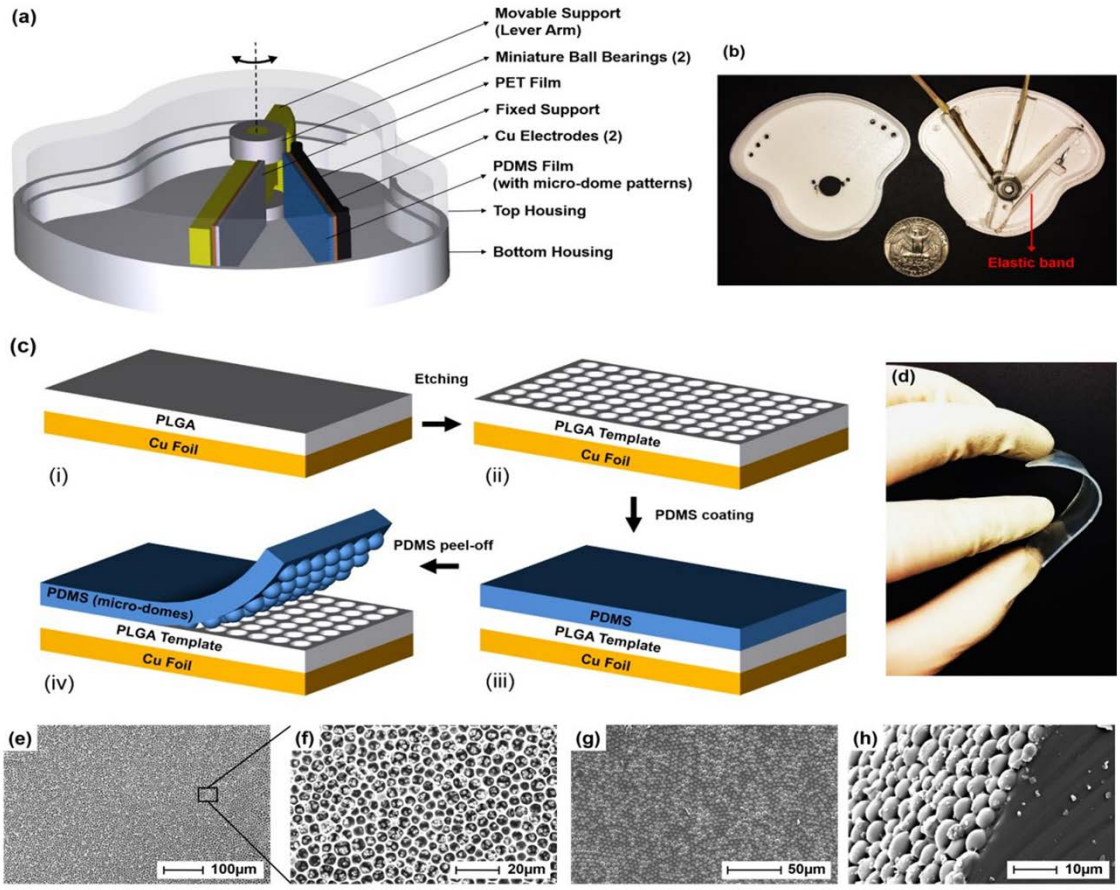

Figure 6.2. (a) CAD assembly model of wREH device components. (b) Fabricated prototype. (c) Schematic of fabrication process for PDMS film with microdome structures. (d) Fabricated PDMS film. (e) SEM image of PLGA template with microwells. (f) Magnified view of a section of (e). (g) SEM image of microdome patterned PDMS film. (h) Magnified side angle view of a section of (g).

Figure 6.3 illustrates different possible positions for a return spring and shows how an accordion-like TENG structure can be incorporated in the same housing to scale-up the output power by increasing the effective contact area and thereby the triboelectric surface charge. Here, a single element of such a structure is analyzed. There can be numerous such elements covering the entire abdominal area to achieve an enhanced power output. The triboelectric charge generation

in a TENG can also be enhanced by selecting appropriate charging materials and modifying surface morphology to further increase effective contact area [59, 115].

In that regard, presented here is a new method for fabricating a micro-patterned PDMS film based on a polylactic acid (PLA) patterning technique used in hybrid supercapacitors [116]. The schematic of the fabrication process is shown in Figure 6.2(c). A microwell patterned template (to be discussed further) is first created as a mold for making PDMS film with regularly ordered microdome structures, thus eliminating the need for using traditional photolithography technique to create a patterned silicon wafer mold [57]. Like PLA, a PLGA polymer thin film of appropriate thickness on Cu foil (Figure 6.2(c-i)) self-assembles into well-ordered arrays of microwell structures with dimensions of approximately 5μm after being etched in a chloroform and methanol mixture, thus forming a PLGA template (Figure 6.2(c-ii)). Thereafter, a PDMS mixture is coated onto the PLGA template, allowed to cure (Figure 6.2(c-iii)), and peeled-off carefully. The result is a PDMS film with regularly ordered microdome structures (Figure 6.2(c-iv)). The microwell structures are created because etching induces micro-phase separation of the PLGA film in the mixture. The capillary action during evaporation of chloroform causes the PLGA film to assemble into close-packed array on the foil. The consequent exchange of solvent and non-solvent is responsible for micro-phase separation in the polymer solution. The spongy cellular structure is created due to the liquid-liquid demixing by nucleation and growth of a polymer-poor phase. To obtain patterns with a constant spongy morphology, the phase separation process is stalled before completion. Figure 6.2(d) shows a flexible PDMS film made using this technique. Figure 6.2(e) and 6.1(f) are scanning electron microscopy (SEM) images of the PLGA template. Figure 6.2(g) and 6.1(h) are SEM images of microdome structures (dome size about 5μm) on the PDMS film. The described fabrication process involves a simple dipping process in a mixture of two fast

evaporating solvents without using any surfactants or stabilizing agents. This process is cost-effective, scalable, and can be performed under ambient conditions, thus offering an attractive alternative to the traditional photolithography technique.

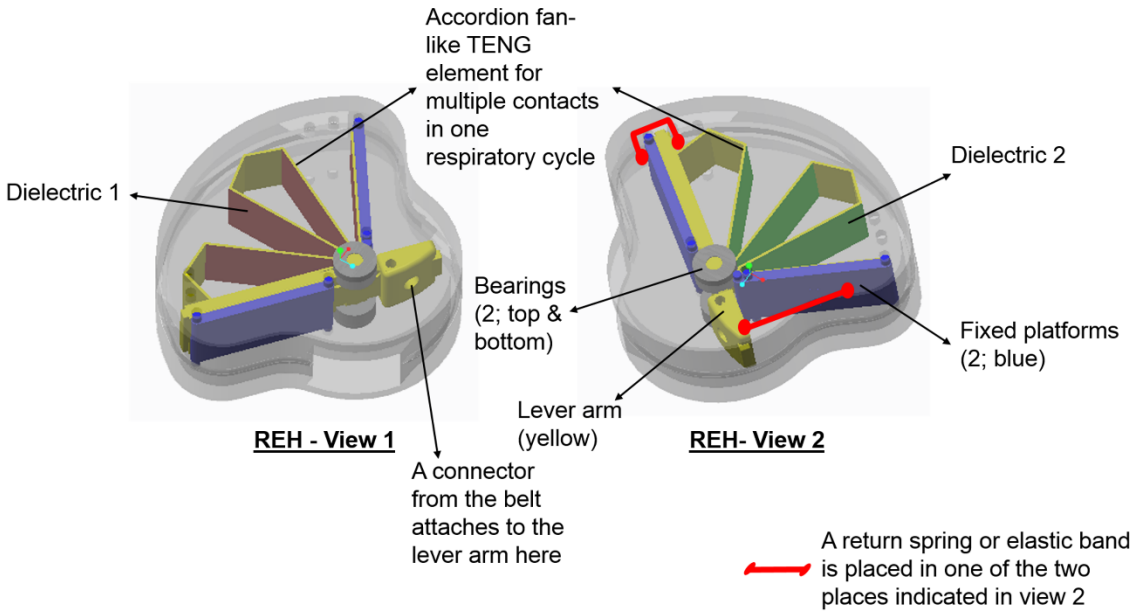

Figure 6.3. CAD assembly model of wREH incorporating an accordion-like TENG structure.

To compare the effect of different surface morphologies on TENG output, different PDMS films were fabricated using different templates – (a) PDMS film patterned using a 2500 grit abrasion pad as a template, (b) Bare PDMS film made using a plain glass slide as template, and (c) PDMS film patterned with an anodisc 200 nm aluminum oxide filter membrane. All fabricated films are of the same area size (15mm x 25mm) and thickness (0.5mm). Open-circuit voltages of TENGs made using all the films were recorded and compared. Results are presented and discussed in section 6.4.

6.2.1 Fabrication of PDMS films

Microdome patterned PDMS film is fabricated as follows:

A PLGA polymer (poly lactic-co-glycolic acid; 85:15) thin film on Cu foil is used to generate an ordered arrangement of microwell structures that is used as a template for making PDMS film with microdome structures. The PLGA polymer resin is first dissolved in chloroform (~3 wt. %) and then coated on Cu foil to a uniform thickness using a doctor blade. The Cu foil with the PLGA thin film is then immersed in a chloroform-methanol mixture (volume ratio of 17/3) for 2s and extracted, forming an array of ordered microwell patterns on its surface. Next, the PDMS elastomer mixture (Sylgard 184, Tow Corning) with a 10:1 ratio (w/w) of the base and the curing agent is stirred, coated on the PLGA template fabricated above, and degassed. The PDMS film with microdome structures is carefully peeled off after curing at room temperature. Any residue of PLGA is dissolved in acetone.

The 2500 grit abrasion disc patterned PDMS film, bare PDMS film, and anodisc filter membrane patterned PDMS film are fabricated as follows:

PDMS elastomer mixture (Sylgard 184, Tow Corning) with a 10:1 ratio (w/w) of the base and the curing agent is stirred, coated on templates: (a) silicon carbide (SiC) 2500 fine grit disc, (b) plain glass slide, and (c) Whatman® anodisc inorganic filter membrane (diam. 47 mm, pore size 200 nm), and then degassed. The PDMS films with 2500 grit patterns, no patterns, and 200nm filter membrane patterns are carefully peeled-off after curing at 100 ºC for ~0.5 h. The SiC disc is sputter coated with copper to make peeling-off PDMS easier. The filter membrane is carefully taped on one side to avoid any PDMS leaking onto the other side of the filter. Sodium hydroxide (NaOH) is used to dissolve any traces of filter on PDMS.

6.2.2 Device fabrication

The wREH consists of (a) a respiratory motion triggered lever mechanism, (b) a contact-separation mode based TENG, (c) an enclosure housing for (a) and (b), and (d) a non-compliant belt. To fabricate (a) and (c), a 3D assembly model is first created using a CAD software (Figure 6.2(a)). The supports and the housing are then 3D printed using ABS copolymer. Two flanged miniature (2mm x 5mm x 2.3mm) double shielded ball bearings are attached to the top and bottom of the lever arm of (a), which is then fixed into the slots designed for it in (c). To fabricate (b), a PET film (15mm x 25mm) with a 0.05mm thickness is deposited with Cu on one side by sputtering, sealed with an adhesive tape, and adhered to the lever arm of (b). Next, a microdome-patterned PDMS film (15mm x 25mm) of 0.5mm thickness is deposited with Cu on the non-patterned side by sputtering, sealed with an adhesive tape, and adhered to the fixed platform of (b). Before sealing, external wires are connected. Once assembled, the lever arm of (a) is attached to one end of the belt through a gap in the enclosure. The belt is made from non-compliant adjustable bands of Velcro® hook and loop fasteners that can easily tighten around the abdomen.

6.3 WORKING PRINCIPLE

The working principle of the energy conversion process in a TENG can be explained by the coupling between the triboelectric effect and electrostatic induction under periodic contact and separation of two material surfaces with distinct triboelectric characteristics [39]. Figure 6.4 illustrates the working of the TENG as a wREH in open-circuit condition. Figure 6.4(a) shows the initial state of the TENG outside the device housing, wherein the two dielectric films are separated

by a distance *d*. In this state, no charge transfer occurs and there is no electric potential difference between the two electrodes. After the TENG structure is assembled in the device housing, the two supports are compressed against each other due to the return spring as previously discussed. Surface charge transfer takes place in the contact area due to the triboelectric effect, resulting in equal and opposite charges on PET and PDMS films, per the triboelectric series [94, 117]. The charge transfers from a material on the positive side of the series to the one on the negative side. The further away the materials are, the greater the charge transferred. As the insulating property of these polymers allows for long-time charge retention [118], the surfaces charges with opposite signs coincide almost in the same plane, with no noticeable potential difference between the electrodes. This represents the initial state of the TENG in the device housing when there is no respiration (Figure 6.4(b)). Once the device is connected to a belt and worn, the onset of inhalation causes the movable support to rotate about the axis formed between the centers of the top and bottom bearings. This results in a separation θ' between the dielectric films. As the two films separate, the opposite charges also separate with an air gap, forming a dipole moment that induces a potential difference (V_{oc}) between the electrodes (Figure 6.4(c)). This is responsible for driving the flow of free electrons through an external load, when connected. As the inhalation cycle continues, V_{oc} also continues to increase until it reaches a maximum, corresponding to a maximum separation θ'' between the dielectric films at the end of inhalation (Figure 6.4(d)). Now, as the exhalation cycle begins (Figure 6.4(e)), V_{oc} starts decreasing with decreasing separation between the two dielectric films as the return spring works to bring the movable support back to its initial state (Figure 6.4(b)). Consequently, V_{oc} reaches zero value when the two dielectric films are in contact again. Figure 6.4(f) shows the V_{oc} signal of the generator for one respiration cycle.

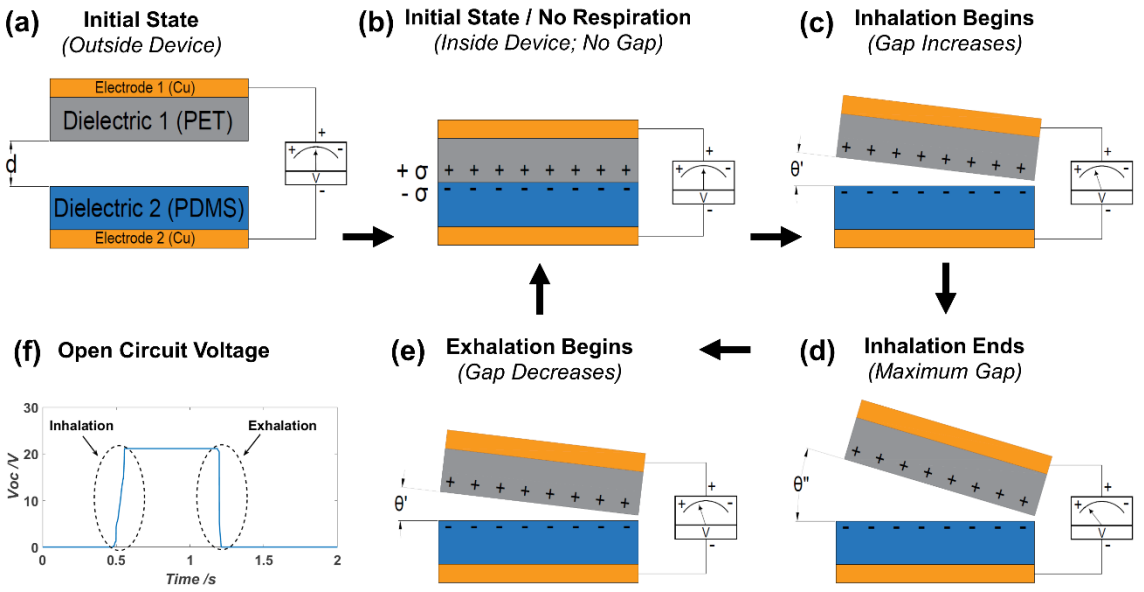

Figure 6.4. Working principle of the TENG as a wREH in open-circuit condition. (a) Initial state outside the device with a separation distance *d* between the two dielectric films, i.e., PDMS film with microdome structures (not shown to simplify illustration) and PET film. (b) Initial state after the TENG is assembled inside the device housing under a compressive force bringing the two dielectric films in contact with each other, generating equal and opposite triboelectric charge densities (σ) on the contact surfaces of the dielectric films. This is the position when there is no respiration taking place. (c) Beginning of inhalation causes a separation θ', which results in an induced potential difference between the two electrodes. (d) As inhalation continues, V_{oc} keeps increasing until it reaches a maximum value at the end of inhalation, corresponding to a maximum separation θ'' between the films. (e) Beginning of exhalation causes the separation to gradually reduce back to θ', and eventually back to the initial state (b), continually diminishing V_{oc} in the process. (f) Open-circuit voltage corresponding to one respiration cycle.

To further understand the working principle, finite element simulations using experimental parameters are conducted to calculate the electric potential distribution in the TENG for different separations between the dielectric films. The schematic of the finite element model is shown in Figure 6.5(a). This structure is surrounded by air, which is selected as the ground and represents the electric potential at infinity [63]. The PDMS and PET films are assigned an experimental σ of

-10 nCm^{-2} and + 10 nCm^{-2}, respectively. This value of σ is estimated based on equation, $V_{oc} = \sigma d/\varepsilon_0$ (reported in Ref. [56]), where ε_0 is the permittivity of free space, V_{oc} is 16.8 V, and d is 15mm. Using this estimate as a boundary condition results in realistic simulations of electric potential, as discussed in section 4.0 The electric potential difference between the electrodes is zero in case of full contact and rises with increasing separation, reaching 9.34 V for a separation of 60° (Figure 6.5(b-f)). These simulation results are consistent with the mechanism described previously.

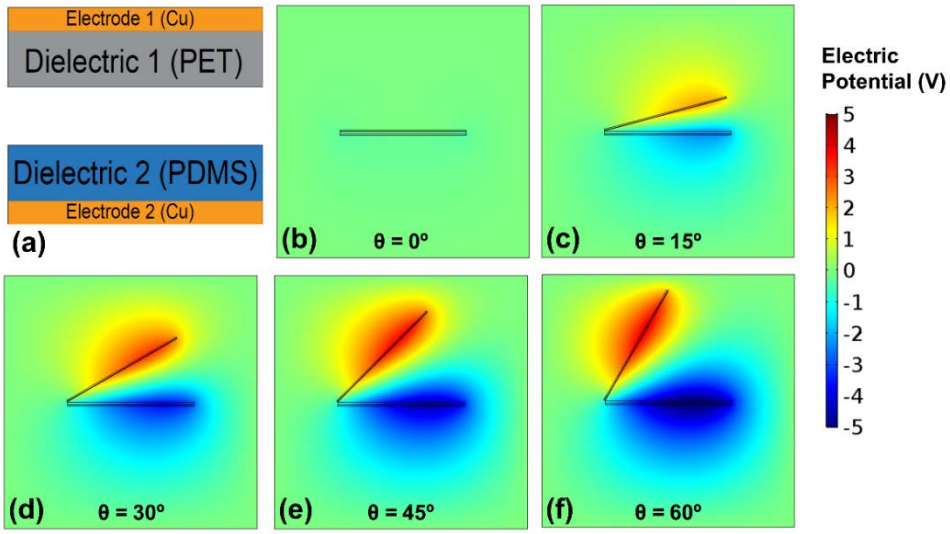

Figure 6.5. (a) Schematic of the finite element model. Finite element simulation of the potential distribution in the TENG for angular separations of (b) 0°, (c) 15°, (d) 30°, (e) 45°, and (f) 60° between the PDMS and PET films.

6.4 DEVICE CHARACTERIZATION

Systematic characterization of the TENG is conducted using a robust vertical contact-separation set-up shown in Figure 4.5. It is reasonable to use a vertical periodic motion to characterize the angular TENG structure presented here, because the working principle remains the same. To validate this, finite element simulations were performed for vertical separations corresponding to

the angular separations in Figure 6.5. Figure 6.6 shows that the trend as well as magnitude of electric potential distribution in the TENG is similar in both cases. For the test conditions to be in the range of normal respiratory motion, a contact-separation frequency of 0.33 Hz is selected [21, 119, 120]. In addition, measurements to determine abdomen displacement and force generated during normal respiration were performed (refer section 5.0). Consequently, the vertical separation distance of the test set-up is fixed at 15 mm with a contact force of ~0.45 kgf. Figure 6.7 shows the measured contact force using a force sensitive resistor.

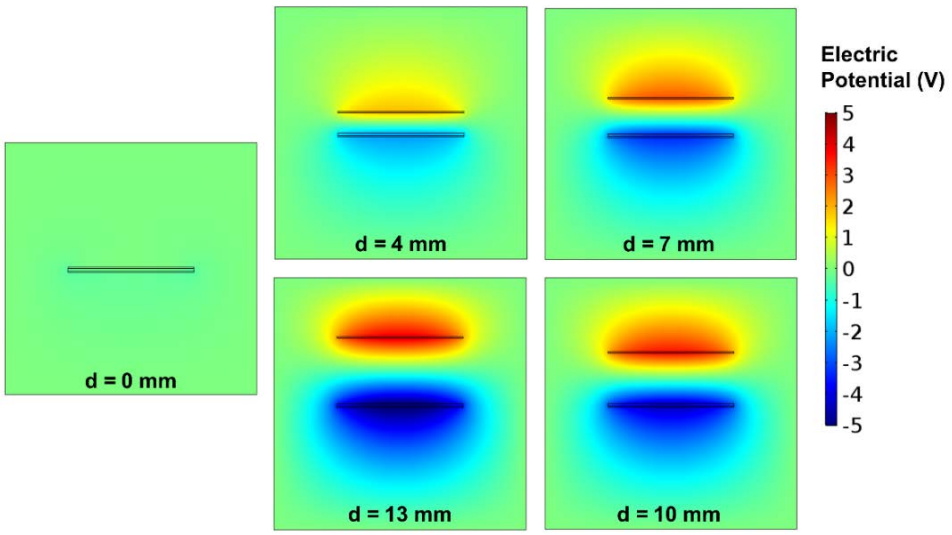

Figure 6.6. Finite element simulation of the potential distribution in the TENG for different vertical separations between the PDMS and PET films. Note: For an angular separation of 15º between the two dielectric films, the vertical separation between the midpoints of the films is measured to be 4mm using a CAD model. Thus, the simulation for 4mm vertical separation corresponds to the simulation for 15º angular separation. Similarly, the simulations for vertical separations of 0mm, 7mm, 10mm, and 13mm correspond to the simulations for angular separations of 0º, 30º, 45º, and 60º, respectively.

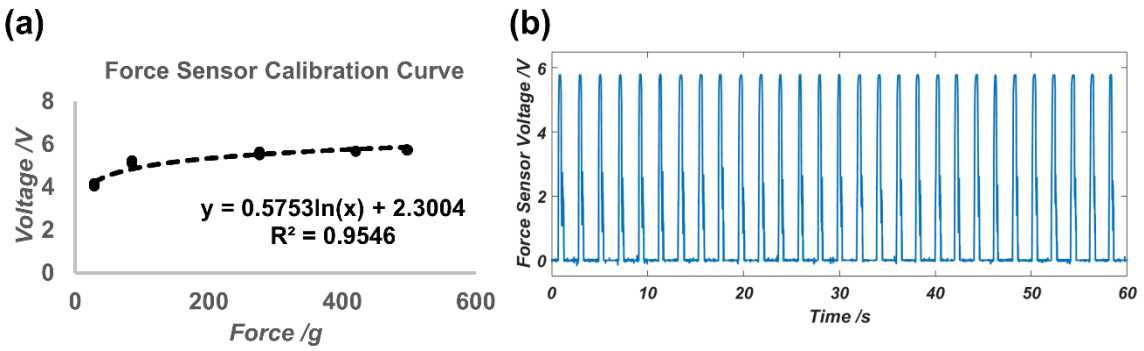

Figure 6.7. Measurement of contact force of the test set-up using a force sensor. (a) Force sensor calibration curve. (b) Output voltage of the force sensor after being attached to the test set-up.

The measured open-circuit voltage of the TENG is shown in Figure 6.8(a), where the magnitude of voltage peak reaches 16.8 V. For comparison with different surface morphologies, open-circuit voltages are obtained using: (a) PDMS film patterned with a 2500 grit abrasion disc, (b) non-patterned bare PDMS film; and (c) PDMS film patterned with an anodisc 200nm aluminum oxide filter membrane. Figure 6.9 compares the V_{oc} signals obtained from the aforementioned films. The peak V_{oc} obtained using microdome patterned PDMS is approximately 32, 8, and 4 times greater than that obtained using (a), (b), and (c), respectively. This suggests a consistently well-ordered microdome structure throughout the surface area of the film. The difference in V_{oc} signals can be explained by the fact that all engineered surfaces are rough to some extent and contact happens only at the apex of the surface asperities [121, 122]. With well-ordered micro/nano patterns, the surface roughness parameters related to height, depth, width, and spacing of the asperities can be controlled, thus ensuring a minimum contact area at the very instance of contact. This minimum area is therefore potentially greater than that in an apparently flat surface, as there are more points of contact.

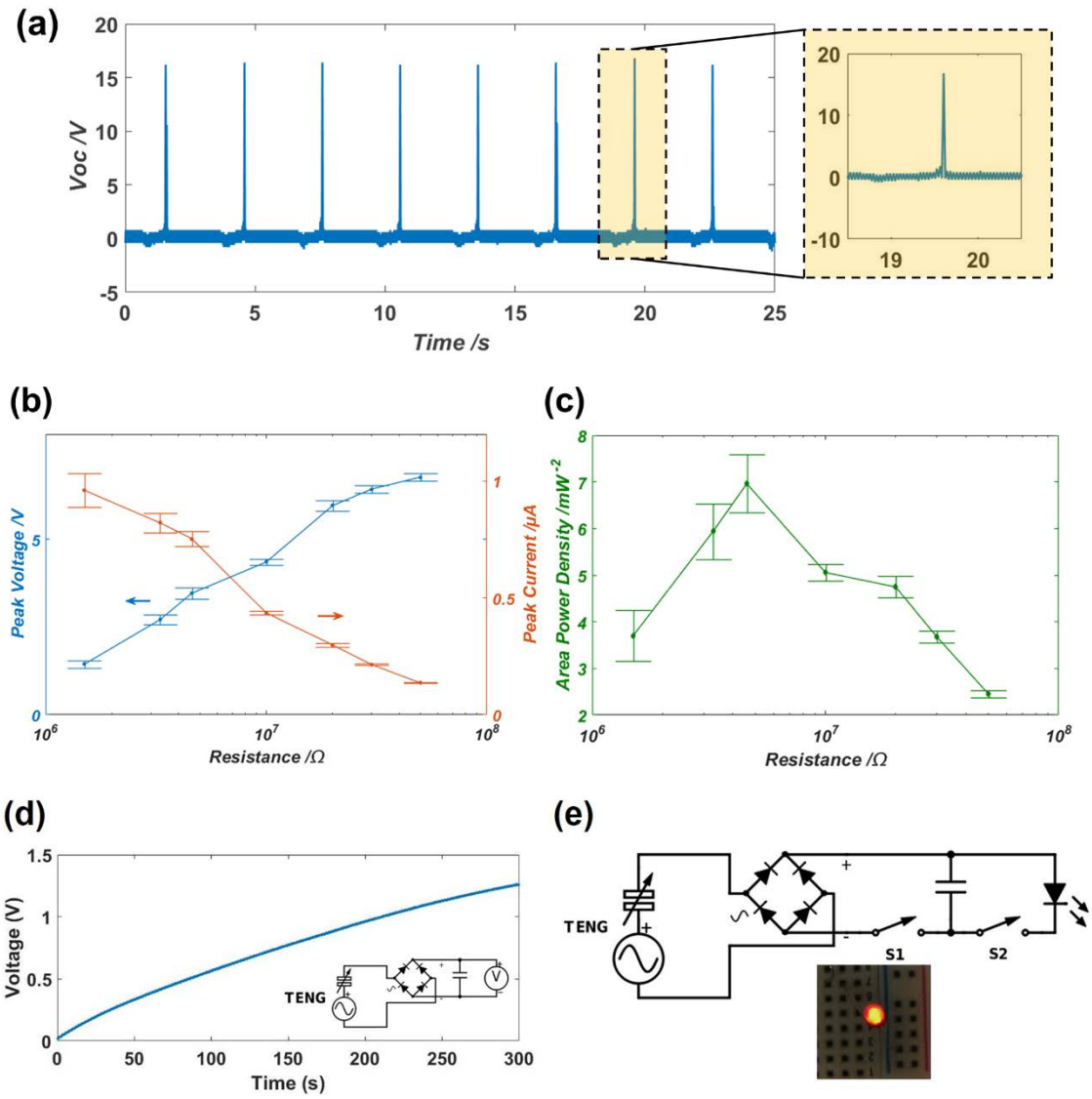

Figure 6.8. Performance characterization of the TENG under normal respiratory motion. (a) Measured open-circuit voltage (V_{oc}). Inset: enlarged view of the single highlighted cycle. (b) Output peak voltage, output peak current, and (c) output area power density dependence on external load resistance. Error bars represent standard deviation (SD) from the mean (n =7). (d) Measured voltage across a 1μF capacitor charged by the fabricated TENG. Inset: the equivalent circuit to store the harvested energy. (e) The equivalent circuit for lighting up a light emitting diode (LED) using the energy stored from the harvester. Inset: LED illuminated by a 100 μF capacitor.

Since the contact area increases with an increase in contact load, the use of PDMS with micropatterns is particularly important in the presented study as the contact force is low. The

elasticity of the microdome patterned PDMS allows for an increase in the effective contact area for a small increment in force, thereby increasing the interface roughness when in contact with the PET surface. In that light, sample (a) shows the effect of having micro-wells instead of micro-projections, which reduces the generator output via reducing the interface roughness as compared to that in (b). Sample (c) shows the effect of nanoprojections surrounded by nanocracks, which enhances the generator output via increasing the interface roughness as compared to that in (b). Microdome patterned PDMS giving an enhanced output as compared to that obtained from sample (c) could be because the nanocracks do not allow for sufficient deformation of the nanoprojections, which is necessary to increase the effective contact area. Figure 6.10 shows the SEM images of the surfaces of the abrasion disc, PDMS film made using the disc, and PDMS film made using the anodisc filter membrane. It must be noted that the peak shape of the voltage is due to the measurement being performed using an oscilloscope with a 10x probe, having an equivalent input impedance of 10MΩ.

To systematically study the reliance of output performance of the TENG on different external loads, different resistors were connected across the TENG. Figure 6.8(b) shows means and standard deviations (SD) of the output voltage and current peaks under different values of external load resistances. The measured peak voltage mean increased from 1.440 V *(n* = 7, *SD* = 0.108*)* to 6.777 V *(n* = 7, *SD* = 0.100*)* when the load resistance increased from 1.5 MΩ to 50 MΩ. The peak current mean showed an opposite trend, decreasing from 0.960 µA *(n* = 7, *SD* = 0.072*)* to 0.136 µA *(n* = 7, *SD* = 0.002*)* under the same external loads. Figure 6.8(c) shows the dependence of the corresponding instantaneous area power density ($P/A = V^2/RA$, with A being the effective area, i.e., 375mm^2) on different external load resistances. A maximum area power density of 7.584 mWm^{-2} is achieved at an external load resistance of 4.6 MΩ. This is the optimum external circuit

condition for energy conversion. Further, to demonstrate the impact of contact force and frequency on generator output, V_{oc} was recorded as the contact force increased from approximately 0.45 kgf to 0.51 kgf while the contact-separation frequency was varied from 0.33 Hz to 1.67 Hz (Figure 6.11). Fundamentally, the peak values of V_{oc} should be independent of external motion frequency [41, 45]. The observed linear increase in the magnitude of V_{oc} can therefore be mainly attributed to the increasing contact force, and to the possibility of some charges accumulating due to incomplete neutralization at higher frequencies, causing an increase in the triboelectric potential. This reiterates the challenge of harvesting at low frequency and low force.

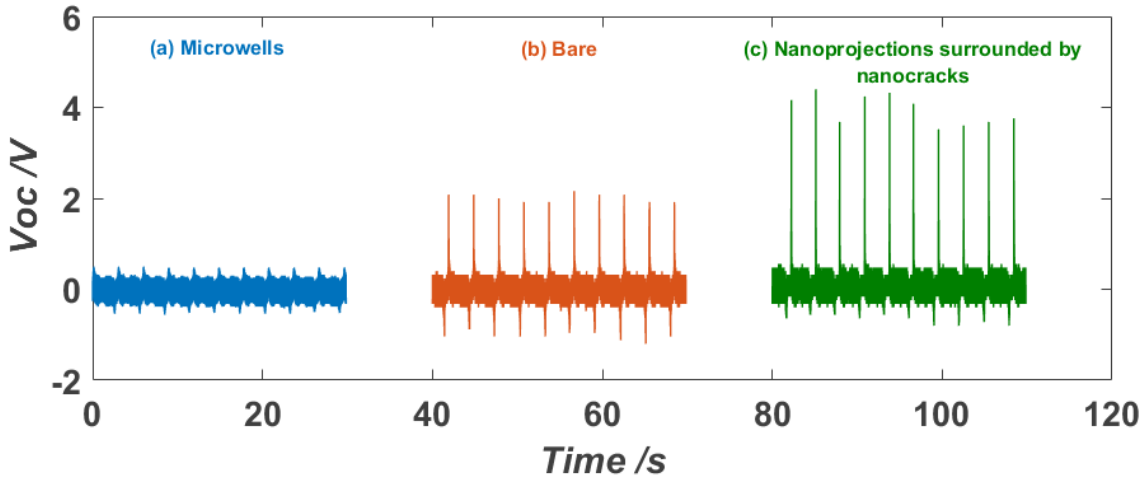

Figure 6.9. Open circuit voltage output of the TENG obtained using (a) 2500 grit abrasion disc patterned PDMS film, (b) non-patterned bare PDMS film, and (c) anodisc 200nm filter membrane patterned PDMS film.

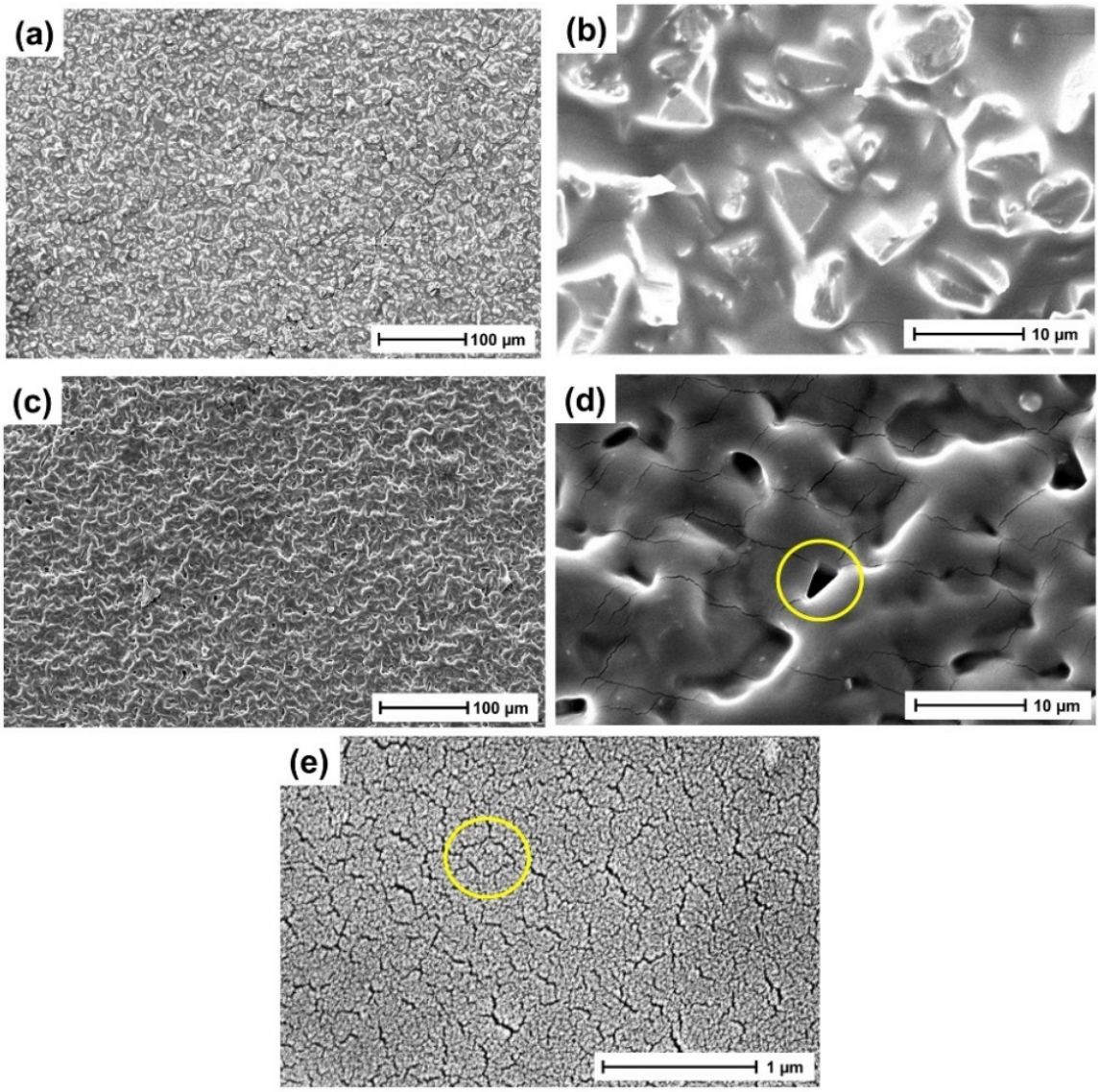

Figure 6.10. SEM images of (a) surface of silicon carbide (SiC) 2500 grit disc, (b) magnified view of a section of (a), (c) PDMS film made using (a) as template, (d) magnified view of a section of (c), and (e) PDMS film made using anodisc filter membrane as template. The circled portion in (d) highlights a single microwell (~3 µm in size) formed due to a dispersed SiC particle on the disc. The circled portion in (e) highlights a single nanoprojection surrounded by nanocracks formed due to 200nm pore structure of the filter membrane.

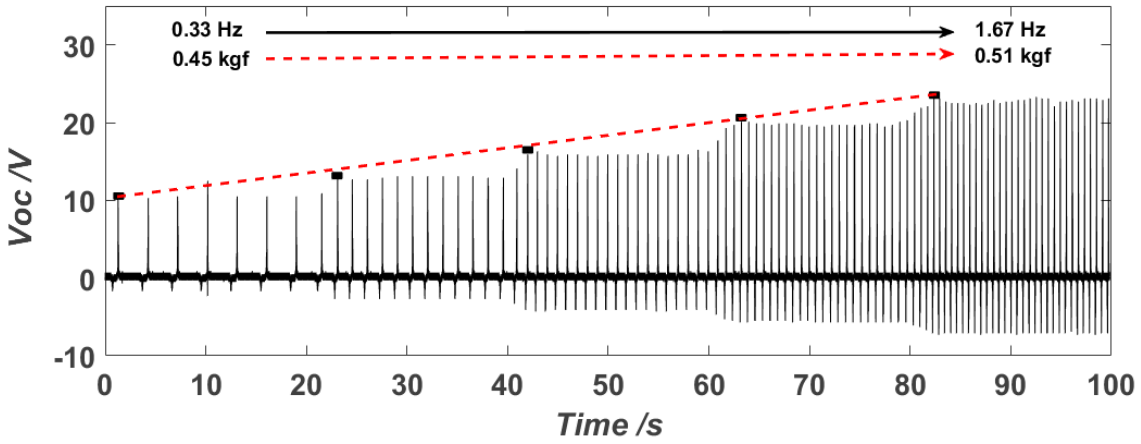

Figure 6.11. Dependence of the open-circuit output voltage of the TENG on force and frequency.

An energy storage unit such as a capacitor, supercapacitor, or battery is needed to store the energy from the AC pulses generated by the TENG to provide a constant bias voltage or current to power electronic devices [123]. To demonstrate this capability, a circuit integrating the TENG with a full-wave bridge rectifier and a 1 µF capacitor is constructed, and the voltage across the capacitor is monitored. Figure 6.8(d) shows that a 1 µF capacitor charged from 0.016 V to 1.261 V in 300 s, corresponding to an accumulated σ of 33.5 µCm^{-2} per cycle ($\sigma/cycle = C\Delta V/ATf$), where C is 1 µF, ΔV is 1.245 V, A is 375mm^2, T is 300 s, and f is 0.33Hz). Furthermore, a 100 µF capacitor is charged using the circuit shown in Figure 6.8(e), and the stored energy is used to light up an LED. Here, the capacitor is first continuously charged by the TENG (switch S1 on; switch S2 off). Once the capacitor is charged to a suitable voltage (> bias voltage of the LED), it is disconnected from the TENG (S1 off), and the stored energy from the capacitor is used to light up the LED (S2 on). In addition to reliably charging capacitors, a durability test (>1000 cycles) was also conducted to confirm mechanical stability of the microdome structures (Figure 6.12). These measurements demonstrate the feasibility of harvesting energy from respiratory motion using a contact-separation mode based TENG for use as a sustainable power source.

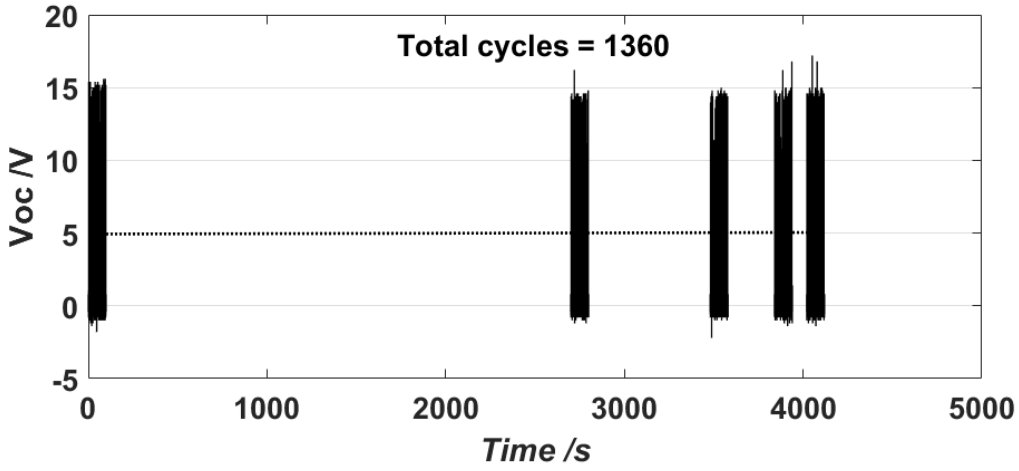

Figure 6.12. Durability test of the TENG using microdome-patterned PDMS under periodic contact force of ~0.45 kgf.

Lastly, a note on efficiency -- the efficiency (η) of the generator is estimated using the following formula:

$$\eta = \frac{Electrical\ \ Output\ \ Power\ (P_e)}{Mechanical\ \ Input\ \ Power\ (P_m)} \times 100\ \% \tag{6-1}$$

The mechanical input power is calculated as follows:

$$P_m = \frac{Work\ (W)}{time\ (t)} = \frac{Force \times disance}{t} = Force \times velocity \tag{6-2}$$
$$= 0.45Kgf \times 1.5cm \left(\frac{20\,breaths}{\min} \right) \left(\frac{\min}{60\,\sec} \right) = 22.1\,mW$$

As discussed previously, a maximum area power density of 7.584 mWm^{-2} is achieved by the wREH with the single TENG element. Therefore, P_e for this single element can be calculated as follows:

$$P_e = Area\ Power\ Density \times TENG\ element\ \ area \qquad (6\text{-}3)$$
$$= \frac{7.584mW}{m^2} \times 375mm^2 = 2.84\mu W$$

Substituting calculated values of P_m and P_e in equation (6-1), we get efficiency for a single element (η_1) as:

$$\eta_1 = 0.013\% \qquad (6\text{-}4)$$

The overall efficiency can be increased with number of elements, utilizing as much of the available abdominal surface area as possible. The mean waist circumference of an adult man in the United States is ~100cm [124], and the height of the abdomen is ~25cm [125]. From these dimensions, the total abdominal surface area ($A_{abdomen}$) available is approximated by considering the abdomen to be a cylinder of radius (r) and height (h), and calculating half the lateral surface area as follows:

$$A_{abdomen} \approx \pi rh \approx \pi \times \frac{100cm}{2\pi} \times 25cm \approx 1250\ cm^2 \qquad (6\text{-}5)$$

Assuming 50% of this surface area can be utilized to position several TENG elements, the total efficiency (η_t) can be calculated as follows:

$$\eta_t = \frac{\frac{7.584mW}{m^2} \times 625cm^2}{22.1mW} \times 100 = 2.145\% \qquad (6\text{-}6)$$

6.5 TESTING AS A RESPIRATORY MOTION SENSOR

The wREH is utilized as a self-powered respiratory motion sensor capable of tracking frequency as well as depth of respiration. The wREH is attached to a non-compliant belt and worn around the abdomen as shown in Figure 6.13(a). As previously discussed, due to the respiratory motion triggered lever mechanism, the separation between the two dielectric films of the TENG structure in the device housing corresponds to the abdomen motion during respiration. Changing separation induces a change in the output voltage between the two electrodes of the TENG, which can be used to monitor respiration. For instance, the time interval between signal peaks can be used to determine respiratory rate (Figure 6.13(b)), whereas the depth of respiration can be correlated to the peak amplitude (Figure 6.13(c)). Furthermore, the TENG voltage signal can be correlated to a spirogram to obtain vital information about lung volumes and capacities [126]. The chest wall is considered a structure with two compartments, the rib cage and the abdomen, with only one degree of freedom. So, any abdominal volume change must be equal and opposite to that of the rib cage, as both compartments undergo the same pressure and contribute different volumes. Volume change, which is a product of *airflow rate* and *time duration* [127, 128], is related to antero-posterior diameter changes. Therefore, a volume-motion relationship can be established and the abdomen motion can then be used to estimate lung volume changes [129-131]. Since the TENG voltage signal corresponds to the circumferential motion of the abdomen during respiration, it in turn represents the increase and decrease in abdominal volume. The area under the voltage-time curve of the TENG (based on a start point, a stop point, and a baseline) can thus be correlated to respiration volume parameters. For example, the area under part of the voltage signal obtained during the inhalation cycle of a spirometry test can be correlated to the *Inspiratory Reserve Volume* (IRV). Likewise, the area under part of the voltage signal obtained during the exhalation cycle of

a spirometry test will correspond to the *Expiratory Reserve Volume* (ERV). Since abnormal respiration is a marker of serious illness [132, 133], a potential application of such a self-powered biosensor can be in remote health monitoring. Abdomen/chest motion can reveal important information about respiration and may help to identify and manage patients at the risk of respiratory malfunctions and other serious adverse events.

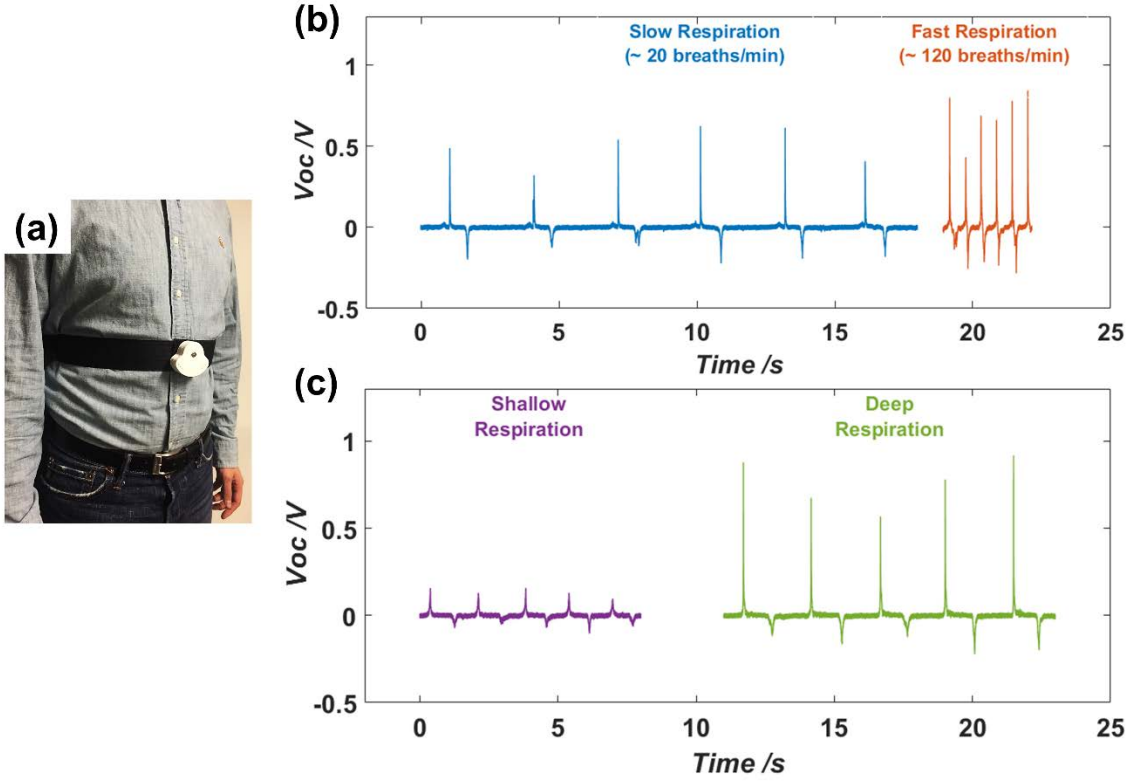

Figure 6.13. Application of the TENG as a respiratory motion sensor. (a) Fabricated wREH worn around the abdomen. (b) Voltage responses to slow and fast respiration. (c) Voltage responses to shallow (small abdomen motion) and deep (large abdomen motion) respiration.

It is worth noting that the ratio of positive voltage peak to negative voltage peak is higher in Figure 6.8(a) compared to that seen in Figure 6.13(b) and Figure 6.13(c), making the negative voltage peak in Figure 6.8(a) seem almost invisible. This asymmetry should be due to a lower

contact force and thereby a lower triboelectric charge density during the respiration test *(wherein the device prototype is worn around the abdomen)*, compared to that in the vertical contact-separation benchtop test setup used for Figure 4a. This is because the lever mechanism in the device amplifies separation between the contacting surfaces to incorporate the accordion-like TENG structure to increase the effective contact area, as previously discussed (Figure 6.3). Therefore, owing to a lower charge density in the device prototype when tested with a single element of the accordion-like structure, the positive voltage peaks in Figure 6.13(b) and Figure 6.13(c) are smaller than those in Figure 6.8(a), resulting in the said asymmetry.

6.6 SUMMARY

In summary, a wearable design of a contact-separation mode based TENG employing a respiratory motion triggered lever mechanism is presented. It has been demonstrated that this design can function as a respiratory energy harvester as well as a self-powered respiratory motion sensor. The TENG consists of a PET film and a microdome-patterned PDMS film as its two triboelectric layers. For each film, a Cu electrode is deposited on the non-contact surface. The PLGA patterning technique demonstrated here provides an attractive alternative for preparing PDMS films with micro/nano structures for TENGs. By converting the mechanical energy from respiratory motion, the TENG device can produce a peak open-circuit voltage of up to 16.8 V and a maximum area power density of 7.584 mWm^{-2} at an external load resistance of 4.6 MΩ. The PDMS film with microdome patterns enhanced the generator output by approximately 32, 8, and 4 times, compared to that obtained with PDMS films with microwells, bare surface, and surface with nanoprojections surrounded by nanocracks, respectively. As a respiratory motion sensor, the TENG device can not

only detect the respiratory rate, but also the depth of respiration. The TENG has been shown to charge a 1μF capacitor from 0.016 V to 1.261 V in 300 seconds, corresponding to an accumulated surface charge density of 33.5 μCm^{-2} in one respiration cycle. Furthermore, a 100μF capacitor is reliably charged and used to light-up an LED. This work demonstrates the possibility of using contact-separation mode based TENG to non-invasively harvest energy from respiratory motion, and thereby its potential towards practical applications as an effective power source for low power wearable electronics and integrated body sensor networks.

7.0 USING A SYNCHRONOUS SWITCH TO ENHANCE OUTPUT ENERGY OF TRIBOELECTRIC NANOGENERATORS

7.1 INTRODUCTION

Although TENGs have been demonstrated as a promising technology for mechanical energy harvesting [134], there are major challenges that need to be addressed for improving integration of TENGs with electronic systems for practical applications. TENGs are high impedance charge sources and usually have high output voltage but very low current. The inherent high impedance creates a huge mismatch when TENGs are directly integrated with energy storage devices such as batteries and capacitors, due to their low impedance, resulting in an inefficient energy conversion. This problem is generally solved *via* power management circuit designs [44, 45, 135]. Furthermore, as discussed in previous chapters, harvesting mechanical energy from irregular, low-frequency, and low-force motions is a great challenge. This is further emphasized in Table 7.1 which gives a summary of output performance of different triboelectric nanogenerators operating at low contact-separation frequency ($F_{cs} \leq 5$ Hz) and low contact force ($F \leq 5$ N). Keeping these challenges in mind, the switch based contact-mode TENG (SW-TENG) presented here offers a potential alternative or complementary approach.

Contact-mode TENGs generally operates as a floating source with its two electrodes connected to an arbitrary external circuit forming a closed loop. In the SW-TENG, a switch is placed between one electrode and the external circuit, electrically isolating the TENG from the

external circuit when open, and vice-versa, when closed (refer Figure 7.1(a) and (b)). Using an electromagnetic relay, the effect of different switching frequencies while keeping the contact-separation frequency (f_{cs}) and contact force constant at 1Hz and ~0.5kgf, respectively, is presented. The versatility of the approach is presented *via* demonstrating the switching effect in three TENGs fabricated with different types of polydimethylsiloxane (PDMS) based films – (a) bare, (b) microdome patterned, and (c) PDMS-Carbon nanofiber (CNF) composite. When the switching frequency (f_{sw}) is in sync with f_{cs}, the stored charges can be increased by a factor of 2.48, 2.25, and 1.92 in TENGs made with samples (a), (b), and (c), respectively, compared to that obtained under typical TENG operation. Figure 7.1 summarizes the difference between the structures of a typical TENG and a SW-TENG, and highlights the switching effect on stored voltages obtained using these two configurations. Further, a maximum area power density of 3.4Wcm^{-2}, 20Wcm^{-2}, and 31.7Wcm^{-2} is achieved at a resistance of 56Ω, in SW-TENGs made with samples (a), (b), and (c), respectively. Compared with the typical TENG, the optimal load resistance is decreased by six orders of magnitude, from megaohms to ohms.

Feasibility of SW-TENG for practical applications is demonstrated by using rectified output of the SW-TENG under synchronous switching to charge commercial capacitors and light up three light emitting diodes. In addition, a mechanical switch prototype is constructed and tested, confirming the practicality of the approach, thus providing a new approach for mechanical energy harvesting and opening the possibility of new designs and applications of TENGs across all its operating modes. A potential application for the SW-TENGs presented here can be as a self-powered sensor for monitoring electromagnetic relays that are a key component in automatic control system, telemetering system and communication system, and are widely used in the industries of electrical, aerospace, and mechanical, etc. [136-139].

Table 7.1. Summary of output performance of different triboelectric nanogenerators operating at low contact-separation frequency ($F_{cs} \leq 5$ Hz) and low contact force ($F \leq 5$ N)

f_{cs} [Hz]	F [N]	TENG device size [cm^2]	Area Power Density [$\mu W cm^{-2}$]	Reference
0.25	2.94	5	0.0286 *	Ko, Y. H., et al. (2014)[115]
0.5	5	15	1.69	Li, W., et al. (2014)[140]
0.5	2.94	1	3.996	Ko, Y. H., et al. (2014)[84]
4.41	0.5	63.5	15	Zi, Y., et al. (2015)[141]
4 **	3	12	10	Zhu, Y., et al. (2016)[34]

* Instantaneous area power density estimated from Figure 5a; ** Estimated from Figure 1

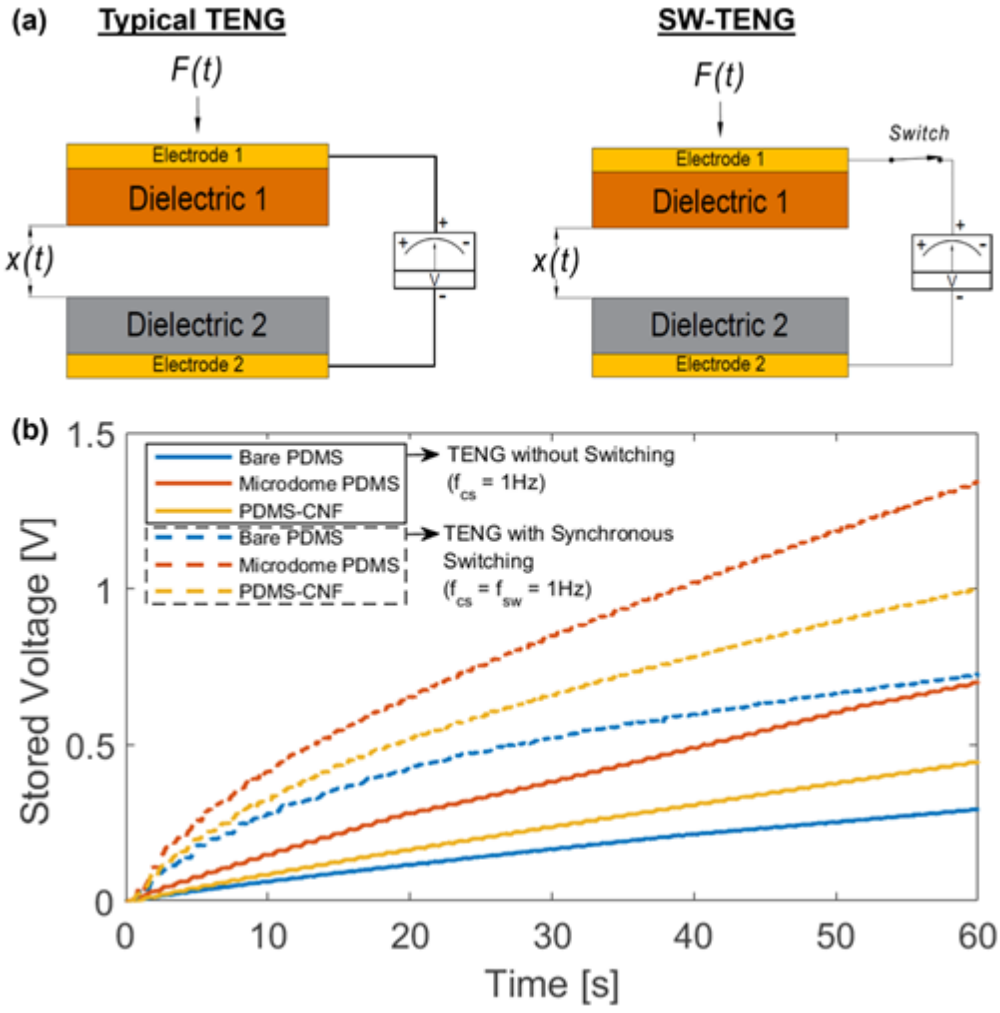

Figure 7.1. (a) Structures of a typical TENG and a SW-TENG. (b) Highlighting the switching effect by comparing the stored voltages obtained using the two configurations.

7.2 SW-TENG STRUCTURE AND WORKING

Figure 7.2(a) shows the basic structure diagram of the SW-TENG in initial state, wherein a switch is placed in between electrode 1 and the voltmeter. Figure 7.2 (b-d) illustrates the working for synchronous switching ($f_{sw} = f_{cs}$) in open-circuit condition. In the initial state, the switch is closed, and with no external force applied to the structure ($F(t) = 0$), the two dielectric films are separated by a distance, $x(t) = x_{max}$ (10mm in the experiments presented in this paper). In this state, no charge transfer occurs and there is no electric potential difference between the two electrodes. Once an external force is applied, the two dielectric films are brought into contact and the switch opens at this instance. Surface charge transfer occurs in the contact area due to triboelectrification (Figure 7.2(b)). This results in equal and opposite charges on the contact surfaces of dielectric 1 and dielectric 2, depending on their position in the triboelectric series [94, 117]. The material on the negative side of the series accepts charges from the material on the positive side, and the charge transfer increases as the gap between the selected material pair in the series increases, i.e., the higher the charge affinity difference between the materials, the higher is the amount of charge transferred. Since the decay of tribocharges can be neglected for insulating polymers [118], the confined surface charges with opposite signs coincide in almost the same plane, leading to no potential difference (V) being developed between the electrodes.

Once the force releases (Figure 7.2(c)), the separation distance between the dielectric films starts increasing gradually, thus separating the opposite tribocharges with an air-gap which induces a V between the electrodes under open-circuit condition. This potential difference is not seen by the voltmeter, since the open switch electrically isolates the TENG from the measurement equipment, which allows for a maximum potential difference (V_{max}) build-up between the electrodes, as any charge leak through the measurement equipment is prevented (a practical

voltmeter will not have an ideal input resistance of infinity). Now, as the structure reaches the released state (Figure 7.2(d)), the switch closes at the instance of maximum separation between the dielectric films ($x(t) = x_{max}$), resulting in V_{max} appearing across the voltmeter. As the external force is reapplied (Fig. 1(e)), V starts diminishing from V_{max} to zero as the separation distance between the dielectric films keeps reducing, eventually reaching zero on full contact (Figure 7.2(b)). This marks the end of one complete energy conversion cycle.

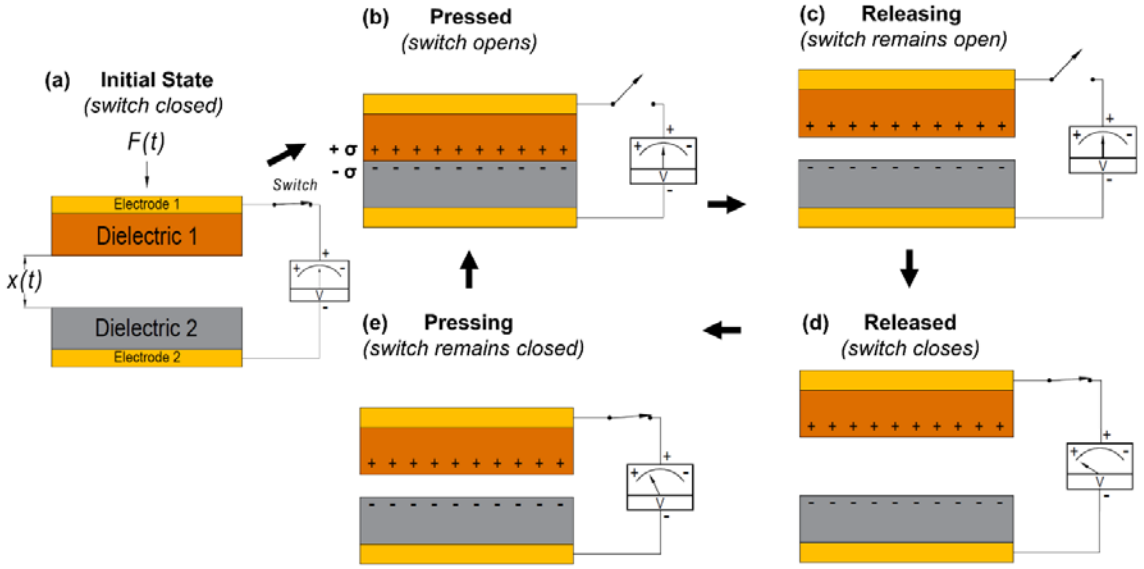

Figure 7.2. Structure and working of the SW-TENG for synchronous switching ($f_{sw} = f_{cs}$) in open-circuit condition.

Here, a PET film (0.05mm thick; 15mm x 25mm) is used as dielectric 1, and for dielectric 2, three different types of polydimethylsiloxane (PDMS) based films are used – (a) bare PDMS film, (b) microdome patterned PDMS film, and (c) PDMS-CNF composite film. All PDMS based films are 0.5mm thick and have an area of 15mm x 25mm. Sputtered gold (Au) is used as the electrode material. The use of these different film types enables the assessment of the effect of surface morphology and dielectricity. Micropatterns on the contact surface of PDMS increases the

interface roughness compared [142], whereas adding CNFs in PDMS increases the effective dielectric constant [143], compared to bare PDMS. Figure 7.3 shows the scanning electron microscopy (SEM) images of the microwell poly lactic-co-glycolic acid (PLGA) template, microdome patterned PDMS film, CNFs, and the PDMS-CNF composite film. The PLGA template (Figure 7.3(a)) is used as a mold to make the microdome patterned PDMS film with dome size of about 5 µm (Figure 7.3(b)). The CNFs having a diameter of about 200 nm are well dispersed in PDMS ((Figure 7.3(c) and (d)). Fabrication details are provided in the Methods section.

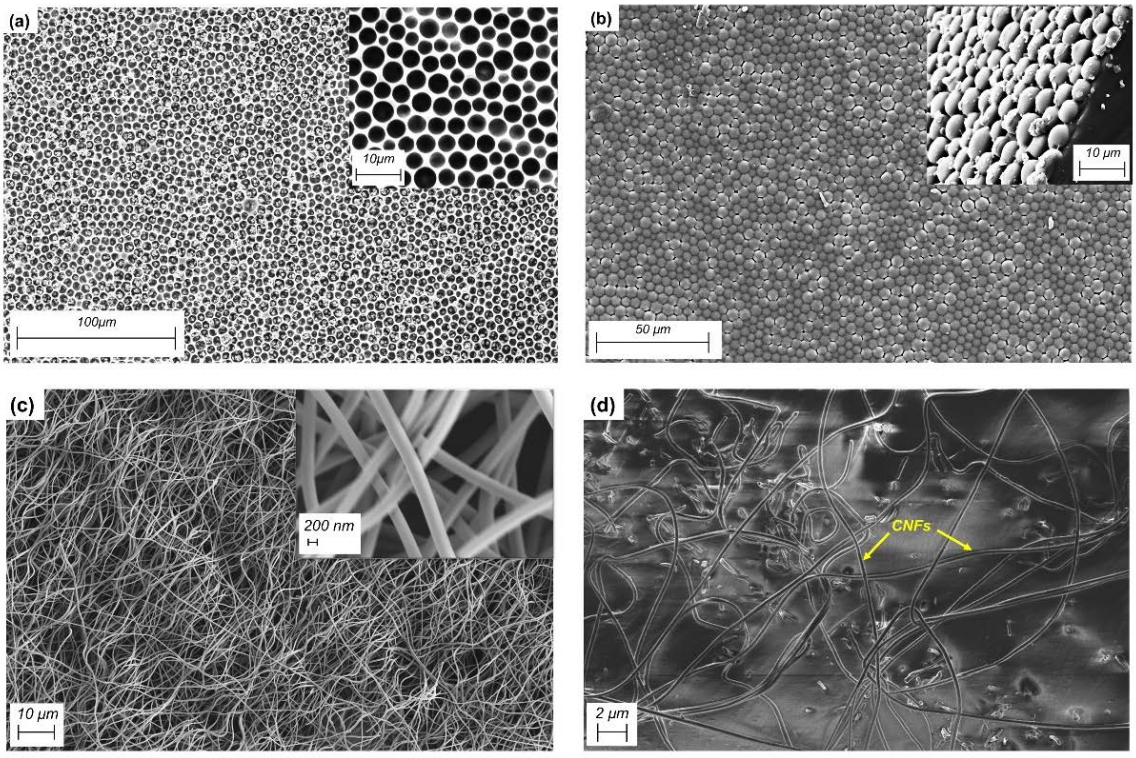

Figure 7.3. SEM images of (a) microwell PLGA template; inset: magnified view, (b) microdome patterned PDMS film; inset: magnified side angle view, (c) Carbon nanofibers (CNFs); inset: magnified view, and (d) PDMS-CNF composite film.

7.3 THE SWITCHING EFFECT

7.3.1 Increase in open-circuit voltage and stored charge

The working if the SW-TENG is experimentally demonstrated by connecting an electromagnetic relay between electrode 1 and the voltage measurement equipment. In addition to the synchronous case, the effect of switching frequencies higher and lower than a fixed contact-separation frequency of 1 Hz is explored by controlling the electromagnetic relay using a photoreflective sensor (PRS) and a microcontroller. Specifically, switching frequencies of 0.33Hz, 0.67Hz, 1.33Hz, 1.67Hz, and 2Hz are tested. The switching strategy is shown in Figure 7.4, which illustrates that the relay switch starts operating at the defined frequency by opening at the instance of first contact between the dielectric films. Details of the test set-up are discussed more in section 7.5. Figure 7.5 shows the voltage outputs of three different TENGs operating at different switching frequencies. The three TENGs are made using a PET film as its first dielectric material, and a bare PDMS film, microdome patterned PDMS film, and PDMS-CNF composite film as its second dielectric material, as previously discussed. It is found that the output voltage significantly increases across all switching frequencies for all TENGs, compared to that obtained in the typical TENG operation. Consistent values of voltage peaks are observed in the synchronous switching case ($f_{sw} = f_{cs}$), wherein the voltage has been observed to increase approximately by a factor of up to 22 (66 V compared to 2.88 V), 17 (156 V compared to 8.8 V), and 90 (178 V compared to 1.96 V) for the bare PDMS, microdome PDMS, and PDMS-CNF based TENGs, respectively.

To assess the output enhancing capability of the SW-TENG, a 1μf capacitor is charged using all three TENGs, with and without switching. A circuit integrating the TENG with a full-wave bridge rectifier and a 1 μF capacitor is constructed, and the voltage across the capacitor is

recorded. Figure 7.6 shows the stored voltage curves for all six cases. Stored charge (Q_c) per cycle is calculated for each case using the following equation:

$$Q_c = \frac{C\Delta V}{Tf_{cs}} \tag{7-1}$$

where C is the capacitance, ΔV is the total stored voltage, T is the total charging time, and f_{cs} is the contact separation frequency.

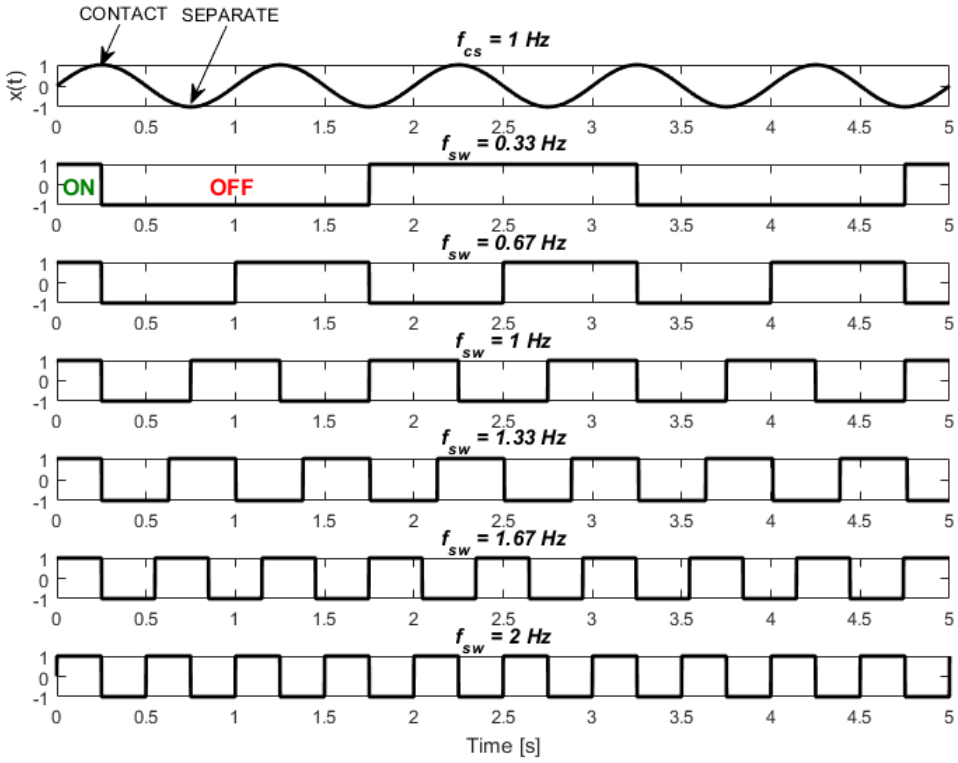

Figure 7.4. Switching strategy for measuring the output voltage of SW-TENG at different frequencies. The sinusoidal wave represents the contact-separation motion, and the square waves represent the ON and OFF states of the switch at switching frequencies of 0.33 Hz, 0.67 Hz, 1 Hz, 1.33 Hz, 1.67 Hz, and 2 Hz. Note that for all switching frequencies, the relay switch is initially closed (ON), and opens (OFF) at the first instance of contact. Note: The duty cycle for every switching frequency is 50%.

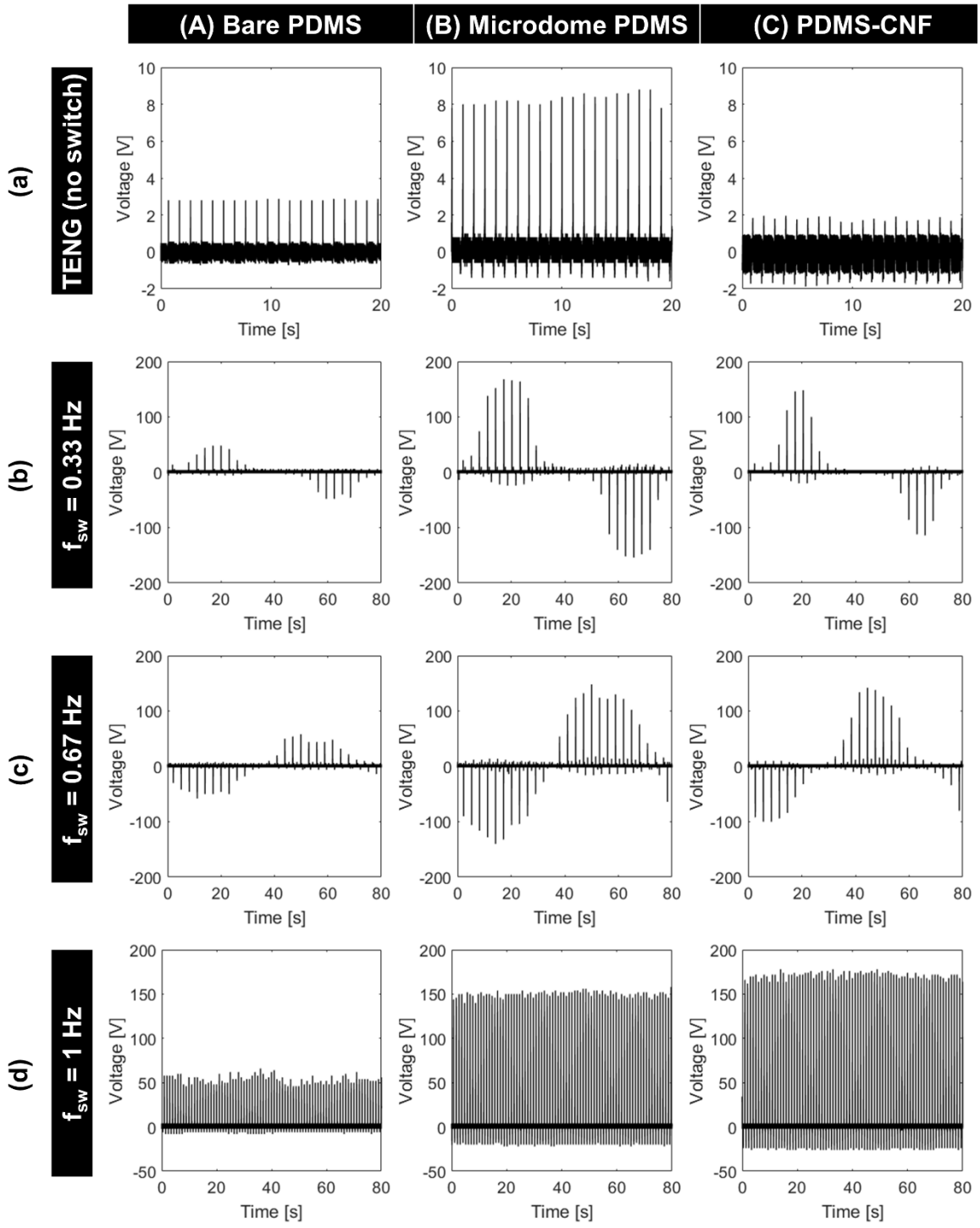
(A) Bare PDMS
(B) Microdome PDMS
(C) PDMS-CNF
(a) TENG (no switch)
(b) f_{sw} = 0.33 Hz
(c) f_{sw} = 0.67 Hz
(d) f_{sw} = 1 Hz
Voltage [V]
Time [s]

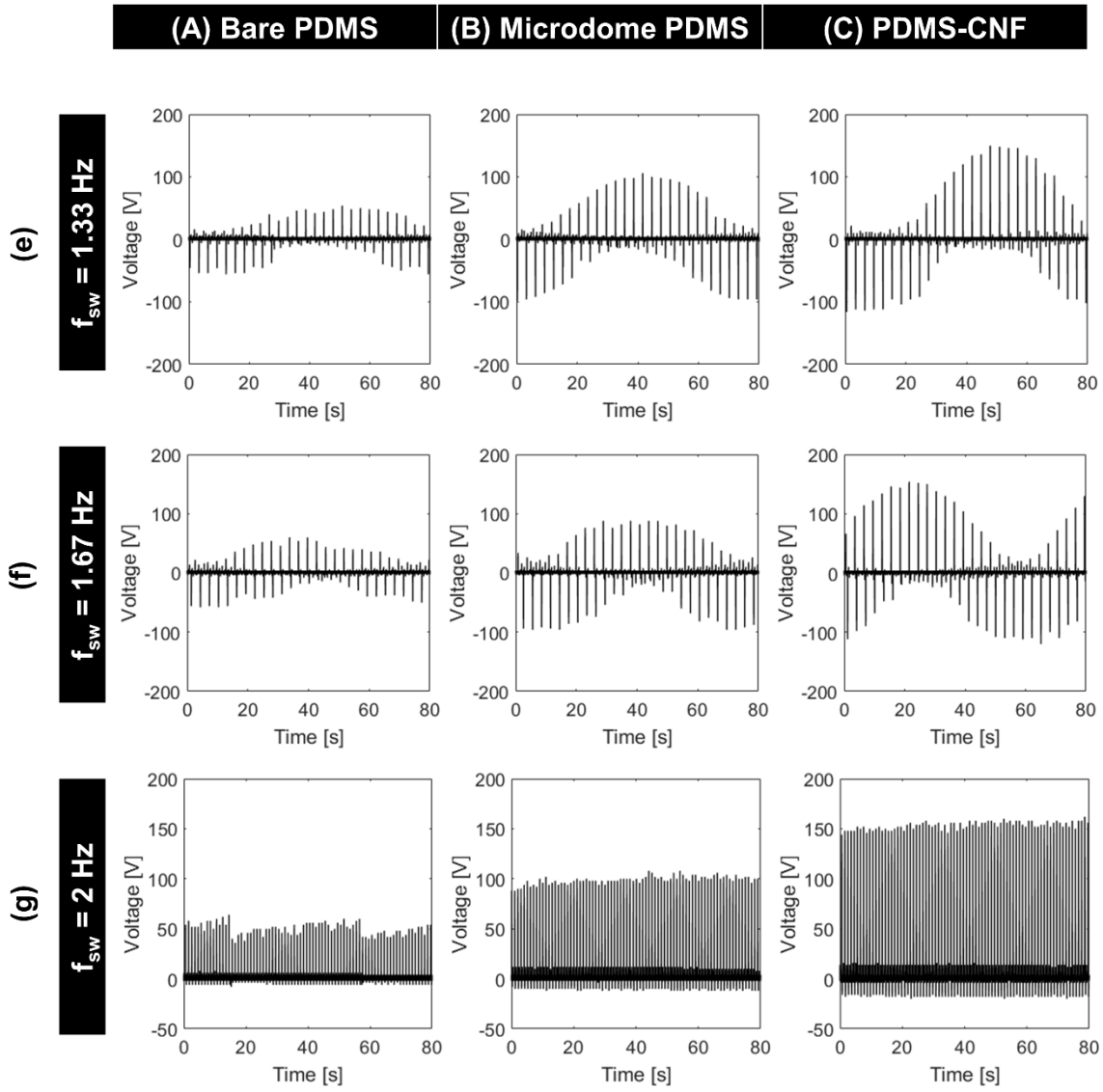

Figure 7.5. Effect of different switching frequencies on voltage outputs of three different TENGs. The columns represent outputs from TENGs made using (A) bare PDMS film, (B) microdome patterned PDMS film, and (C) PDMS-CNF composite film. Rows represent outputs under (a) typical TENG operation (no switch), (b) f_{sw} = 0.33 Hz, (c) f_{sw} = 0.67 Hz, (d) f_{sw} = 1 Hz (synchronous case), (e) f_{sw} = 1.33 Hz, (f) f_{sw} = 1.67 Hz, and (g) f_{sw} = 2 Hz. Note: In all cases, f_{cs} = 1 Hz.

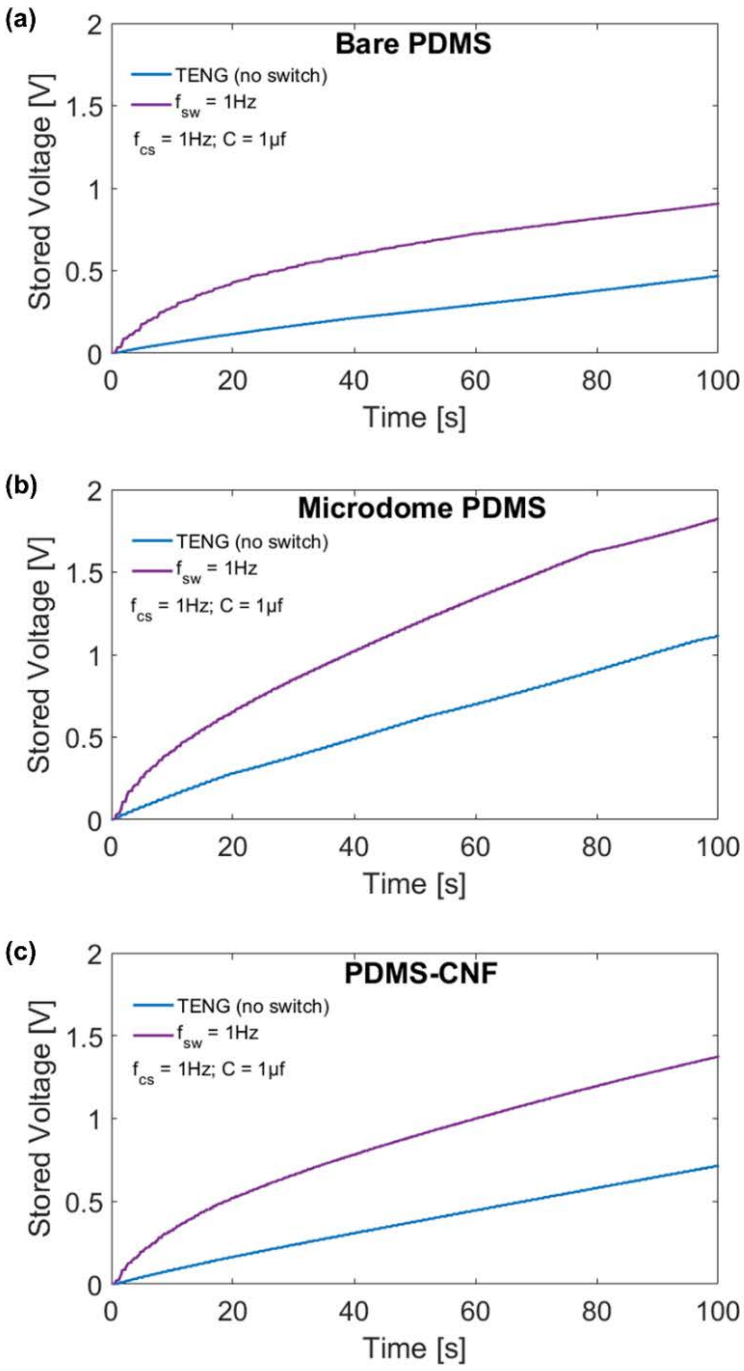

Figure 7.6. Stored voltage measured across a 1μf capacitor while it is being charged with (a) a typical TENG (no switch) and SW-TENG under synchronous switching, both made using a bare PDMS film, (b) a typical TENG (no switch) and SW-TENG under synchronous switching, both made using a microdome PDMS film, and (c) a typical TENG (no switch) and SW-TENG under synchronous switching, both made using a PDMS-CNF composite film.

The stored charge per cycle for the bare PDMS, microdome patterned PDMS, and PDMS-CNF composite based TENGs under typical operation (with f_{cs} equal to 1Hz) is 4.87nC, 7.39nC, and 11.65nC, respectively. Similarly, the stored charge per cycle for the bare PDMS, microdome patterned PDMS, and PDMS-CNF composite based TENGs under synchronous switching operation (with f_{cs} and f_{sw} equal to 1 Hz) is 12.08nC, 16.65nC, and 22.37nC, respectively. This indicates that synchronous switching can enhance the stored charges by a factor of 2.48, 2.25, and 1.92 in the bare PDMS, microdome PDMS, and PDMS-CNF based SW-TENGs, respectively, compared to that achieved under the typical TENG operation. This result is conservative. The actual increase should be larger because a capacitor is not an ideal storage element, and the leakage current leakage increases with applied voltage.

7.3.2 Dependence on external load resistance

The dependence of the output performance of the SW-TENG on different external loads is systematically studied by connecting different load resistances across the generator. Figure 7.7(a-c) shows means and standard deviations (SD) of the output voltage and current peaks under different values of external load resistances. For SW-TENG made using the bare PDMS film, it is observed that the peak voltage mean increased from 13.5 V (n = 8; SD = 0.3) to 55.3 V (n = 8; SD = 0.8), while the peak current mean decreased from 900.0 mA (n = 8; SD = 21.8) to 0.1 mA (n = 8; SD = 0.0), as the load resistance increased from 15 Ω to 1 M Ω (Figure 7.7(a)). Similarly, for SW-TENG made with the microdome patterned PDMS film, the peak voltage mean increased from 27.0 V (n = 8; SD = 0.8) to 121.3 V (n = 8; SD = 2.7), while the peak current mean decreased from 1800.0 mA (n = 8; SD = 50.4) to 0.1 mA (n = 8; SD = 0.0), as the load resistance increased from 15 Ω to 1 M Ω (Figure 7.7(b)). For SW-TENG made with the PDMS-CNF composite film, the

peak voltage mean increased from 36.8 V (n = 8; SD = 0.8) to 174.0 V (n = 8; SD = 0.4), while the peak current mean decreased from 2450.0 mA (n = 8; SD = 56.0) to 0.2 mA (n = 8; SD = 0.0), as the load resistance increased from 15 Ω to 1 M Ω (Figure 7.7(c)). Figure 7.7(d-f) shows the means and SDs of the corresponding instantaneous area power density (calculated using equation (7-2)) under different external load resistances. The maximum area power density (P_d) achieved in the three SW-TENGs (in the order listed) is 3.4Wcm^{-2}, 20Wcm^{-2}, and 31.7Wcm^{-2}, at an external resistance of 56Ω, respectively. This is the optimum external circuit condition for energy conversion for all three SW-TENGs presented here.

$$P_d = \frac{V^2}{RA} \tag{7-2}$$

where V is the peak output voltage of the SW-TENG, R is the external load resistance, and A is the nominal area of the device, i.e., 15mm x 25mm.

TENGs have high inherent impedance stemming from their inherent capacitance, and therefore face a huge impedance mismatch when coupled with energy storage units which usually have low impedance. The high impedance of TENGs leads to very low short-circuit currents which limits its applications. This is particularly true when the mechanical energy source is low-frequency, resulting in ultralow energy storage efficiency (only about 1% when a TENG is used to charge an ideal 1 V battery) [40, 144, 145]. The optimum load resistance (R_{opt}) for a typical TENG can be estimated using equation (7-3), and is generally in the MΩ range [56]. This was evident when the same microdome PDMS based TENG discussed in this chapter was evaluated under typical operating condition, i.e., without a switch, and the optimal load resistance was found to be 4.6 MΩ (refer Figure 6.8(c)). Here, R_{opt} for the SW-TENGs is found to be six orders of magnitude lower, in the ohm range. This is a potential benefit of the SW-TENG.

$$R_{opt} \approx \frac{(d_0 + x_{\max})^2}{Av\varepsilon_0} \tag{7-3}$$

where d_0 is the effective dielectric constant, x_{max} is the maximum separation distance between the dielectric films, A is the nominal area of contact, v is the average velocity, and ε_0 is the permittivity of free space.

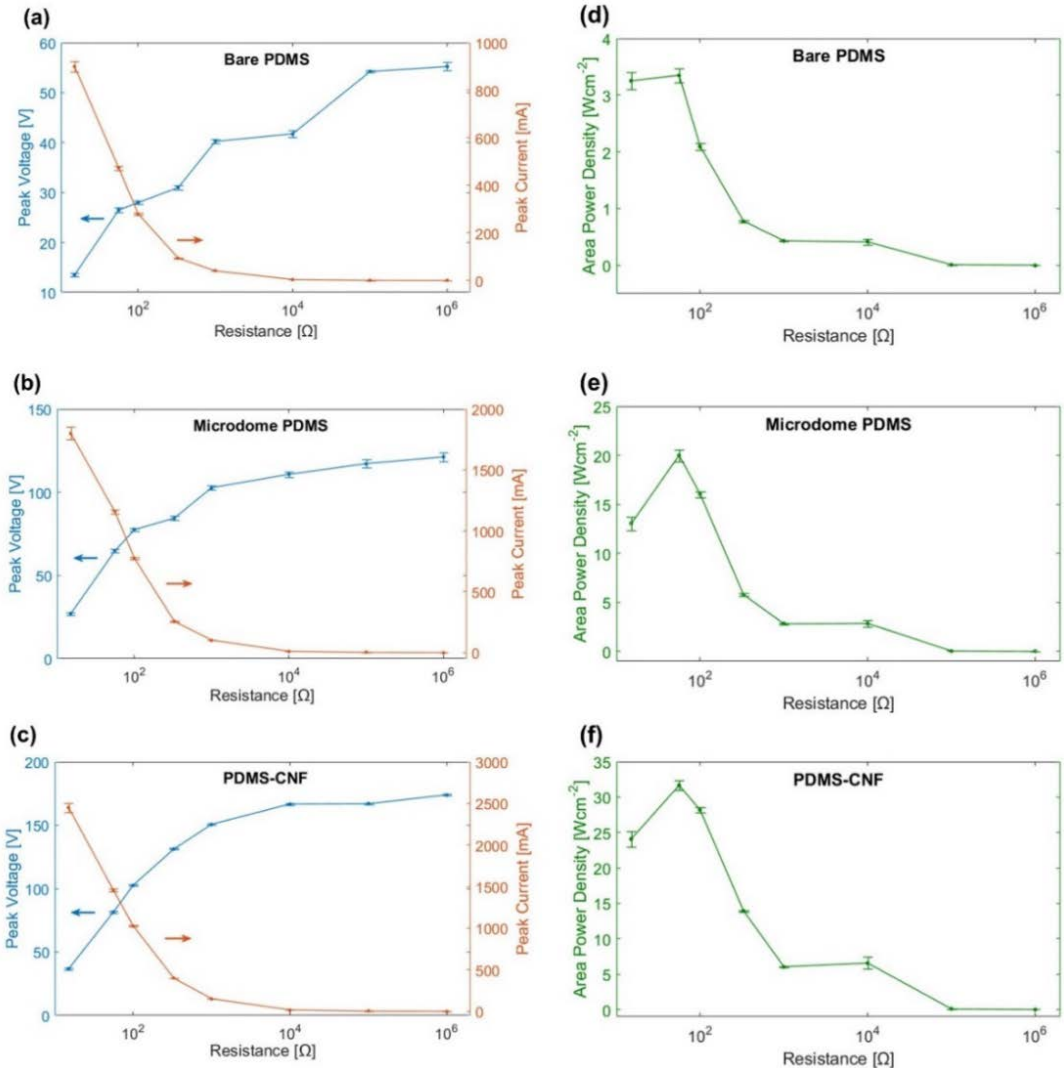

Figure 7.7. Reliance of the output performance of the SW-TENG on external load. (a-c) Output peak voltage, output peak current, and (d-e) instantaneous output area power density dependence on external load resistance in SW-TENGs made with a bare PDMS film, microdome patterned PDMS film, and PDMS-CNF composite film. Note: Error bars represent standard deviation (SD) from the mean (n =8).

The decrease in R_{opt} should be because the inherent capacitance of the TENG (C_{teng}) is electrically isolated from the external circuit for the time duration the switch is open, i.e., for half cycle from contact to separation in the synchronous switching case. The inherent high impedance of the TENG stems from its inherent capacitance, and any factor that increases C_{teng} will lower the inherent impedance, which in turn will lower R_{opt} [91]. From equation (7-3), it is seen that R_{opt} is dependent on the structural parameters of the TENG and the velocity of motion, and is independent of the tribocharge density. An increase in v will lower R_{opt}. As discussed, the circuit only closes when the relay switch closes, bringing the switch contact mechanism into the picture. The contact velocity of the relay switch is several hundred mm/s, and its contact resistance is in the mΩ range [146-148]. This should be additional contributing factors towards lowering R_{opt} of the TENG. R_{opt} is possibly a combination of the relay contact resistance and the TENG impedance seen by the circuit when the switch closes. There may be other factors responsible and further investigation is necessary. Another noteworthy point is that the isolation of the inherent capacitance from the external circuit is also a reason behind the increase in the stored energy across the load capacitor discussed above (Figure 7.6). This is because the total stored energy when $x(t) = x_{max}$ is inversely proportional to the square of the sum of the load capacitance (C_{load}) and the inherent capacitance of the TENG (C_{teng}) [144]. Another factor to investigate to understand the enhancement of output energy better would be the effect of decrease in time duration of the voltage peaks compared to the effect of the increase in voltage amplitude, due to synchronous switching.

7.4 VALIDATING FEASIBILITY FOR PRACTICAL APPLICATIONS

To validate the feasibility of SW-TENG for practical applications, the circuit shown in Figure 7.8 was constructed to light up 3 LEDs connected in series. A storage element such as a capacitor or battery can be used to collect the energy generated in the SW-TENG. Here, a rectified SW-TENG output is used to continuously charge a capacitor to a suitable voltage (switch S1 *on*; switch S2 *off*). This stored energy is then used to light up the LEDs by disconnecting the capacitor from the SW-TENG (S1 *off*) and connecting it across the LEDs (S2 *on*). The SW-TENG is operated under the synchronous switching condition.

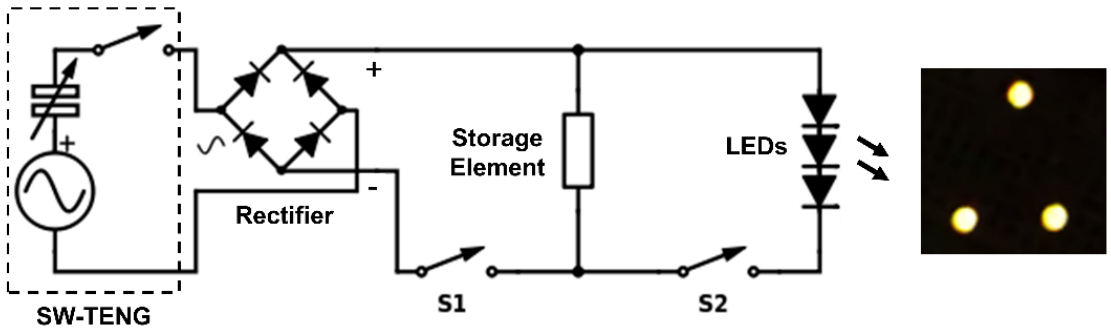

Figure 7.8. The equivalent circuit for lighting up LEDs using the energy stored from the SW-TENG.

Finally, to explore the potential of SW-TENGs to be a completely autonomous energy harvester, a mechanical switch prototype was fabricated and tested. Figure 7.9(a) shows the structure, working, and V_{oc} test results of the prototype. It is obvious that the working of the mechanical prototype switch is similar to the synchronous switching case shown in Figure 7.2, except that the prototype switch only closes when $x(t) = x_{max}$, and is open the remainder of the time. Briefly, metal 3 and metal 1 form a mechanical switch. Once an external force is applied to the structure, bringing the two dielectrics in contact, equal and opposite triboelectric charge

densities (σ) are developed on the contact surfaces. The gap between metal 3 and metal 1 is now x_{max}, and the TENG structure is electrically isolated from the external circuit, i.e., the voltmeter in this case (Figure 7.9(a-ii)). As the force is removed and the oppositely charged films separate, a potential difference is induced between metal 1 and metal 2. When metal 2 contacts metal 3, the circuit is closed and the charges flow from metal 2 to metal 3 to screen the potential difference. V_{oc} keeps increasing until it reaches a maximum value (Figure 7.9(a-iii)). Now, as the top layer is pressed again, the circuit is open once again, continually diminishing V_{oc} in the process (Figure 7.9(a-iv)).

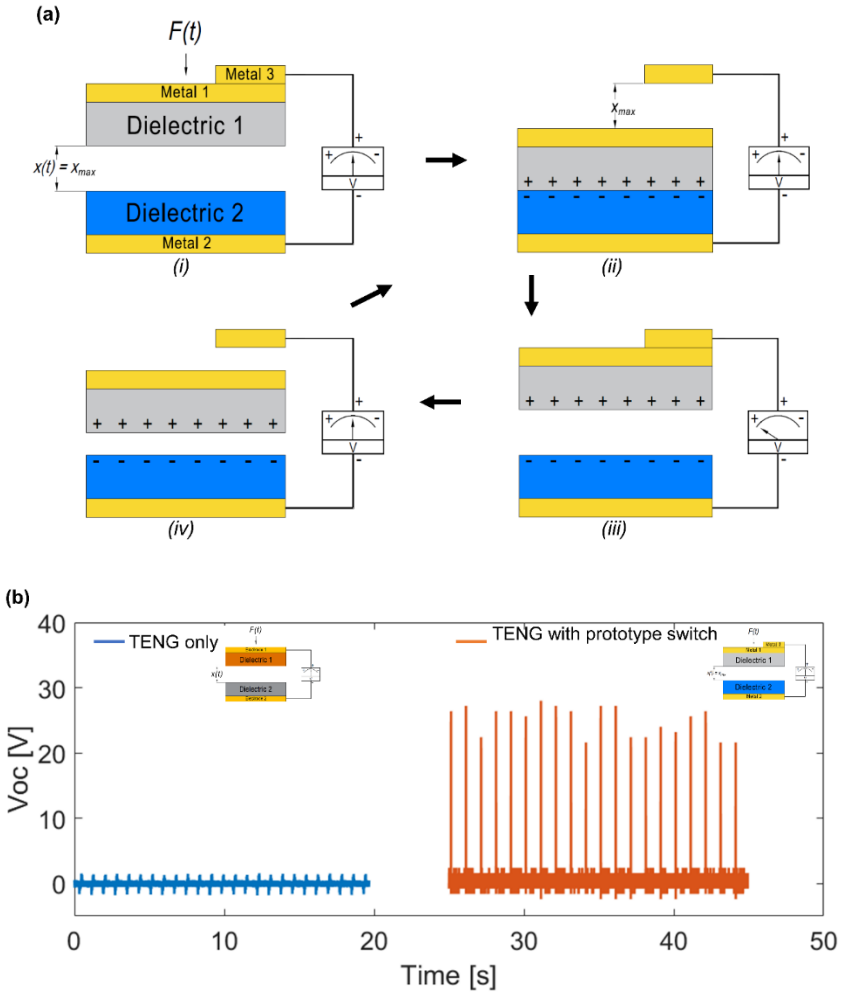

Figure 7.9. (a) Mechanical prototype switch structure and working. (b) Comparison of the open-circuit voltage outputs of a typical TENG and a TENG with prototype switch.

Figure 7.9(b) compares the open-circuit voltages of a PDMS-CNF based TENG under typical operating condition and under mechanical switching condition. It is seen that voltage output increases at least by a factor 10 due to mechanical switching. With carefully designed switching mechanisms, better results can be obtained. This successfully demonstrates the practical viability of incorporating a switching mechanism in a contact-mode TENG.

7.5 METHODS

7.5.1 Method for switching frequency tests

The switching frequency test set-up schematic is shown in Figure 7.10. A PRS (QRE1113; Fairchild Semiconductor) is calibrated to detect the contact between the two dielectric materials. The PRS output responds to the motion of the movable support using changes in transmissivity of infrared light as the movable support travels from a position of maximum separation ($x(t) = x_{max}$) to a position of full contact between the dielectric films ($x(t) = 0$). An Arduino microcontroller is used to read the PRS signal, and trigger the electromagnetic relay at a specified frequency at the occurrence of contact. All voltage measurements are performed using a 10x probe with an oscilloscope having an internal resistance of 1 MΩ. A computer interfaces with the microcontroller, so it can be programmed and with the oscilloscope, so the recorded voltage data can be saved for analysis.

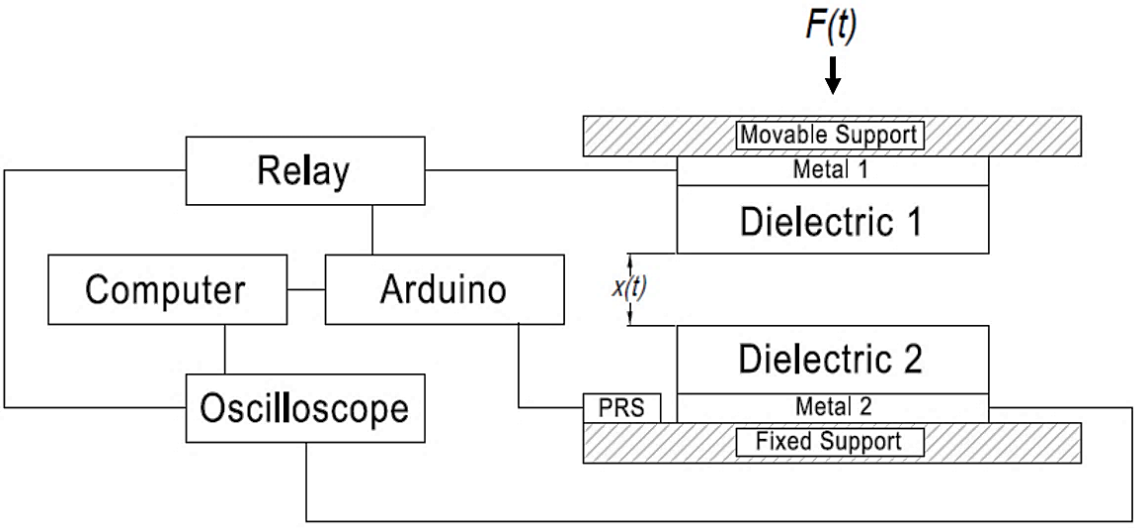

Figure 7.10. Switching frequency test set-up schematic.

7.5.2 Fabrication of PDMS-CNF composite film

A polymer solution of 10wt% polyacrylonitrile (PAN) in N,N-Dimethyl Formamide (DMF) is made by weighing the appropriate amounts of the precursor and stirred for 12hrs. The polymer solution is then transferred into a syringe and injected into the electrospinning setup through a stainless-steel needle at a rate of 1.5ml/hr. A potential difference of 15KV is applied between the needle and the rotating cylinder collecting the PAN nanofibers and the distance between the tip of needle and drum is maintained at 15cm. SEM image of the electrospun PAN nanofibers is shown in Figure 7.11(a). Subsequently, the obtained PAN nanofibers were exfoliated from the rotating drum collector and a stabilization heat treatment is done at 200C for 4hrs with a heating rate of 5C/min in air. The stabilized PAN nanofibers were carbonized at 700C for 1hr in argon atmosphere to obtain the carbon nanofibers (CNFs) used to make the PDMS composite. Figure 7.11(b) shows the Raman spectra of the fabricated CNFs in a range of Raman shift from 1000 to 1800 cm^{-1}. The two broad peaks at ~1369-1372 cm-1 (D-Band) and ~ 1585 - 1590 cm-1 (G-

Band) with R ~ 2.45 (ID/IG) correspond to an in-plane graphitic crystallite size La = 4.4/R = 1.8nm - 1.9nm (obtained from Guassian fitting of the spectra) and are in agreement with those previously reported in literature [149]. The ratio of intensity of the D-band to G-band also determines the electrical conductivity as well as the mechanical properties of the CNF [150, 151]. To make the composite film, a solution of 2.5wt% CNFs in PDMS base (Sylgard 184, Tow Corning) is mixed homogenously using a magnetic stirrer, and the curing agent is then added such that the base to curing agent are in a 10:1 ratio (w/w). This solution is stirred, coated on a glass slide, and degassed. After curing, the PDMS-CNF composite film is peeled off.

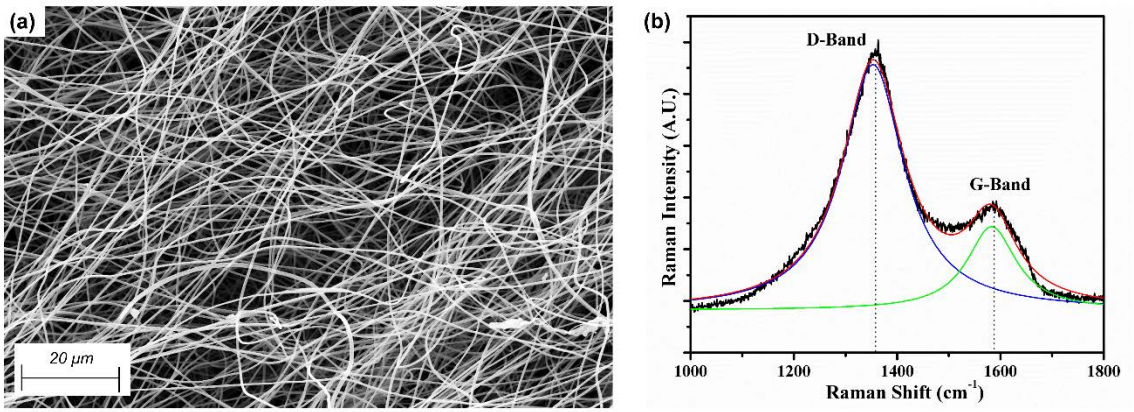

Figure 7.11. (a) SEM image of electrospun polyacrylonitrile (PAN) nanofibers. (b) Raman spectra of carbon nanofibers (CNFs).

7.5.3 Fabrication of PDMS film with microdome structures

This is discussed in section 6.2.1, and is repeated here. PLGA polymer resin (85:15) is first dissolved in chloroform (3 wt. %) and then coated on Cu foil to a uniform thickness using a doctor blade. The Cu foil with the PLGA thin film is then dipped in a chloroform-methanol mixture (volume ratio of 17/3) for 2s and extracted, forming a template with well-ordered

microwell patterns on its surface. PDMS elastomer mixture (Sylgard 184, Tow Corning) with a 10:1 ratio (w/w) of the base and the curing agent is stirred and coated on the PLGA template fabricated above, and degassed. After curing at room temperature, the PDMS film with microdome structures is carefully peeled off. Acetone is used to dissolve any residue of PLGA.

7.6 SUMMARY

A new approach for mechanical energy harvesting has been demonstrated, wherein a switch is incorporated in a TENG. It has been shown that under synchronous switching condition, i.e., when the switching frequency is the same as the contact-separation frequency of the TENG, the output energy is enhanced by over a factor of two and the optimum load resistance is lowered, from megaohms to ohms. This is shown to be true for TENGs made using three different types of polydimethylsiloxane (PDMS) based films – (a) bare PDMS film, (b) microdome patterned PDMS film, and (c) PDMS-CNF composite film, thus demonstrating versatility of the approach. Practical viability of the approach is demonstrated by charging a commercial capacitor and using the stored charge to light up three LEDs. In addition, a TENG integrated with a mechanical prototype switch is successfully fabricated and tested. This approach thus offers tremendous potential for development of new designs and applications across all operating mode of TENGs.

8.0 FUTURE WORK

In this work, the potential of using triboelectric effect to harvest energy from respiratory motion in a non-invasive manner, is identified. The challenges of harvesting from irregular, low frequency, and low force motions have been studied, and the advantages of using a TENG over classical energy harvesting techniques have been demonstrated. The TENG technology has improved significantly since its first report by ZL Wang's group in 2012. However, low current output of TENGs due to their high inherent impedance remains a great challenge. It is well-known that selecting appropriate charging materials and modifying surface characteristics are effective ways of enhancing the triboelectric charge density, and thereby the current output. While impactful research efforts continue in this direction, there is still a lot of scope for improvement in TENG device structures that can be instrumental in reducing impedance.

The research-to-practice path of TENG involves moving knowledge gained from basic sciences to its application. This translational path is a continuous process. With the overarching theme of further improving output and wearability of the respiratory harvester, and its effectiveness as a self-powered respiration sensor, future research work could be conducted in the following directions:

- Integrating a synchronous switch mechanism in the wREH
- Exploring new designs to improve wearability, particularly fabric-based approaches
- Correlating the output signal from the harvester with a spirogram

APPENDIX A

A.1 CONCEPT GENERATION AND SELECTION

Table 8.1 presented here shows several respiratory energy harvester concepts based on contact-separation that were generated along with some of their potential drawbacks/advantages. In this work, the lever mechanism concept was selected for further development based on its simple and effective design. This concept is #5 in the table below and chapter 6.0 discusses its development in detail.

Table 8.1. Illustrations of respiratory energy harvester concepts along with their potential advantages(A)/disadvantages(D)

#1 Concave substrate based triboelectric generator (TG)

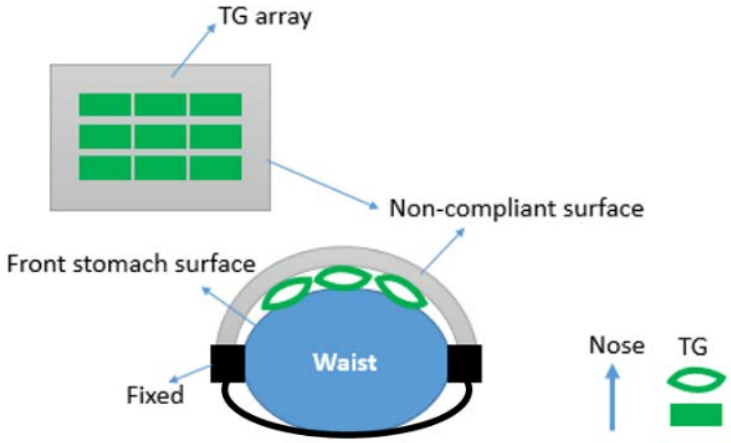

Table 8.1 (continued)

- A: (i) multiple elements can increase effective contact area
- D: (i) a large non-complaint surface may be inconvenient to wear; (ii) The motion is not uniform throughout the abdominal surface, and not the same for all humans. So, the gap in the TG elements should be custom-designed.

#2 Skin-based TG

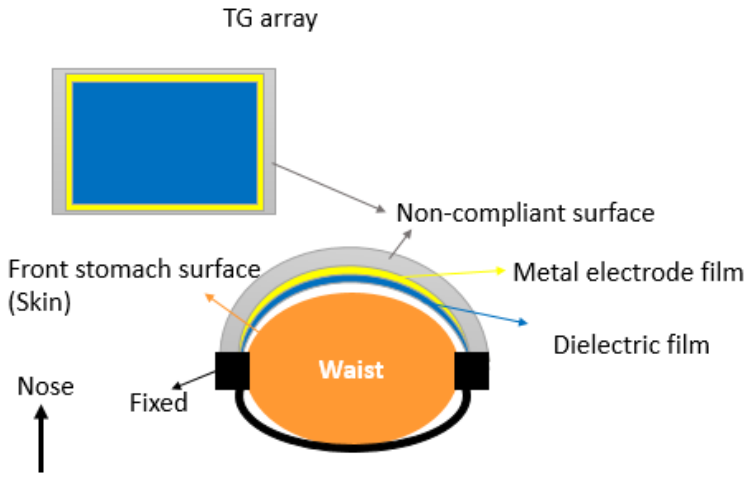

- A: (i) reduces design and fabrication complexity
- D: (i) a large non-complaint surface may be inconvenient to wear; (ii) As discussed in section 6.2, the charge generation process in a TG is significantly affected by humidity. Therefore, with direct skin contact, this design is more vulnerable to humidity.

#3 Vertical contact-separation with a gear assembly

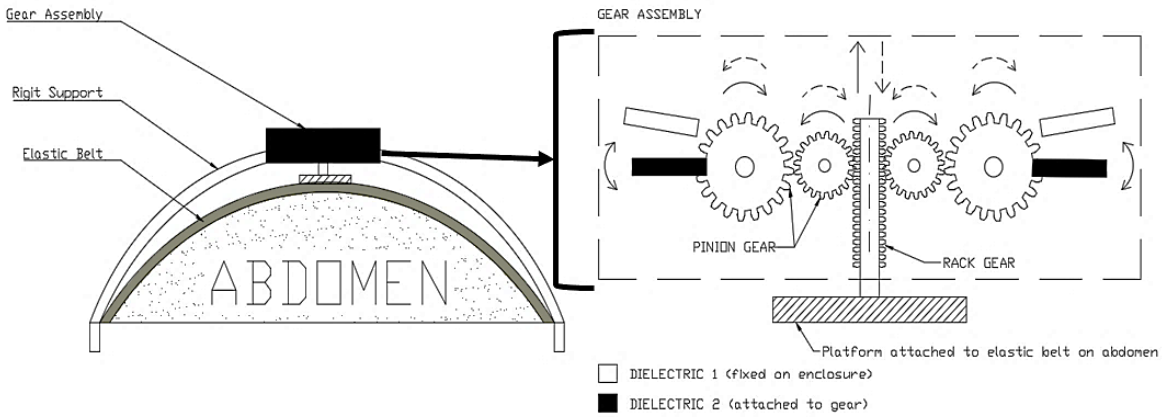

- A: (i) amplifies contact force and (ii) contact area

Table 8.1 (continued)

- D: (i) relatively a complex structure to fabricate; (ii) may be cumbersome to wear; (iii) gear mechanism may add extra resistance during respiration

#4 Vertical contact-separation

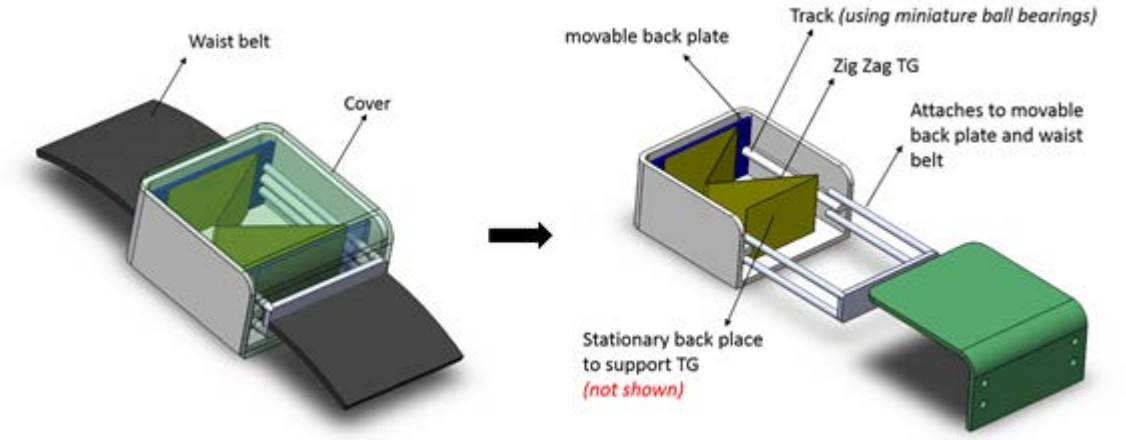

- A: (i) high wearability; (ii) increases effective contact area; (iii) frequency multiplication*
- D: (i) track design may be complex as the motion is not exactly linear

#5 Angular contact-separation - Lever mechanism

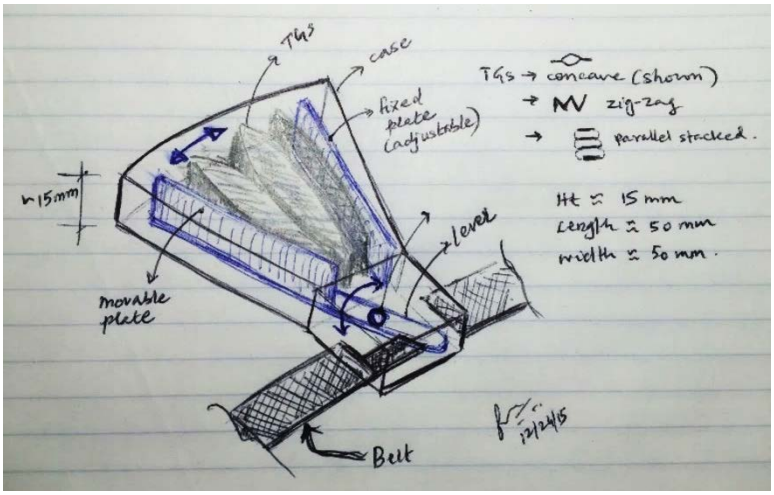

- A: (i) high wearability; (ii) increases effective contact area; (iii) amplifies separation; (v) frequency multiplication*; (vi) potentially more sensitive to motion; (vii) ease of fabrication
- D: (i) bearings failure

Table 8.1 (continued)

***Note:** The zig-zig TG (referred to as the accordion-like structure in chapter 6.0) has a frequency multiplication effect, which also helps in enhancing the output of the generator. A proof-of-concept test was conducted with a TG made with nominally flat polyethylene terephthalate (PET) and polyimide film, having an additional third layer placed in between. The third layer has a PET film with attached electrode on one side facing the polyimide film, while a polyimide film with attached electrode is on the other side facing the PET film. As expected, two peaks are observed in a single contact-separation cycle – one at intermediate contact, and the second at full contact (see figure below).

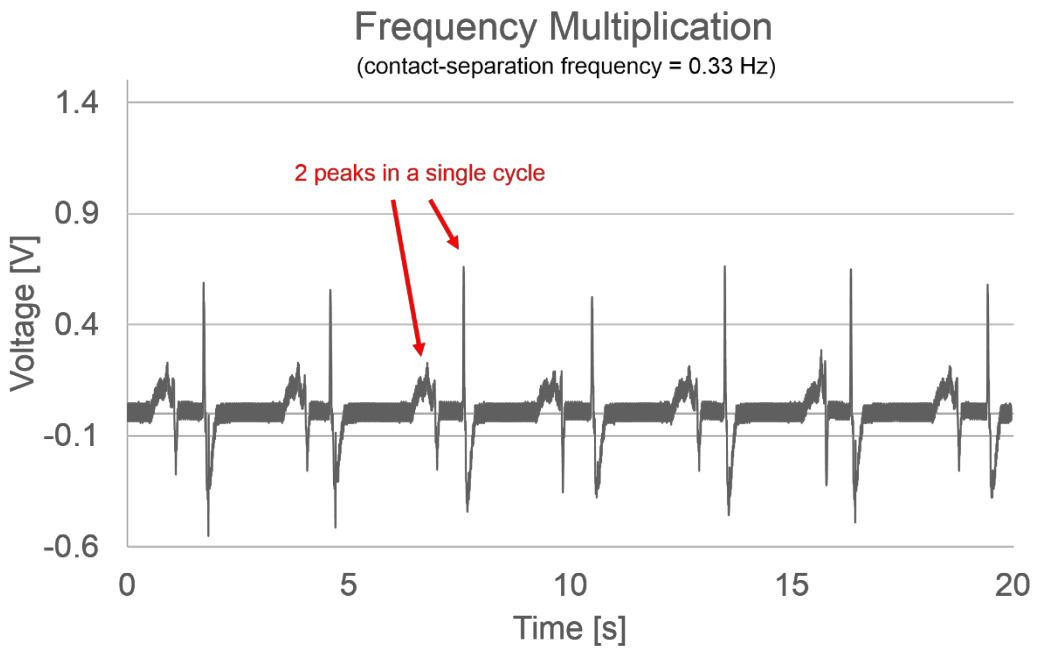

BIBLIOGRAPHY

[1] B. Gyselinckx, C. Van Hoof, J. Ryckaert, R.F. Yazicioglu, P. Fiorini, V. Leonov, Proceedings of the IEEE 2005 Custom Integrated Circuits Conference, 2005., Institute of Electrical & Electronics Engineers (IEEE).

[2] M. Seyedi, B. Kibret, D.T. Lai, M. Faulkner, IEEE Transactions on Biomedical Engineering, 60 (2013) 2067-2079.

[3] J.L. Gonzalez, A. Rubio, F. Moll, Int J Soc Mater Eng for Resourc, 10 (2002).

[4] S. Wang, Z.-H. Lin, S. Niu, L. Lin, Y. Xie, K.C. Pradel, Z.L. Wang, Acs Nano, 7 (2013) 11263-11271.

[5] N.S. Choi, Z. Chen, S.A. Freunberger, X. Ji, Y.K. Sun, K. Amine, G. Yushin, L.F. Nazar, J. Cho, P.G. Bruce, Angewandte Chemie, 51 (2012) 9994-10024.

[6] J.-M. Tarascon, M. Armand, Nature, 414 (2001) 359-367.

[7] D.H.P. Kang, M. Chen, O.A. Ogunseitan, Environmental science & technology, 47 (2013) 5495-5503.

[8] D. Larcher, J.-M. Tarascon, Nature chemistry, 7 (2015) 19-29.

[9] P.D. Mitcheson, E.M. Yeatman, G.K. Rao, A.S. Holmes, T.C. Green, Proceedings of the IEEE, 96 (2008) 1457-1486.

[10] K. Bult, A. Burstein, D. Chang, M. Dong, M. Fielding, E. Kruglick, J. Ho, F. Lin, T. Lin, W. Kaiser, Proceedings of the 1996 international symposium on Low power electronics and design, IEEE Press1996, pp. 17-21.

[11] J.D. Meindl, Proceedings of the IEEE, 83 (1995) 619-635.

[12] J.A. Paradiso, T. Starner, IEEE Pervasive Computing, 4 (2005) 18-27.

[13] Z.L. Wang, G. Zhu, Y. Yang, S. Wang, C. Pan, Materials Today, 15 (2012) 532-543.

[14] J.M. Donelan, Q. Li, V. Naing, J.A. Hoffer, D.J. Weber, A.D. Kuo, Science (New York, NY), 319 (2008).

[15] L. Mateu, F. Moll, Microtechnologies for the New Millennium 2005, International Society for Optics and Photonics2005, pp. 359-373.

[16] T. Starner, IBM systems Journal, 35 (1996) 618-629.

[17] G.A. Brooks, T.D. Fahey, T.P. White, Exercise physiology: Human bioenergetics and its applications, Mayfield publishing company1996.

[18] S. Roundy, P.K. Wright, J. Rabaey, Computer communications, 26 (2003) 1131-1144.

[19] H. Liu, C. Lee, T. Kobayashi, C.J. Tay, C. Quan, Sensors and Actuators A: Physical, 186 (2012) 242-248.

[20] H. Kulah, K. Najafi, IEEE Sensors Journal, 8 (2008) 261-268.

[21] W.F. Ganong, K.E. Barrett, Review of medical physiology, Appleton & Lange Norwalk, CT1995.

[22] C.R. Saha, T. O'Donnell, N. Wang, P. McCloskey, Sensors and Actuators A: Physical, 147 (2008) 248-253.

[23] S.P. Beeby, R. Torah, M. Tudor, P. Glynne-Jones, T. O'donnell, C. Saha, S. Roy, Journal of Micromechanics and microengineering, 17 (2007) 1257.

[24] S.P. Beeby, M.J. Tudor, N. White, Measurement science and technology, 17 (2006) R175.

[25] M. Rezaei, J. Lueke, D. Raboud, W. Moussa, Microsystem Technologies, 19 (2013) 1195-1219.

[26] D. Shen, J.-H. Park, J.H. Noh, S.-Y. Choe, S.-H. Kim, H.C. Wikle, D.-J. Kim, Sensors and actuators A: physical, 154 (2009) 103-108.

[27] W. Yang, J. Chen, G. Zhu, J. Yang, P. Bai, Y. Su, Q. Jing, X. Cao, Z.L. Wang, ACS nano, 7 (2013) 11317-11324.

[28] P. Bai, G. Zhu, Z.-H. Lin, Q. Jing, J. Chen, G. Zhang, J. Ma, Z.L. Wang, ACS Nano, 7 (2013) 3713-3719.

[29] T.-C. Hou, Y. Yang, H. Zhang, J. Chen, L.-J. Chen, Z. Lin Wang, Nano Energy, 2 (2013) 856-862.

[30] S. Wang, Y. Xie, S. Niu, L. Lin, Z.L. Wang, Advanced materials, 26 (2014) 2818-2824.

[31] Y. Yang, H. Zhang, Z.-H. Lin, Y.S. Zhou, Q. Jing, Y. Su, J. Yang, J. Chen, C. Hu, Z.L. Wang, ACS Nano, 7 (2013) 9213-9222.

[32] J. Zhong, Q. Zhong, F. Fan, Y. Zhang, S. Wang, B. Hu, Z.L. Wang, J. Zhou, Nano Energy, 2 (2013) 491-497.

[33] L. Dhakar, P. Pitchappa, F.E.H. Tay, C. Lee, Nano Energy, 19 (2016) 532-540.

[34] Y. Zhu, B. Yang, J. Liu, X. Wang, L. Wang, X. Chen, C. Yang, Scientific reports, 6 (2016).

[35] S. Lee, W. Ko, Y. Oh, J. Lee, G. Baek, Y. Lee, J. Sohn, S. Cha, J. Kim, J. Park, Nano Energy, 12 (2015) 410-418.

[36] T. Zhou, C. Zhang, C.B. Han, F.R. Fan, W. Tang, Z.L. Wang, ACS applied materials & interfaces, 6 (2014) 14695-14701.

[37] X. Pu, L. Li, H. Song, C. Du, Z. Zhao, C. Jiang, G. Cao, W. Hu, Z.L. Wang, Advanced materials, 27 (2015) 2472-2478.

[38] W. Seung, M.K. Gupta, K.Y. Lee, K.-S. Shin, J.-H. Lee, T.Y. Kim, S. Kim, J. Lin, J.H. Kim, S.-W. Kim, ACS nano, 9 (2015) 3501-3509.

[39] F.-R. Fan, Z.-Q. Tian, Z.L. Wang, Nano Energy, 1 (2012) 328-334.

[40] S. Niu, X. Wang, F. Yi, Y.S. Zhou, Z.L. Wang, Nature communications, 6 (2015).

[41] Z. Wen, H. Guo, Y. Zi, M.-H. Yeh, X. Wang, J. Deng, J. Wang, S. Li, C. Hu, L. Zhu, ACS nano, 10 (2016) 6526-6534.

[42] Y. Zi, H. Guo, Z. Wen, M.-H. Yeh, C. Hu, Z.L. Wang, ACS Nano, 10 (2016) 4797-4805.

[43] G. Zhu, B. Peng, J. Chen, Q. Jing, Z. Lin Wang, Nano Energy, 14 (2015) 126-138.

[44] S. Niu, X. Wang, F. Yi, Y.S. Zhou, Z.L. Wang, Nature communications, 6 (2015) 8975.

[45] S. Niu, Z.L. Wang, Nano Energy, 14 (2015) 161-192.

[46] D.J. Lacks, R. Mohan Sankaran, Journal of Physics D: Applied Physics, 44 (2011) 453001.

[47] C. Sun, J. Shi, D.J. Bayerl, X. Wang, Energy & Environmental Science, 4 (2011) 4508.

[48] J.-J. Wang, H.-J. Su, C.-I. Hsu, Y.-C. Su, Journal of Physics: Conference Series, 557 (2014) 012022.

[49] S. Roundy, P.K. Wright, Smart Materials and structures, 13 (2004) 1131.

[50] H. Li, C. Tian, Z.D. Deng, Applied Physics Reviews, 1 (2014) 041301.

[51] P. Patel, M.B. Khamesee, Microsystem Technologies, 19 (2013) 1357-1363.

[52] A. Delnavaz, J. Voix, IECON 2012-38th Annual Conference on IEEE Industrial Electronics Society, IEEE2012, pp. 984-988.

[53] E. Shahhaidar, B. Padasdao, R. Romine, C. Stickley, O. Boric-Lubecke, Engineering in Medicine and Biology Society (EMBC), 2013 35th Annual International Conference of the IEEE, IEEE2013, pp. 3439-3442.

[54] H. Kulah, K. Najafi, Micro Electro Mechanical Systems, 2004. 17th IEEE International Conference on.(MEMS), IEEE2004, pp. 237-240.

[55] Q. Zheng, B. Shi, F. Fan, X. Wang, L. Yan, W. Yuan, S. Wang, H. Liu, Z. Li, Z.L. Wang, Advanced materials, 26 (2014) 5851-5856.

[56] S. Niu, S. Wang, L. Lin, Y. Liu, Y.S. Zhou, Y. Hu, Z.L. Wang, Energy & Environmental Science, 6 (2013) 3576.

[57] F.-R. Fan, L. Lin, G. Zhu, W. Wu, R. Zhang, Z.L. Wang, Nano letters, 12 (2012) 3109-3114.

[58] G. Zhu, C. Pan, W. Guo, C.-Y. Chen, Y. Zhou, R. Yu, Z.L. Wang, Nano letters, 12 (2012) 4960-4965.

[59] G. Zhu, Z.H. Lin, Q. Jing, P. Bai, C. Pan, Y. Yang, Y. Zhou, Z.L. Wang, Nano letters, 13 (2013) 847-853.

[60] G. Zhu, J. Chen, Y. Liu, P. Bai, Y.S. Zhou, Q. Jing, C. Pan, Z.L. Wang, Nano letters, 13 (2013) 2282-2289.

[61] S. Wang, L. Lin, Y. Xie, Q. Jing, S. Niu, Z.L. Wang, Nano letters, 13 (2013) 2226-2233.

[62] L. Lin, S. Wang, Y. Xie, Q. Jing, S. Niu, Y. Hu, Z.L. Wang, Nano letters, 13 (2013) 2916-2923.

[63] S. Niu, Y. Liu, S. Wang, L. Lin, Y.S. Zhou, Y. Hu, Z.L. Wang, Advanced materials, 25 (2013) 6184-6193.

[64] F. Saurenbach, D. Wollmann, B.D. Terris, A.F. Diaz, Langmuir, 8 (1992) 1199-1203.

[65] L.S. McCarty, G.M. Whitesides, Angewandte Chemie, 47 (2008) 2188-2207.

[66] R. Elsdon, F.R.G. Mitchell, Journal of Physics D: Applied Physics, 9 (1976) 1445-1460.

[67] W.R. Harper, Contact and frictional electrification, Clarendon P., Oxford, 1967.

[68] M.W. Williams, Aip Advances, 2 (2012) 010701.

[69] L.-H. Lee, Journal of electrostatics, 32 (1994) 1-29.

[70] M.D. Hogue, C.R. Buhler, C.I. Calle, T. Matsuyama, W. Luo, E.E. Groop, Journal of Electrostatics, 61 (2004) 259-268.

[71] L.B. Schein, M. LaHa, D. Novotny, Physics Letters A, 167 (1992) 79-83.

[72] J. Lowell, A.C. Rose-Innes, Advances in Physics, 29 (1980) 947-1023.

[73] A.G. Bailey, Journal of Electrostatics, 51 (2001) 82-90.

[74] G. Castle, Journal of Electrostatics, 40 (1997) 13-20.

[75] G. Castle, L. Schein, Journal of Electrostatics, 36 (1995) 165-173.

[76] S. Matsusaka, H. Maruyama, T. Matsuyama, M. Ghadiri, Chemical Engineering Science, 65 (2010) 5781-5807.

[77] R.L. Jackson, J.L. Streator, Wear, 261 (2006) 1337-1347.

[78] R.L. Jackson, I. Green, Tribology Transactions, 54 (2011) 300-314.

[79] A.W. Bush, R.D. Gibson, T.R. Thomas, Wear, 35 (1975) 87-111.

[80] Y.S. Zhou, S. Wang, Y. Yang, G. Zhu, S. Niu, Z.-H. Lin, Y. Liu, Z.L. Wang, Nano letters, 14 (2014) 1567-1572.

[81] D. Davies, Journal of Physics D: Applied Physics, 2 (1969) 1533.

[82] I. Johnston, D. McCluskey, C. Tan, M. Tracey, Journal of Micromechanics and Microengineering, 24 (2014) 035017.

[83] D. Nečas, P. Klapetek, Open Physics, 10 (2012) 181-188.

[84] Y.H. Ko, S.H. Lee, J.W. Leem, J.S. Yu, RSC Advances, 4 (2014) 10216-10220.

[85] Y. Zhu, B. Yang, J. Liu, X. Wang, L. Wang, X. Chen, C. Yang, Scientific reports, 6 (2016) 22233.

[86] M.D. Hogue, University of Central Florida, Ann Arbor, 2005, pp. 85-85 p.

[87] B.D. Terris, J.E. Stern, D. Rugar, H.J. Mamin, Physical review letters, 63 (1989) 2669-2672.

[88] H.T. Baytekin, A.Z. Patashinski, M. Branicki, B. Baytekin, S. Soh, B.A. Grzybowski, Science, 333 (2011) 308-312.

[89] L. Zhang, F. Xue, W. Du, C. Han, C. Zhang, Z. Wang, Nano Res., 7 (2014) 1215-1223.

[90] Y. Yang, G. Zhu, H. Zhang, J. Chen, X. Zhong, Z.-H. Lin, Y. Su, P. Bai, X. Wen, Z.L. Wang, ACS Nano, 7 (2013) 9461-9468.

[91] S. Niu, Y.S. Zhou, S. Wang, Y. Liu, L. Lin, Y. Bando, Z.L. Wang, Nano Energy, 8 (2014) 150-156.

[92] S. Niu, Y. Liu, S. Wang, L. Lin, Y.S. Zhou, Y. Hu, Z.L. Wang, Adv. Funct. Mater., 24 (2014) 3332-3340.

[93] J.P.C. Kleijnen, S.M. Sanchez, T.W. Lucas, T.M. Cioppa, INFORMS Journal on Computing, 17 (2005) 263-289.

[94] A.F. Diaz, R.M. Felix-Navarro, Journal of Electrostatics, 62 (2004) 277-290.

[95] S.M. Sanchez, 2007 Winter Simulation Conference, Institute of Electrical & Electronics Engineers (IEEE)2007.

[96] J.K. Telford, J Hopkins Apl Tech D, 27 (2007) 224-232.

[97] M.C. Croarkin, J. Res. Natl. Inst. Stand. Technol., 106 (2001) 279.

[98] C.M. Prado, E.A. Leick-Maldonado, L. Yano, A.S. Leme, V.L. Capelozzi, M.A. Martins, I.F. Tibério, American journal of respiratory cell and molecular biology, 35 (2006) 457-465.

[99] A.B. Otis, C.B. McKerrow, R.A. Bartlett, J. Mead, M. McIlroy, N. Selverstone, E. Radford, Journal of applied physiology, 8 (1956) 427-443.

[100] W. Zin, A. Rossi, L. Zocchi, J. Milic-Emili, Journal of applied physiology, 57 (1984) 271-277.

[101] J.-L. Vincent, E. Abraham, P. Kochanek, F.A. Moore, M.P. Fink, Textbook of critical care, Elsevier Health Sciences2011.

[102] Kevin, (2017).

[103] A. McConnell, Breathe strong, perform better, Human Kinetics2011.

[104] J.N. Mills, The Journal of physiology, 112 (1951) 201-203.

[105] O. Nisell, Acta physiologica Scandinavica, 59 (1963) 85-96.

[106] T. Earthrowl-Gould, B. Jones, M.R. Miller, Proceedings of the Institution of Mechanical Engineers. Part H, Journal of engineering in medicine, 215 (2001) 515-520.

[107] G.H. van Ramshorst, M. Salih, W.C. Hop, O.J. van Waes, G.J. Kleinrensink, R.H. Goossens, J.F. Lange, The Journal of surgical research, 171 (2011) 240-244.

[108] G.H. van Ramshorst, J.F. Lange, R.H. Goossens, N.L. Agudelo, G.J. Kleinrensink, M. Verwaal, S.F. Flipsen, W.C. Hop, L.S. Wauben, J. Jeekel, Physiological measurement, 29 (2008) N41-N47.

[109] Y. Sugiura, M. Inami, T. Igarashi, Proceedings of the 25th annual ACM symposium on User interface software and technology, ACM2012, pp. 529-536.

[110] S. Wang, L. Lin, Z.L. Wang, Nano letters, 12 (2012) 6339-6346.

[111] X.S. Zhang, M.D. Han, R.X. Wang, F.Y. Zhu, Z.H. Li, W. Wang, H.X. Zhang, Nano letters, 13 (2013) 1168-1172.

[112] V. Nguyen, R. Yang, Nano Energy, 2 (2013) 604-608.

[113] H. Guo, J. Chen, L. Tian, Q. Leng, Y. Xi, C. Hu, ACS applied materials & interfaces, 6 (2014) 17184-17189.

[114] C.K. Chua, K.F. Leong, Rapid prototyping: principles and applications, World Scientific2003.

[115] Y.H. Ko, G. Nagaraju, S.H. Lee, J.S. Yu, ACS applied materials & interfaces, 6 (2014) 6631-6637.

[116] X. Liu, H.-G. Jung, S.-O. Kim, H.-S. Choi, S. Lee, J.H. Moon, J.K. Lee, Scientific reports, 3 (2013) 3183.

[117] F.-R. Fan, Z.-Q. Tian, Z. Lin Wang, Nano Energy, 1 (2012) 328-334.

[118] Y. Tada, Japanese journal of applied physics, 31 (1992) 846.

[119] T. O'Hanlon-Nichols, AJN The American Journal of Nursing, 98 (1998) 39-45.

[120] M. Skubic, G. Alexander, M. Popescu, M. Rantz, J. Keller, Technology and Health Care, 17 (2009) 183-201.

[121] J. Greenwood, K. Johnson, E. Matsubara, Wear, 100 (1984) 47-57.

[122] X. Miao, X. Huang, Wear, 309 (2014) 146-151.

[123] Y. Hu, Y. Zhang, C. Xu, L. Lin, R.L. Snyder, Z.L. Wang, Nano letters, 11 (2011) 2572-2577.

[124] M.A. McDowell, C.D. Fryar, C.L. Ogden, K.M. Flegal, National health statistics reports, 10 (2008) 5.

[125] A. Tilley, (1993).

[126] T.R. Gildea, K. McCarthy, Cleveland clinic: current clinical medicine, (2010).

[127] A.B. Otis, W.O. Fenn, H. Rahn, Journal of applied physiology, 2 (1950) 592-607.

[128] J.N. Davis, D. Stagg, The Journal of physiology, 245 (1975) 481-498.

[129] K. Konno, J. Mead, J Appl Physiol, 22 (1967) 407-422.

[130] A. De Groote, M. Wantier, G. Cheron, M. Estenne, M. Paiva, Journal of applied physiology, 83 (1997) 1531-1537.

[131] M.A. Sackner, H. Watson, A.S. Belsito, D. Feinerman, M. Suarez, G. Gonzalez, F. Bizousky, B. Krieger, Journal of applied physiology, 66 (1989) 410-420.

[132] M.A. Cretikos, R. Bellomo, K. Hillman, J. Chen, S. Finfer, A. Flabouris, Medical Journal of Australia, 188 (2008) 657.

[133] J.F. Fieselmann, M.S. Hendryx, C.M. Helms, D.S. Wakefield, Journal of general internal medicine, 8 (1993) 354-360.

[134] Z.L. Wang, J. Chen, L. Lin, Energy Environ. Sci., 8 (2015) 2250-2282.

[135] C. Han, C. Zhang, W. Tang, X. Li, Z.L. Wang, Nano Research, 8 (2015) 722-730.

[136] V. Gurevich, Electric relays: Principles and applications, CRC Press2016.

[137] J.L. Blackburn, T.J. Domin, Protective relaying: principles and applications, CRC press2015.

[138] Y.G. Paithankar, S. Bhide, Fundamentals of power system protection, PHI Learning Pvt. Ltd.2010.

[139] K. Li, F. Yao, J. Lu, Z. Li, Electrical Contacts, 2000. Proceedings of the Forty-Sixth IEEE Holm Conference on, IEEE2000, pp. 79-82.

[140] W. Li, J. Sun, M. Chen, Nano Energy, 3 (2014) 95-101.

[141] Y. Zi, L. Lin, J. Wang, S. Wang, J. Chen, X. Fan, P.K. Yang, F. Yi, Z.L. Wang, Advanced materials, 27 (2015) 2340-2347.

[142] M.-L. Seol, S.-H. Lee, J.-W. Han, D. Kim, G.-H. Cho, Y.-K. Choi, Nano Energy, 17 (2015) 63-71.

[143] N. Roy, A.K. Bhowmick, Journal of Materials Science, 47 (2012) 272-281.

[144] S. Niu, Y. Liu, Y.S. Zhou, S. Wang, L. Lin, Z.L. Wang, IEEE Transactions on Electron Devices, 62 (2015) 641-647.

[145] S. Niu, Z.L. Wang, Nano Energy, 14 (2015) 161-192.

[146] W. Ren, J. Jin, Y. Fu, C. Chang, Electrical Contacts (Holm), 2014 IEEE 60th Holm Conference on, IEEE2014, pp. 1-7.

[147] R.K. Frazier, S. Alles, Electromagnetic Compatibility, 2005. EMC 2005. 2005 International Symposium on, IEEE2005, pp. 949-954.

[148] G. Zhai, W. Fan, W. Liang, Computational Engineering in Systems Applications, IMACS Multiconference on, IEEE2006, pp. 1074-1081.

[149] Y. Wang, S. Serrano, J.J. Santiago-Aviles, Synthetic Metals, 138 (2003) 423-427.

[150] M. Panapoy, A. Dankeaw, B. Ksapabutr, Thammasat Int J Sc Tech, 13 (2008) 11-17.

[151] L. Feng, N. Xie, J. Zhong, Materials, 7 (2014) 3919-3945.